



Universitetet
i Stavanger

FACULTY OF SCIENCE AND TECHNOLOGY

MASTER'S THESIS

Study programme/specialisation: Petroleum Engineering / Natural Gas Technology	Spring semester, 2018 Open
Author: Anecito D. Silvano (signature of author)
Faculty Supervisor(s): Professor Runar Bøe	
Title of master's thesis: Flow Investigation of Stall and Choke on Axial Compressor using CFD	
Credits (ECTS): 30	
Keywords: axial compressor, stall, choke, CFD, compressor performance map, snappyHexMesh, boundary conditions, OpenFoam solver	Number of pages: 94 + enclosure: 15 Stavanger, June 15, 2018 date/year

ABSTRACT

The complicated nature of axial compressor fluid dynamics instabilities such as stall and choke when utilizing air power left a lot of room for investigation during the state of operation. This dynamic instabilities diminished compressor efficiency, reliability, and even loss of engine power leading to catastrophic failure. Therefore, it is extremely important to understand how choke and stall occurs and the causes behind its inception.

The interactions between the shock wave and the tip clearance flow have been identified as the primary cause of stall. Thus, to explore its flow mechanisms and the physical trends as compressor throttle towards stall, fundamental questions are have to be answered in the course of investigation. These questions are the following:

- How does the rotor blade tip clearance flow affects shock wave during interactions?
- Does shock boundary layer leading to shock waves causes flow separation?
- What is the possible behavior of both the shock wave and the rotor tip clearance flow?

Investigation rolls around NASA Rotor 67, a transonic axial compressor turbo rotor fan, operated without inlet guide vane(IGV) and stator. This rotor-only configuration enables comparison of its experimental data(A. J. Strazisar et. al., 1989) and the numerical flow analysis using computational fluid dynamics(CFD) simulation in OpenFOAM. Thus, actual application of fluid dynamics physical laws and theories into CFD tool is the main take-away of the author's academic gain on this study.

A three-dimensional unsteady Navier-Stokes equations and proper set of stable and accurate boundary conditions were studied and applied. The flow case was scrutinized to select proper solver and turbulence model. The OpenFOAM solver, *rhoPimpleDyMFoam*, and the k- ω -SST turbulence model applied to Approximate Reimann(ARS) solver fits the case showing good convergence with resulting flow field in agreement with the experiment.

Compressor performance map operating points(peak efficiency condition, near stall and stalled condition) were thoroughly investigated on the simulation by studying the flow fields in the rotor tip region. It is found that the interaction between the shock wave and the rotor blade tip vortex leakage flow is mainly the reason behind the stall of axial compressor.

KEYWORDS: *axial compressor, stall, choke, CFD, compressor performance map, snappyHexMesh, boundary conditions, OpenFoam solver*

ACKNOWLEDGEMENTS

Definitely, there are people that touched and changed my life for the better that made my journey to Norway possible leading to this master study.

To start, I would like to share that me and my family were about to go back home after I lost my job in the fall of 2015. I just took my chances and applied personally for a master study at the University of Stavanger(UiS) though classes were already started in a week or so. And so, I am very grateful for the golden opportunity given to me and my family that affects not only me but also them in a big way. I want to acknowledged with sincere gratitude to the following people making all these possible.

First, to Marit Håvardsholm for her devoted assistance, true work and serviced leading to my acceptance and a study place at the university, I cherished that very day when I come at your office, small details how you help still fresh and your mutual respect, I am so grateful, thank you so much.

Second, to Åshild Kitty Shearer. I would like to pay my respect and gratitude for her initiative, who offered her time for teaching me basics and general background on drilling and geology on my first school day upon knowing I have no petroleum engineering background and considering I was a total stranger to her, it was for me a miracle and I thank you for showing the beautiful spirit and culture of your ancestors.

To Professor Runar Bøe, I am so grateful for giving me a chance to work on this thesis under your arm. Your kindness, acceptance and trust is so inspiring when you agreed to be my supervisor.

To my best friend Ranil de la Pena, I thank you for the referral that brought me to work in this country leading to this degree. To my parents and the SPCC group, I thank you for your encouragement and prayers.

I owe my greatest gratitude to my wife Herly for working so hard, so that I can still continue this master study. And to my children Herliane and Helynne, you are the fuel in times of desperation, I dedicate this to you.

Lastly, to God be the honor and glory!.

TABLE OF CONTENTS

ABSTRACT	II
ACKNOWLEDGEMENTS	III
TABLE OF CONTENTS	IV
LIST OF FIGURES	VI
LIST OF TABLE(S)	VIII
NOMENCLATURE	IX
CHAPTER 1: INTRODUCTION	1
1.1. AXIAL COMPRESSOR - AN OVERVIEW	3
1.1.1. AXIAL COMPRESSOR VELOCITY TRIANGLES	4
1.1.2. AXIAL COMPRESSOR COMPRESSION STAGE	5
1.1.3. COMPRESSOR STABILITY	8
1.1.4. BLADE CASCADE NOTATION AND TERMINOLOGY	9
1.2. COMPRESSOR INSTABILITY	10
1.3. AXIAL COMPRESSOR BASIC OPERATION	13
1.4. OBJECTIVES AND ORGANIZATION OF THE PRESENT WORK	14
CHAPTER 2: LITERATURE REVIEW	16
2.1. FUNDAMENTALS OF ROTATING STALL	16
2.2. THE CONCEPT OF SURGE	18
2.3. FUNDAMENTALS CHOKED FLOW	18
2.3.1. COMPRESSIBLE FLOW	19
2.4. ON ROTATING STALL AND SURGE - A LITERATURE SURVEY	19
2.5. COMPUTATIONAL STUDIES OF COMPRESSOR FLOW	20
2.6. TURBULENCE MODELING OF FLOW IN CFD	21
2.7. BOUNDARY CONDITION ON STUDIED DOMAIN	22
CHAPTER 3: NUMERICAL FORMULATION AND CFD TOOLS	23
3.1. NAVIER-STOKES EQUATIONS	23
3.2. RANS EQUATIONS IN A ROTATING FRAME OF REFERENCE	25
3.3. RANS NUMERICAL FORMULATION IN OPENFOAM SOLVER	26
3.1. HYPERBOLIC SOLUTION	27
3.1.1. GODUNOV SCHEME	27
3.1.2. SOLUTION OF THE RIEMANN PROBLEM IN EULER EQUATIONS	28
3.1.3. THE HLLC APPROXIMATE RIEMANN SOLVER	28
3.1.4. RIEMANN SOLVER FOR CAPTURING SHOCKS IMPLEMENTED IN OPENFOAM	29
3.2. TURBULENCE MODELING	30
3.2.1. BOUNDARY LAYER SHEAR STRESS TRANSPORT (SST)	30
3.3. SPATIAL DISCRETIZATION	32
3.4. TIME DESCRETIZATION	33
3.4.1. STEADY SOLVER	33
3.4.2. UNSTEADY SOLVER	34
3.5. THE CONVERGENCE TECHNIQUES	34

CHAPTER 4: THE TEST CASE AND SETTINGS AT OPENFOAM SOLVER.....	36
4.1. THE TEST CASE - NASA ROTOR 67.....	36
4.1.1. TEST PARAMETER DESCRIPTION OF THE ROTOR.....	37
4.2. OPENFOAM OVERVIEW.....	39
4.2.1. OPENFOAM WORK FLOW AND CASE STRUCTURE.....	39
4.3. DATA.....	41
4.3.1. EXPERIMENTAL DATA EXTRACTION.....	41
4.3.2. NUMERICAL DATA EXTRACTION(POST-PROCESSING).....	43
4.4. MESHING.....	45
4.4.1. THE ROTOR GEOMETRY.....	45
4.4.2. CREATING THE TRI-SURFACE PATCHES.....	47
4.4.3. MESHING THE COMPUTATIONAL DOMAIN.....	49
4.4.4. THE PASSAGE ROTOR COMPUTATIONAL DOMAIN.....	55
4.5. NUMERICAL SET UP.....	56
4.5.1. THE SOLVER.....	56
4.5.2. TURBULENCE MODELING.....	57
4.6. INITIAL AND BOUNDARY CONDITIONS.....	58
4.6.1. INLET BOUNDARY CONDITION.....	59
4.6.2. OUTLET BOUNDARY CONDITION.....	59
4.6.3. WALL BOUNDARY CONDITION.....	59
4.6.4. PERIODIC BOUNDARY CONDITION.....	60
CHAPTER 5: RESULTS AND DISCUSSION.....	62
5.1. RESULTS ON PEAK EFFICIENCY CONDITION.....	63
5.2. STALL INITIATION.....	68
5.2.1. RESULTS OF INDUCING STALL.....	69
CHAPTER 6: CONCLUSION AND FUTURE WORK.....	76
REFERENCES.....	78
APPENDIX 1 - SNAPPYHEXMESH FILE DICTIONARY.....	81
APPENDIX 2 - SNAPPYHEXMESH RUN.....	87
APPENDIX 3 - CHECK MESH OF SNAPPYHEXMESH RESULT.....	90
APPENDIX 4 - PORTION OF RHOPIMPLEDYMFOAM SOLVER OUTPUT.....	93
APPENDIX 5 - TURBULENCE PROPERTIES.....	94

LIST OF FIGURES

Figure 1. 1 - Turbo-machinery applications.....	1
Figure 1. 2 - Compressor Blades as diffuser-Outlet area is larger than the inlet((David Japikse, 1997).....	3
Figure 1. 3 - (a)Velocity triangle of axial compressor (b)Changes in fluid properties in axial compressor ..	4
Figure 1. 4 - Temperature-Enthalpy diagram of the compression stage of axial compressor	6
Figure 1. 5 - Compressor Stability	8
Figure 1. 6 - Blade Cascade notation.....	9
Figure 1. 7 - Blade Terminology.....	10
Figure 1. 8 - Operational Stability. Matching Compressor Characteristics and Throttle Characteristics....	11
Figure 1. 9 - Typical Compressor Performance Map, Emphasis on the Effect of Compressor Speeds	12
Figure 1. 10 - Single Stage of Axial Compressor	13
Figure 1. 11 - Axial Compressor Basic Mechanism of Operation	14
Figure 2. 1 - Rotating Stall Propagation(Individual column of blades defecting stall development).....	16
Figure 2. 2 - Full-Span Stall(Pampreen, 1993), viewed in axial direction	17
Figure 2. 3 - Part-Span Stall(Pampreen, 1993), viewed in axial direction	18
Figure 3. 1 - Descrization of mesh cells (Toro, 1999)	27
Figure 3. 2 - HLLC approximate solution structure(Toro, 1999).....	29
Figure 3. 3 - Cells discretization method (Toro, 1999)	32
Figure 4. 1 - Rolls Royce Jet Engine. Courtesy: (Royce).....	36
Figure 4. 2 - NASA Rotor 67	37
Figure 4. 3 - Aerodynamic survey probes(A.J. Strazisar et. al.,(1989)).....	38
Figure 4. 4 - Laser Anemometer and aerodynamic survey locations(A.J. Strazisar et. al.,(1989)).....	38
Figure 4. 5 - OpenFOAM Workflow	39
Figure 4. 6 - A sample OpenFOAM case structure	40
Figure 4. 7- Data Coordinate Measurement(A.J. Strazisar et. al.,(1989)) , RP-radial position,.....	41
Figure 4. 8 - (a) Streamlines (b) Constant chord percentage line(A.J. Strazisar et. al.,(1989))	42
Figure 4. 9-Window numbering(A.J. Strazisar et. al.,(1989)) with emphasis each blade having same window point(top).....	42
Figure 4. 10 - Data extraction in <i>Paraview</i>	43

Figure 4. 11 - Streamwise pitch percentage of the flow passage	44
Figure 4. 12 - Sample of a <i>function object</i> code for Plotting and data extraction(Residuals plots sample)	45
Figure 4. 13 - Rotor Blade - CAD modeled.....	46
Figure 4. 14 - Meridional Plane(A.J. Strazisar et. al.,(1989)	47
Figure 4. 15 - 3D mesh of the rotor geometry in Salome.....	48
Figure 4. 16 - The tri-surface .stl geometries as one flow domain(one face is hidden to see inside).....	49
Figure 4. 17 - Background mesh with tri-surface .stl geometries inside(iso and top view)	50
Figure 4. 18 - Castellated Mesh of the Fluid Computational Domain(Bottom) and tri-surface boundaries(Top)	51
Figure 4. 19 - Surface snapping result in snappyHexMesh. mesh off(top), mesh on(bottom)	52
Figure 4. 20 - Different mesh refinement level sensitivity run of the computational domain in snappyHexMesh.	53
Figure 4. 21 - Blade section mesh detail	54
Figure 4. 22 - snappyHexMesh results of the computational domain. whole mesh(top), interior mesh cut-out view(bottom)	55
Figure 4. 23 - Passage Rotor Domain	56
Figure 4. 24 - Boundary layer regions(Bakker, 2002).....	57
Figure 4. 25 - Boundary conditions used in the analysis.....	58
Figure 4. 26 - C-Grid boundary cut of the computational domain.....	60
Figure 4. 27-Periodic boundary cyclicGgi dictionary.....	61
Figure 5. 1 - Sample of the residual plot	62
Figure 5. 2 - Peak Efficiency condition time history of mass flow rate fluctuations.....	63
Figure 5. 3 - Pressure and mass flow rate fluctuations at peak efficiency conditions	64
Figure 5. 4 - Comparison between the CFD Results and experimental results of inlet axial velocity(C_a) at peak efficiency conditions.....	64
Figure 5. 5 - Mach number plot at 70% span from shroud near peak efficiency	65
Figure 5. 6 - Comparison between experiments and CFD results of relative Mach number at 10% span and 30% pitch at peak efficiency conditions.....	66
Figure 5. 7 - Comparison between experiments and CFD results of relative Mach number at 10% span and 50% pitch at peak efficiency conditions.....	67
Figure 5. 8 - Static pressure gradient contour plots at 30% and 70% span at peak efficiency conditions..	67

Figure 5. 9 - Relative velocity vectors at mid-span(50% span) at peak efficiency condition	68
Figure 5. 10 - Experimental and CFD Result Comparison of the Performance map	70
Figure 5. 11 - Mass flow rate convergence history for NASA Rotor 67 operating points A, B, and C.....	70
Figure 5. 12 - Comparison of experimental (AJ. Strazisar et al. (1989)) and CFD computed adiabatic efficiency	71
Figure 5. 13 - Tip section static pressure contours.....	73
Figure 5. 14 - Entropy contours at meridional plane view at the middle(50% pitch)	73
Figure 5. 15 - Tip gap leakage vortex shedding streamlines	74
Figure 5. 16 - Operating point C(in-stall condition) velocity vectors near leading edge.....	75

LIST OF TABLE(S)

Table 4. 1 - Inlet Boundary Conditions.....	59
---	----

NOMENCLATURE

Symbols

δ_{ij}	Kronecker delta	-
η	Efficiency	-
γ	Specific heat ratio	-
μ	Viscosity	$\text{kg m}^{-1}\text{s}^{-1}$
ν	Kinematic viscosity	m^2s^{-1}
Ω	Vorticity	s^{-1}
ω	Specific dissipation rate, rotational speed	s^{-1} , rps
\emptyset	Dimensionless coefficient for velocity, Stage loading coefficient	-
Π	Total pressure ratio	-
ψ	Dimensionless parameter coefficient for work, Flow coefficient	-
ρ	Density	kg m^{-3}
σ	Total shear stress tensor; Effective turbulent quantity	$\text{kg m}^{-1-2}\text{s}$
τ	Shear stress	$\text{kg m}^{-1-2}\text{s}$
τ_t	Pseudo time-step	s
v	Volume	m^3
ϵ	Turbulent dissipation	m^2s^3
φ	Arbitrary quantity	-
α	Absolute flow angle	$^\circ$
β	Relative flow angle	$^\circ$
γ	Ratio C_p/C_v , or blade inlet angle for blade terminology	-
θ	Tangential coordinate	-
ϕ	camber angle for blade terminology, or flow coefficient	$^\circ$

Mathematical Symbols

Δ	Difference operator	-
$\frac{\partial}{\partial}$	Partial derivative operator	-
∇	Gradient operator	-
$\nabla \cdot$	Divergence operator	-
$\nabla \nabla \cdot$	Laplacian operator	-
\mathfrak{R}_b	Blade-to-Blade radius	m
\mathfrak{R}_n	Meridional radius	m
sup	Supremum operator	-
A	Area	m^{-2}
\mathbf{F}	Flux tensor	-
\mathbf{F}^{hllc}	Godunov flux	-
\mathbf{R}	Residual vector	-
\mathbf{U}	Conservative state vector	-
\mathbf{W}	Primitive variables	-
\tilde{A}	Mass-averaged of an arbitrary quantity	-
$\vec{\mathbf{U}}$	Absolute velocity vector	ms^{-1}
$\vec{\mathbf{U}}_{\text{rel}}$	Relative velocity vector	ms^{-1}
\vec{q}	Heat flux vector	$\text{kJm}^{-2}\text{s}^{-1}$
A''	Arbitrary quantity fluctuation	-
c, a	Sound velocity	ms^{-1}
C	Air velocity	ms^{-1}
C_{cfl}	Courant-Friedrich-Lewy number	-
C_p	Specific heat (constant pressure)	$\text{kJkg}^{-1}\text{K}^{-1}$
E	Total Energy	kJ
F	Decomposed flux tensor in an arbitrary referential	-

h	Enthalpy	kJkg^{-1}
K, k	Turbulent kinetic energy	m^2s^2
m, \dot{m}	Mass flow rate	kg s^{-1}
Ma	Mach number	-
O	Order	-
P, p	Pressure	kg m^2
Pr	Prandtl number	-
q	conserved flow variables	-
r	Radial coordinate	(m, °)
r_m	Mean radius	m
r_t	Tip radius	m
r_h	Hub radius	m
Re	Reynolds number	-
s	Blade pitch	m
S_{ij}	Mean strain tensor	s^{-1}
T	Temperature	K
t	Time	s
u, v, w	Velocity components in a Cartesian referential	ms^{-1}
V, U	Magnitude of (absolute) velocity	ms^{-1}
V_θ	Tangential velocity	ms^{-1}
W	Magnitude of relative velocity	ms^{-1}
x, y, z	Cartesian coordinates	m
y^+	Dimensionless distance to wall	-
R	Specific gas constant	$\text{kJkg}^{-1}\text{K}^{-1}$
r, θ, z	Cylindrical coordinates	-
w, W	Work	kJ s^{-1}

Subscripts

0	Total quantities
1	Rotor inlet (ambiguous with Runge-Kutta coefficients)
2	Rotor outlet (ambiguous with with Runge-Kutta coefficients)
3	Rotor inlet for the second stage for multi-compressor stage
<i>a</i>	Adiabatic, also used as axial component of velocity
<i>c</i>	Convective terms
<i>d</i>	Dissipative terms
<i>i</i>	Cell index (ambiguous with with the matrix index)
<i>l, L</i>	Left
<i>r, R</i>	Right
<i>s</i>	Static quantities
<i>S</i>	compressor stage
<i>t</i>	Temporal term
*	Star Region
∞	free stream quantity, upstream of the inlet
<i>blade, rot</i>	Blade
<i>diaph</i>	Diaphragm
<i>fan</i>	Expansion fan
<i>Lam</i>	Laminar
<i>max</i>	Maximum
<i>min</i>	Minimum
<i>r, θ, z</i>	Cylindrical directions
<i>sw</i>	stream-wise
<i>Turb</i>	Turbulent
<i>x, y, z</i>	Cartesian directions

Superscripts

T	Transpose
$n+1$	Next time step
n	Current time step

Abbreviations

3D	Three dimensional
ALE	Arbitrary Lagrangian-Eulerian
ARS	Approximate Riemann Solver
B2B	Blade to blade
CFD	Computational Fluid Dynamics
CFL	Courant-Friedrich-Lewy
DNS	Direct Numerical Simulation
GGI	General Grid Interface
GUI	Graphic User Interface
HP	High Pressure
HLLC	Harten Lax Van Leer Contact
IP	Intermediate Pressure
IRS	Implicit Residual Smoothing
LA	Laser Anemometer
LE	Leading Edge
LES	Large Eddy Simulation
LP	Low Pressure
LTS	Local Time Stepping
MUSCL	Monotone Upstream-Centered Schemes for Conservative Laws
NACA	National Advisory Committee for Aeronautics
NASA	National Aeronautics and Space Administration
N-S	Navier-Stokes

PIMPLE	Combined PISO and SIMPLE Algorithm
PISO	Pressure-Implicit Split Operator
PS	Pressure Side
$rx\theta$ -M	Radius_Theta-Meridional
R67	Rotor 67
RP	Radial Position
SDRC	Structural Dynamics Research Corporation
SIMPLE	Semi-Implicit Method For Pressure-Linked Equations
SST	Shear Stress Transport
TE	Trailing Edge
WNBEG	Starting Window Number for Laser Anemometer Survey

CHAPTER 1: INTRODUCTION

Turbo-machineries are composed of complex parts and play a vital role for world's energy supply and mobility of the modern world. Turbo machines utilized a continuous flowing fluids for its operation through interactions of its physical sub-components, mainly a rotating blades, for the machine to operate. Aircraft engines and steam turbines are some examples of these. Figure 1.1, (a) to (g) shows different applications of turbo-machinery: aero-planes turbine propulsion, wind turbine for electricity production, ship propulsion, pipeline fluid transport, internal combustion engine turbo charging, steam turbine for power generation and process plant accessories.

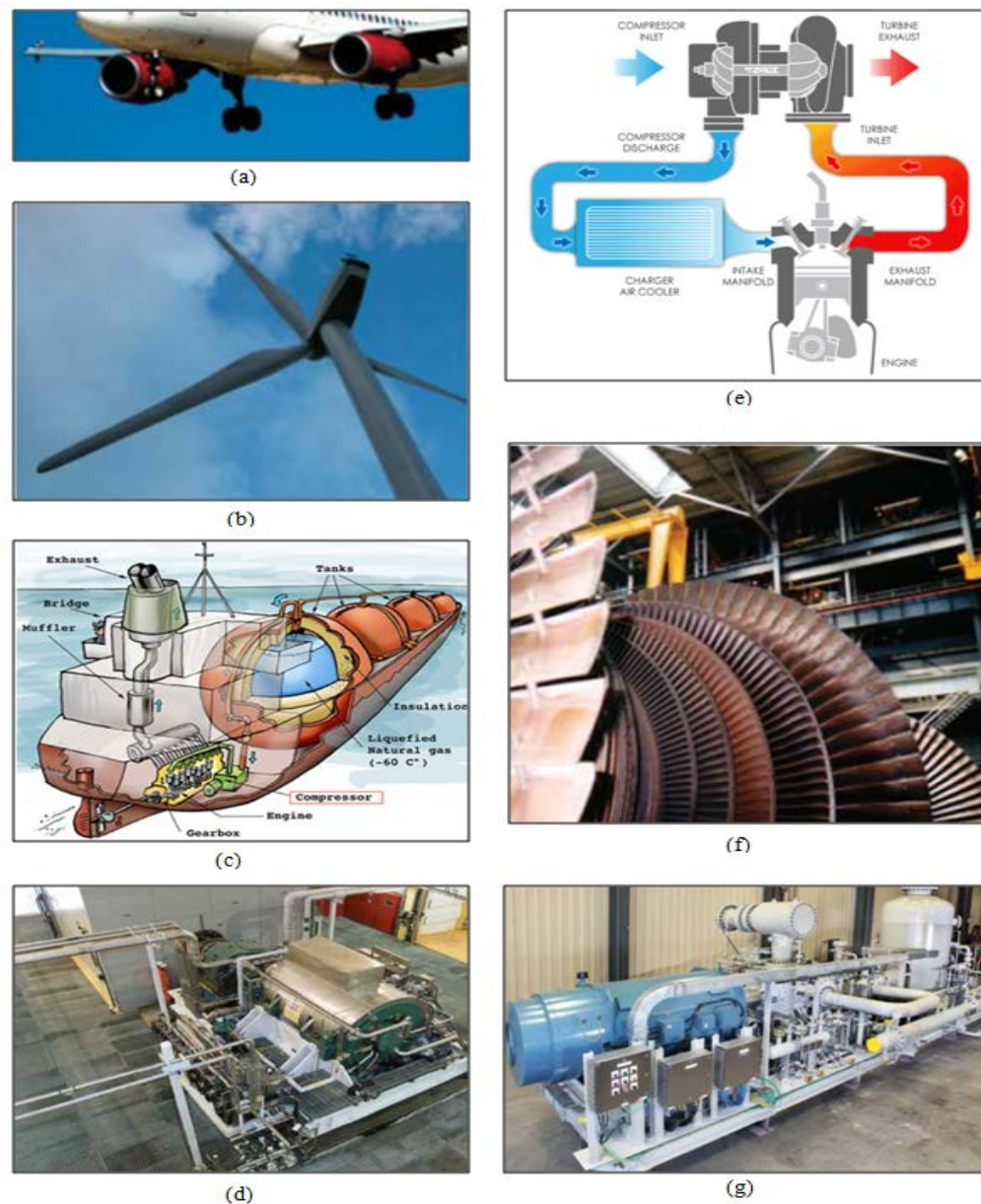


Figure 1.1 - Turbo-machinery applications

Source: <http://en.wikipedia.org/wiki/Images>

Turbo-machines can be classified in three ways (Ingram, 2009), the type of fluid that they used is the first, second is based on direction that the fluid flow travel through the machine and the third is whether the machine is delivering power to or extracting power from the working fluid.

The type of fluids used, split machine into two categories, the one that work on compressible fluids (stationary gas turbines, aircraft engines, high speed fans). The characteristics of these machines is that if the velocity of the fluid goes above the local speed of sound, shock waves may formed. The second, is those machine that work with incompressible fluids such as water or oil (ship propellers, pumps, hydraulic turbines). Shock waves are not an issue in liquids but the phenomenon known as cavitation which occurs if the pressure of the fluids falls below its characteristic pressure properties. In addition, the fluid density is not constant anymore and varies along its path.

For the machine under direction of flow classification, essentially if the flow is along the longitudinal axis of the machine it is called axial machine but if the fluid flow direction turns and has component velocity in radial direction it is known as centrifugal or radial machine.

Lastly, a type of machine which *extract energy* from the fluids and the one that *delivers energy* to the fluids. The former refers to as turbines and the latter are called compressors, blowers or pumps depending on the type of fluids used and the magnitude of pressure rise.

For this study, we are dealing with compressible fluids that absorbs energy from the machines in axial flow direction.

Technological invention of turbo-machines are rich in engineering and physical phenomena that a curious mind would consider investigating for better understanding. This is where the governing laws, physics, equations etc. are taking place which pioneers of physics and mathematics, the likes of Newton and its contemporaries has left us to understand, study or improved. There are many ways how fluids are being process by this machines depending on its intended purpose and application. For this work, we are mainly focused on compression process done by compressors and its subsequent phenomena. Thus, this will be discuss in the subsequent sections and chapters.

As shown in Figure 1.1, compressors are one of the most important components of these turbo-machineries. Various components of internal combustion engine where compressor forms the first part of the engine is shown in Figure 1.1, (e). Compressors increases the total enthalpy of the working fluid using the work of the input shaft. Reciprocating, rotary, centrifugal and axial are four general types of compressors. Reciprocating and rotary compressors aimed at reducing the gas volume at delivery. Centrifugal and axial compressors transfers energy to the fluid by accelerating the fluids to high velocities and later decelerating it through a diverging channel to convert the kinetic energy into pressure energy. This work only deals with deals with axial compressor.

1.1. AXIAL COMPRESSOR - AN OVERVIEW

Compressor fluid flow operates in the concept of diffusion. Thus, its blade are arranged and design as a diffuser. A diffuser is any flow element that allows the flow to decelerate due to an increase in flow area(e.g. divergent walls), and this in turn permits the static pressure to rise due to Euler or Bernoulli equation. The diffuser is a comparatively simple element in which the fluid may attain complicated flow states.

The air compressor increases the air pressure, using the power input via the shaft to accelerate the air stream and convert the kinetic energy to pressure through the diffuser shaped blade channels. Figure 1.2 below illustrates compressor blades as a diffuser.

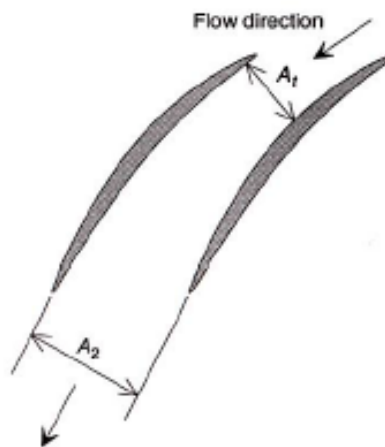


Figure 1. 2 - Compressor Blades as diffuser-Outlet area is larger than the inlet((David Japikse, 1997)

Using the continuity equation, assuming constant density for simplicity, one can see that the increasing area(diffuser effect) results in velocity reduction, so that kinetic energy is converted to pressure.

$$\text{By conservation of mass: } \dot{m} = \rho(v) = \rho(C_1 * A_1) = \rho(C_2 * A_2) \quad (1-1)$$

$$\text{Assuming constant density, we can write: } \frac{A_2}{A_1} = \frac{C_1}{C_2} \quad (1-2)$$

where: A is passage area, C is the air velocity, \dot{m} is the mass flow, ρ is density, v = specific volume, subscript 1 and 2 is the inlet and outlet respectively.

Since the flow moves towards higher pressure, which is the opposite to the rule of nature, there is always a risk for flow reversal and unstable operation, called stall. Growing boundary layer around the blades results in reduction of flow passage area, which can result in flow separation, called rotating stall, which can develop into full surge(more details on the next sections). Large forces are released during surge that can cause serious damage to the compressor.

1.1.1. AXIAL COMPRESSOR VELOCITY TRIANGLES

When a body is moving with an object, it has velocity vectors that each are acting. An example of this is a person riding a bicycle on a head wind. The bicycle is the frame of reference, which has frame velocity \vec{U} , the wind velocity can be called absolute velocity, we can label it \vec{C} . Clearly the absolute velocity \vec{C} is the velocity that will be experienced by an observer watching the cyclist at the road side. On the other hand, the wind velocity experienced by the cyclist is different and it is called the relative velocity, \vec{W} . By inspection (since head wind) relative velocity \vec{W} can be solved through vector subtraction. ($\vec{W} = \vec{C} - \vec{U}$).

Same analogy above can be applied on rotating compressor handling fluids. Velocity components can be resolved in a free body diagram called velocity triangles. The velocity triangles for an axial compressor stage is shown on Figure 1.3(a). The working fluid (mostly air) approaches the rotor with velocity C_1 at angle α_1 , which is set by the compressor inlet guide vanes or by some other upstream feature. By vector subtraction of the blade speed U , the relative velocity W_1 at angle β_1 is obtained, which must be correctly aligned with the rotor blades for satisfactory operation. In passing through the rotor blade passage, the

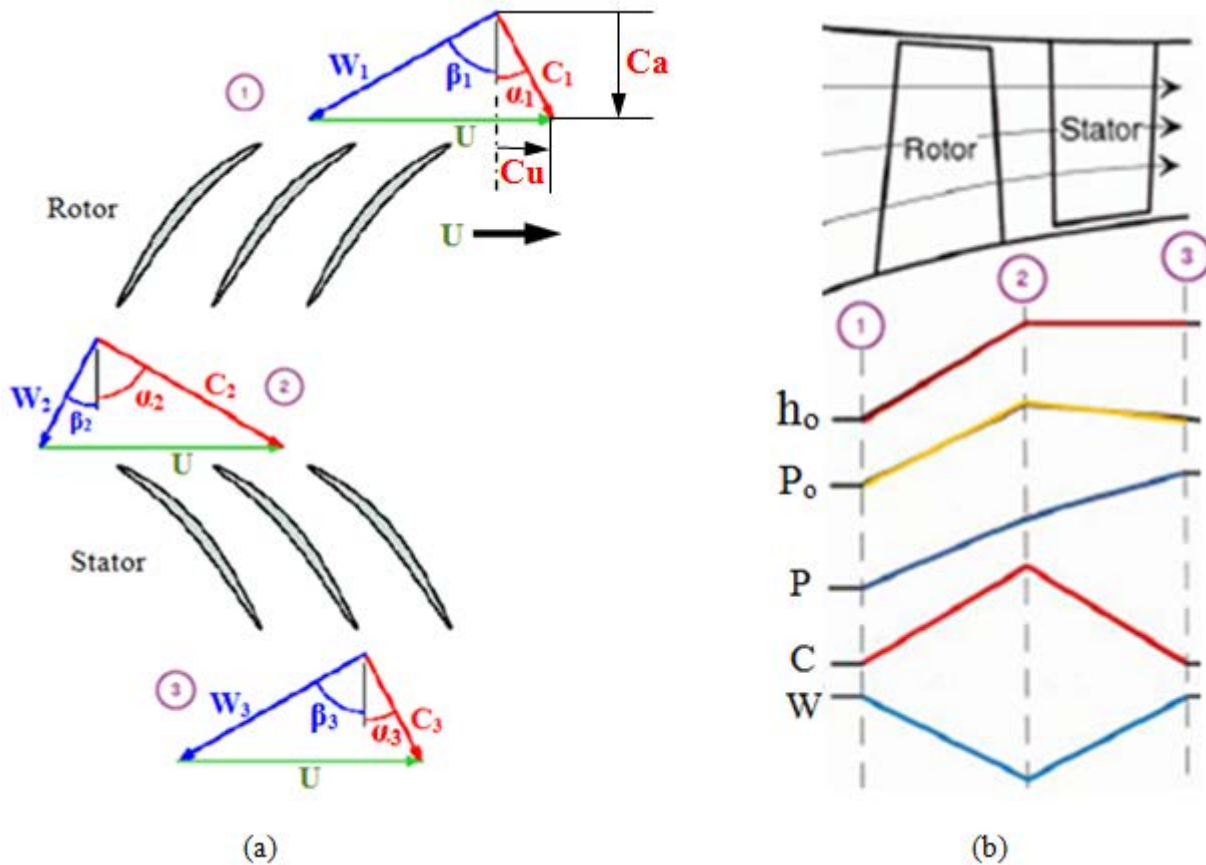


Figure 1. 3 - (a)Velocity triangle of axial compressor (b)Changes in fluid properties in axial compressor

flow is decelerated in the relative frame of reference (viewing flows from the point of view of the rotating component) and emerges at some lower velocity W_2 and angle β_2 . This is by the geometry of the blade at the exit but not exactly equal to the blade exit angle. The difference between the blade and the flow angles is the deviation angle. For more details about blade terminology and cascade notation please refer Figures 1.6 and 1.7.

At the rotor exit, the working fluid approaches the stator with the velocity C_2 and angle α_2 (absolute frame of reference, since stationary blades), obtain by vector addition of the blade speed to the rotor exit relative velocity. As with the rotor, this velocity should be properly aligned with the stator blades. The flow again is diffused through the stator and emerges with velocity C_3 at an angle α_3 . The angle is set by the stator blade angle, but also with some degree of deviation. A typical stage design, is a repeating stage in which C_3 is equal to C_1 and α_3 is equal to α_1 . In addition, it's been common to design stages for constant axial velocity, so that $C_{a1}=C_{a2}=C_{a3}$. A consequence of this, to satisfy continuity, the annulus area of the stage must decrease in the streamwise direction as the pressure and hence the density of the fluid increases. This can be seen on Figure 1.3(b), top most with rotor - stator profile.

Compressor flow is characterized by a deceleration of relative velocities. It can be seen in Figure 1.3(a) the Euler velocity triangles of the rotor stator cascade. The work done by the blade is related to the change in tangential velocity (C_a),

$$W = \Delta h_0 = U(C_{u2} - C_{u1}) \quad (1-3)$$

where, U is the blade velocity, C_u , from velocity triangles (Figure 1.3(a)) equals $C_a \cdot \tan \alpha$.

1.1.2. AXIAL COMPRESSOR COMPRESSION STAGE

The change of properties of the working fluid can be explained using the velocity triangles at inlet and outlet of the rotor and stator blades. Figure 1.3(b) shows the connection between velocity and various thermodynamic properties of the flow, such as absolute and static pressure, enthalpy, axial and relative velocity. As can be seen in the Figure 1.3(b), the absolute velocity C is increased between inlet and outlet of the rotor blades (flow is accelerated), due to energy input via compressor shaft. This results in increased total enthalpy, h_0 over the rotor. Over the stator, there is no work input so that h_0 remains constant. Same reasoning applies to the total pressure, P_0 too, however, due to friction losses over the stator blades certain pressure drop takes place as shown. The static pressure, P is increased in both rotor and stator passage, due to diffuser effect.

Same analysis can be applied, illustrating the compression in a TS-diagram shown on figure 1.4. Two settings, namely total (with subscript pre-fix 0) and static (without prefix) properties are shown in the TS-diagram, where the basic relations as stated above explains the change of properties over the compressor

stage. As one can see the difference between total and static properties are the dynamic values, dictated by

$$\text{changes in the flow velocities. } T_0 = \frac{h_0}{c_p} = T + \frac{C^2}{c_p} \quad (1-4)$$

where: c_p is the constant pressure specific heat, h_0 is the total or stagnation enthalpy, T_0 is the stagnation or total to total temperature and T is the static temperature.

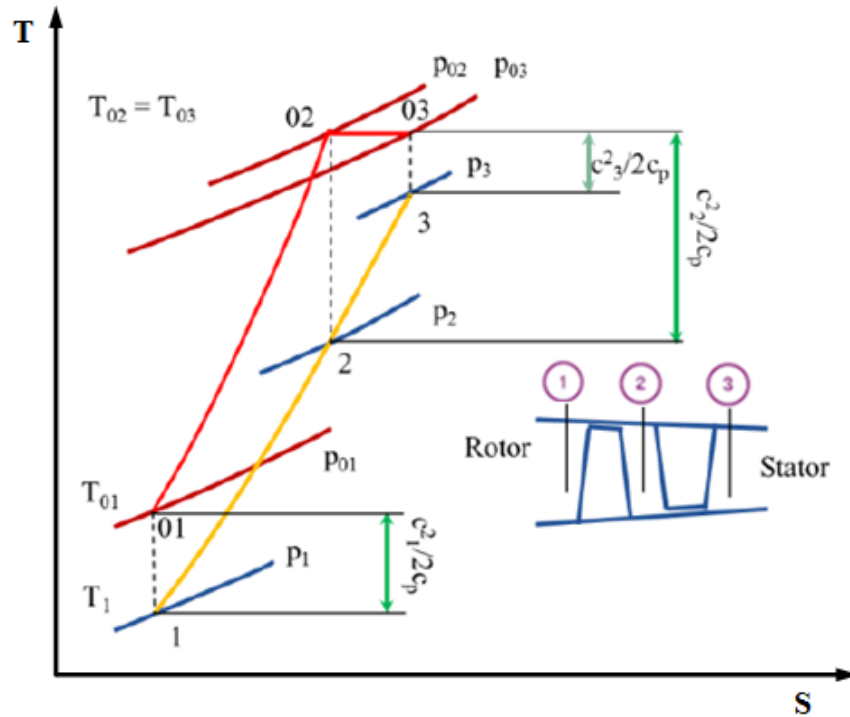


Figure 1. 4 - Temperature-Enthalpy diagram of the compression stage of axial compressor

Base on figure 1.4, stage performance can be analyzed expressing the total temperature change, ΔT_{0S} , of the stage :

$$\Delta T_{0S} = T_{03} - T_{01} = T_{03} - T_{02} = U \cdot C_a (\tan\beta_1 - \tan\beta_2) \quad (1-5)$$

where C_a is the axial component of the absolute velocity C , representing the mass flow, U is the blade speed and $(\tan\beta_1 - \tan\beta_2)$ is the flow deflection, indicating the level of diffusion. To maximize the energy transfer between the blade and the working fluid, one can try to maximize these three parameters. However, there are physical and practical limitation to how much one can increase these values. The blade speed is limited due to mechanical load on the blades, the axial component of the absolute velocity and thereby, the mass flow is limited due to size considerations and the turning of the flow, the diffusion is limited due to stability concerns.

It is important to introduce static and stagnation quantities. Static quantities define a thermodynamic state. Taking the statement base from Anderson(Anderson Jr., 1984): static quantities is what you feel if you were moving with the flow. Total quantities is what you would feel if you're blocking the flow and adiabatically take the velocity to zero. Therefore, the total quantities taking into account kinetic energy($\frac{c^2}{2}$) and it is usually define by total enthalpy(h_0), total pressure(p_0) and total temperature(T_0):

$$h_0 = h + \frac{c^2}{2} \quad (1-6)$$

where: $h = c_p * T$ as static enthalpy, c_p is specific heat at constant pressure and C the magnitude of absolute velocity.

$$p_0 = p^* \left(1 + \frac{\gamma-1}{2} M_a^2\right)^{\frac{\gamma}{\gamma-1}} \quad (1-7)$$

$$T_0 = T^* \left(1 + \frac{\gamma-1}{2} M_a^2\right) \quad (1-8)$$

where, $M_a = \frac{C}{c}$, the Mach Number, $c = \sqrt{\gamma RT}$ is the speed of sound, γ the specific heat ratio and R , is the specific gas constant.

Looking Figure 1.4, it follows that overall aerodynamic parameters can be defined. The adiabatic efficiency(η_a) and the total pressure(P_R) are:

$$\eta_a = \frac{\left(\frac{p_{02}}{p_{01}}\right)^{\frac{\gamma-1}{\gamma}} - 1}{\frac{T_{02}}{T_{01}} - 1} \quad (1-9)$$

$$P_R = \frac{p_{02}}{p_{01}}, \quad (1-10)$$

where subscript 1 and 2 denote inlet and outlet of the rotor, respectively.

Adiabatic or isentropic efficiency(η_a) can be expressed also in terms of compressor isentropic work and actual work, W_s and W_a respectively:

$$\eta_a = \frac{W_s}{W_a} \quad (1-11)$$

$$W_s = mc_p(T_{02-s} - T_{01}) \quad (1-12)$$

$$W_s = mc_p(T_{02} - T_{01}) \quad (1-13)$$

Applying isentropic relationship:

$$\frac{T_{02}}{T_{01}} = \left(\frac{p_{02}}{p_{01}}\right)^{\frac{\gamma-1}{\gamma}} \quad (1-14)$$

Combining equations 1-11 to 1-14, will yield the same efficiency as Equation 1.8 in form:

$$\eta_a = \frac{\left(\frac{p_{02}}{p_{01}}\right)^{\frac{\gamma-1}{\gamma}} - 1}{\frac{T_{02}}{T_{01}} - 1} \quad (1-9 \text{ or } 1-15)$$

Please note that the values taken at point 1 and 2 are in mass average.

1.1.3. COMPRESSOR STABILITY

Compressors are working against the law of nature, i.e. delivering the low pressure working fluid at high pressure at the compressor outlet. Many factors can disturb the flow, resulting in reverse flow and compressor instability. To have a general understanding of how these instabilities develop within the compressor stage and propagate through the component, short discussion below is provided.

There are many parameters, such as mass flow, pressure, temperature, and other properties of the working fluid, which changes between inlet and outlet of the compressor. To provide general analysis tools that help engineers with a general overview over the engine behavior, various dimensionless parameters have been derived. Dimensionless pressure and flow parameters, denoted by ϕ , as flow coefficient and ψ , as pressure or temperature coefficient are useful parameters for analysis of compressor stability.

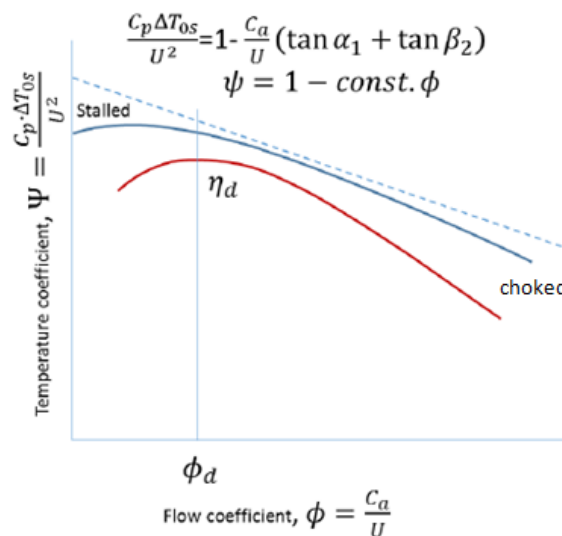


Figure 1. 5 - Compressor Stability

The ideal relationship between pressure coefficient, ψ , and flow coefficient, ϕ , over a stage, which is a first degree equation, is represented by a straight dash line in the Figure 1.5. However, flow coefficient ϕ , at higher and lower flows than the design flow, ϕ_d , deviation between the ideal and real case increases, indicated by the blue curve in the figure above. The design case efficiency η_d , represented by the red curve, which is at its maximum at design flow drops and the risk for instability increases.

1.1.4. BLADE CASCADE NOTATION AND TERMINOLOGY

Figure 1.6 below, shows cascade nomenclature with the inlet and outlet station labeled 1 and 2 on the subscript with absolute velocities C and air angles, α used. In addition, Figure 1.7 are blade terminologies for reference terms used throughout this work.

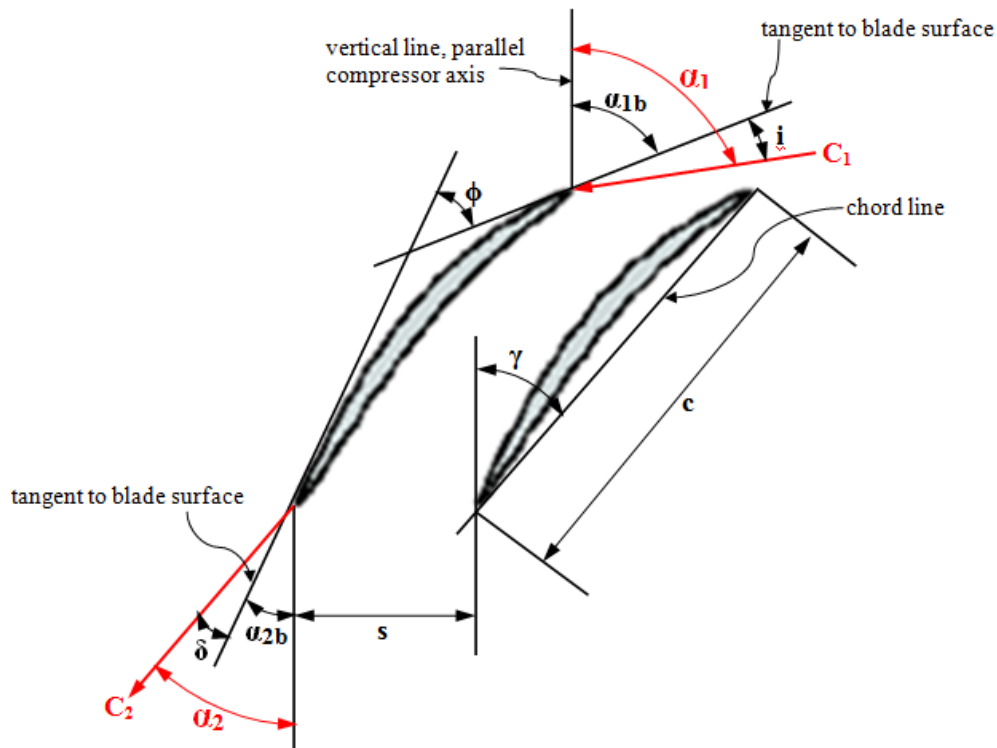


Figure 1. 6 - Blade Cascade notation

From the figure:

$$i = \alpha_1 - \alpha_{1b} \quad \text{air incidence angle}$$

$$\delta = \alpha_2 - \alpha_{2b} \quad \text{air deviation angle}$$

$$\text{AOA} = \alpha_1 - \gamma \quad \text{air angle of attack}$$

$$\Theta = \alpha_1 - \alpha_2 \quad \text{air turning angle}$$

Other variable terms are:

C - air absolute velocities

α - air angles (note: positive α measured in cascade becomes negative β when applied to rotor)

γ - blade stagger angle

σ - solidity or (aspect ratio) pitch/chord ratio or $\frac{s}{c}$

s - blade pitch

c - blade chord

ϕ - blade camber angle

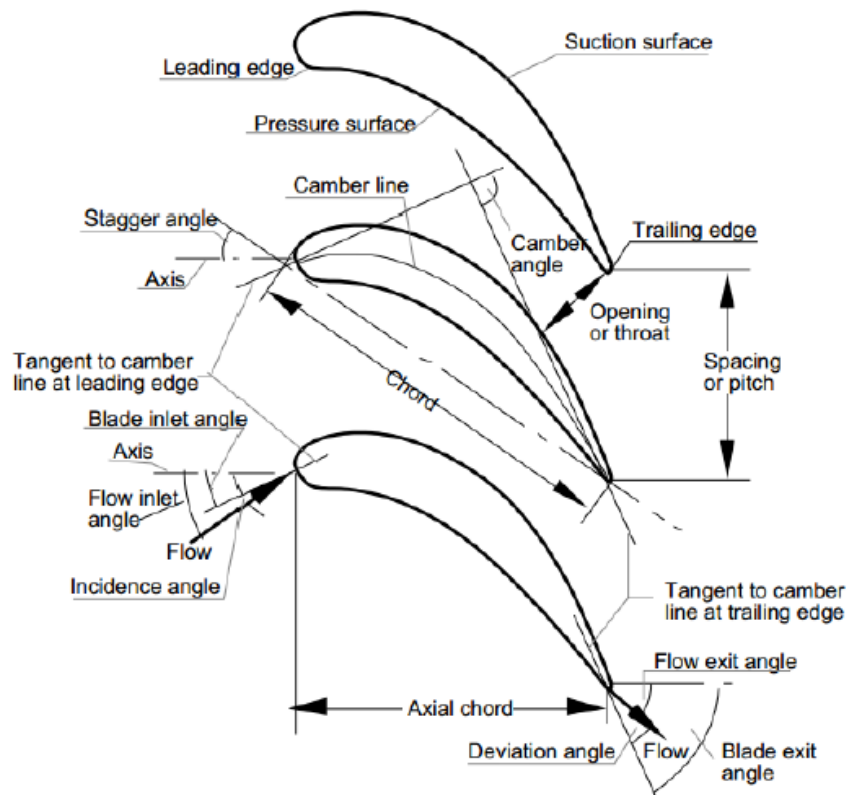


Figure 1.7 - Blade Terminology

Source: <http://en.wikipedia.org/wiki/Images>

1.2. COMPRESSOR INSTABILITY

Compressors operate against the law of nature where fluids are sucked at inlet and should be delivered at outlet, higher than the inlet pressure. The complicated nature of the field plus a high blade loading on achieving high compression ratios makes it hard to establish a large operating range sufficiently. The useful operating range of the compressors is only limited both at very high and very low mass flow rates. There is always a certain range to be achieved in order to ensure consistent performance that compressors are designed for all applications. Beyond this certain range, occurrence of strong shock waves and the *flow*

chokes at high mass flow rates is one of its limitations mentioned earlier leading to significant reduction of efficiency. On the other hand, at low mass flow rates, the compressor is limited by the initiation of aerodynamic instabilities called *stall*. Instabilities like this are characterized by the occurrence of limit cycle vibrations and strong fluctuations in the flow properties and mass flow rates. Continuous oscillations can lead to blade fatigue and engine failure which can lead into some catastrophic incident. Therefore, the major aspect of design and performance predictions must be understood by the designer related to aerodynamic instabilities and stall propagation. It also must be avoided at all costs.

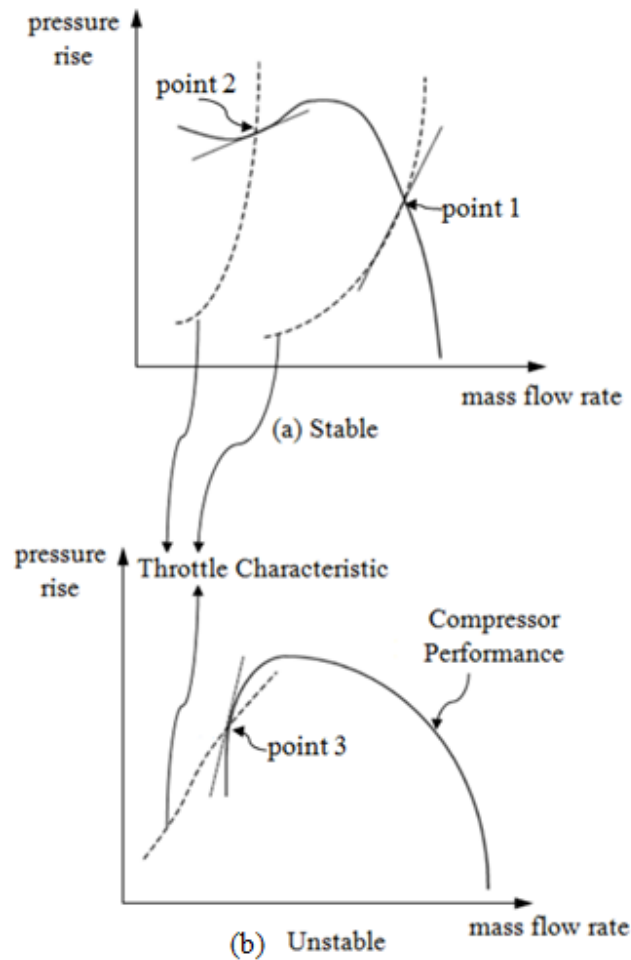


Figure 1. 8 - Operational Stability. Matching Compressor Characteristics and Throttle Characteristics

Compressors have the ability to recover from disturbances that alter its operational equilibrium point during operation, this refers to as the compressor's stability. This disturbance may be transient or deliberate changes to its operating point. The system is unstable if the disturbance drives away the compressor from its original point. This is obvious for a compressor being driven by the turbine shaft and the operating curve has point match changes than can be observed due to the transient change of mass flow. When there is deliberate changes to the operating point after changing the compressor shaft speed and new equilibrium

is achieved, the compressor performance is stable as shown in Figure 1.8(a) where pressure recovers at point 2. When new operating point cannot be achieved as in point 3 in Figure 1.8(b), it is unstable. In practical sense, this can be observed during actual compressor operation that the compressor produce irregular disturbing sound.

Studies of compressor stability can be classified into two: operational stability and aerodynamic stability. Operational stability deals with the used of throttle valve or throttle sensors place at the downstream flow and compressor performance are match with compressor performance map versus the compressor characteristics actual result plots. The aerodynamic stability deals with the abrupt deterioration of performance due to stall, flow separation and choked flow that can be observed on humming noise and violent vibrations during operation.

A typical performance map is shown in Figure 1.9. Stall or surge line is represented by the dash line. A parallel line down to the right is the surge avoidance line. Occurrence of surge or stall, is not always after the stall line to the left direction but may still occur before and right side of stall line(in the figure 1.9) if the flow is unstable due to instability. So the surge avoidance line serves as safety margin for the compressor operation to ensure that it is operating away from the region that stall or surge may occur. Another reason why surge avoidance line is introduce is because compressor operational characteristics can be biased to a higher degree that the surge line may be poorly known. As mention earlier, there is always a limit on compressor operational performance, compressor operating point near surge line has a benefit of higher pressure ratio but a greater risk of stalling.

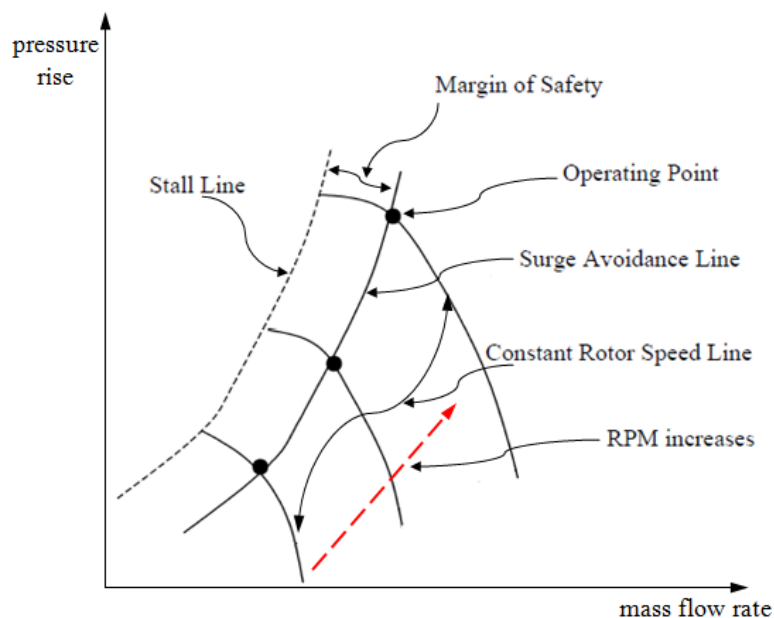


Figure 1. 9 - Typical Compressor Performance Map, Emphasis on the Effect of Compressor Speeds

1.3. AXIAL COMPRESSOR BASIC OPERATION

In axial compressors, fluid flow enters and exits in axial direction. Compressors can be a single stage or multi stage (one pair of rotor stator only, or more than one pair, respectively). A single stage of axial compressor is shown in Figure 1.10. Each stage is made up of rotor blades and a row of stator blades (Figure 1.10(a)). The basic mechanism of operation is shown in Figure 1.11. At the rotor, the energy is transferred from the rotating blades to the passing fluids and the fluid accelerates. As the fluid reaches stator section, fluid flow decelerates as it passes through diverging nozzles and the kinetic energy is converted into pressure energy. There is work exerted by the stage to the fluids and subsequently compresses the working fluids through the series of progressive converging passage channels (Figure 1.10(b)), resulting in an increase of its stagnation and static pressure. The pressure rise is dependent on the work done by the rotor on the fluid flow and also with the degree of how fluids decelerates through the stator. Thus the pressure ratio of the multi-stage compressor is much higher compared to the single stage compressor but for the expense of the overall efficiency, notwithstanding the weight and cost also.

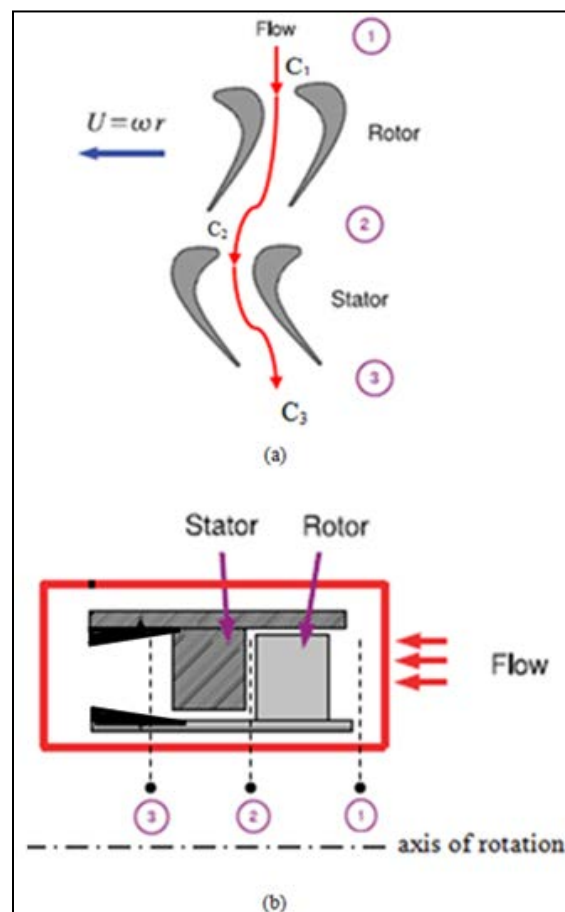


Figure 1. 10 - Single Stage of Axial Compressor

(a) Cylindrical section view (b) Axial section view

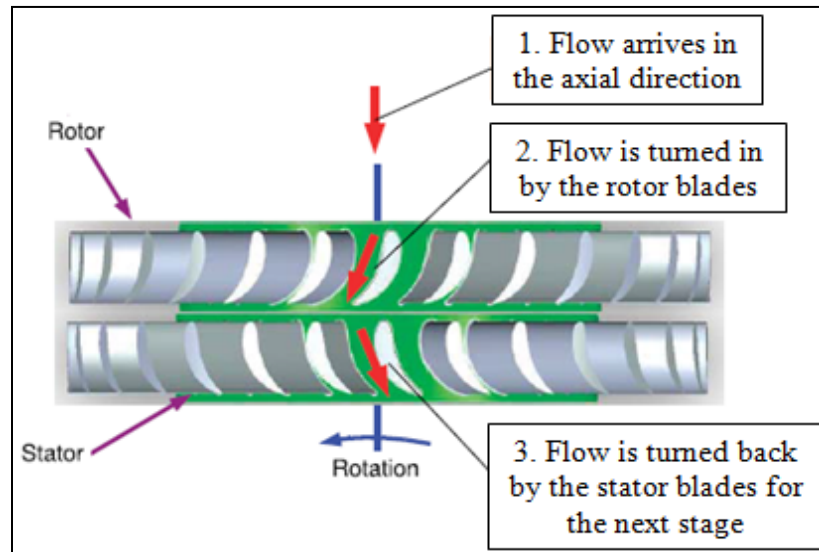


Figure 1. 11 - Axial Compressor Basic Mechanism of Operation

Modern axial compressors operations are very complex due to the fact that the flow is inherently three dimensional and transient cause by the relative motion between successive cascades of blades rows and the viscous effects in each stages. Sub-sonic and supersonic flow coexist in a region where flow is transonic under Mach number greater that unity. This happens usually near the rotor tip leading edge where the highest blade velocity is combined with the flow axial fluid velocity, leading to the formation of a system shock waves and three dimensional shock boundary layer interactions.

1.4. OBJECTIVES AND ORGANIZATION OF THE PRESENT WORK

The main objectives of this study is to understand the governing physics of the axial compressor stall and chalk during operation. Physical phenomena, theories and mathematical formulation will be dig deeper on the succeeding sections and chapters as part of the motivation to gain understanding and knowledge. Physical phenomena and the theories will be done through literature research while the physics and mathematical formulation of the stall and chalk phenomenon will be aided with computational fluid dynamics(CFD) as visualization tool to support and verify understanding on the pre-determined result.

Therefore the main take away on the authors academic gain and learning's are the following:

- Fluid dynamics in axial compressor air flow.
- Computational fluid dynamics modeling using CFD tool.
- Using and running CFD(Open-FOAM) tool on fluid flow actual test case problem.

Numerous progress in the area of stall and chocked modeling in axial compressors had been done in the past one to two decades, this work will try to add contribution on flow visualizations necessary for understanding the nature of stall and chocked instabilities.

This thesis is organized in the following manner: Discussion of stall and chock phenomena base on technical perspective is presented in Chapter 2. Governing mathematical formulas and equations for numerical simulation is introduced in Chapter 3. Chapter 4, presents the test case rotor and the numerical methods involved in setting up fluid flow case problems and simulating into CFD tool. Results and discussion of the compressor operating points and stall inception studies are presented in chapter 5. Conclusions from this work and possible future work are given in chapter 6.

CHAPTER 2: LITERATURE REVIEW

In this chapter, review about instabilities currently studied will be discuss. Related research work about compressor stall and choke will be presented. Review of Computational Fluid Dynamics(CFD) technique and the interface boundary condition implementation to CFD were studied and discussed. It is also important to include turbulence modeling topic discussed in this chapter since we are dealing instabilities in turbulent state.

2.1. FUNDAMENTALS OF ROTATING STALL

As been discuss, the stability of compressor is base on its performance map and has limitation due to instabilities. Manifestation on this instabilities can be the rotating stall and chalk. We will elaborate further on the proceeding sections. Airflow through the compressor at rotating coordinate system is initially steady. Supposedly, instability is introduced by changing the rotor speed, flow separation and other type of flow distortion ensued. Sign of compressor performance deterioration can lead mild stall or choke at the initial state depending on speed change. At this point the flow is no longer uniform in the axial direction. And it is only a matter of seconds for the stall to build up and if not remedied immediately, damage will be inevitable. Stall and choke can happen actually on both compressible and incompressible fluids.

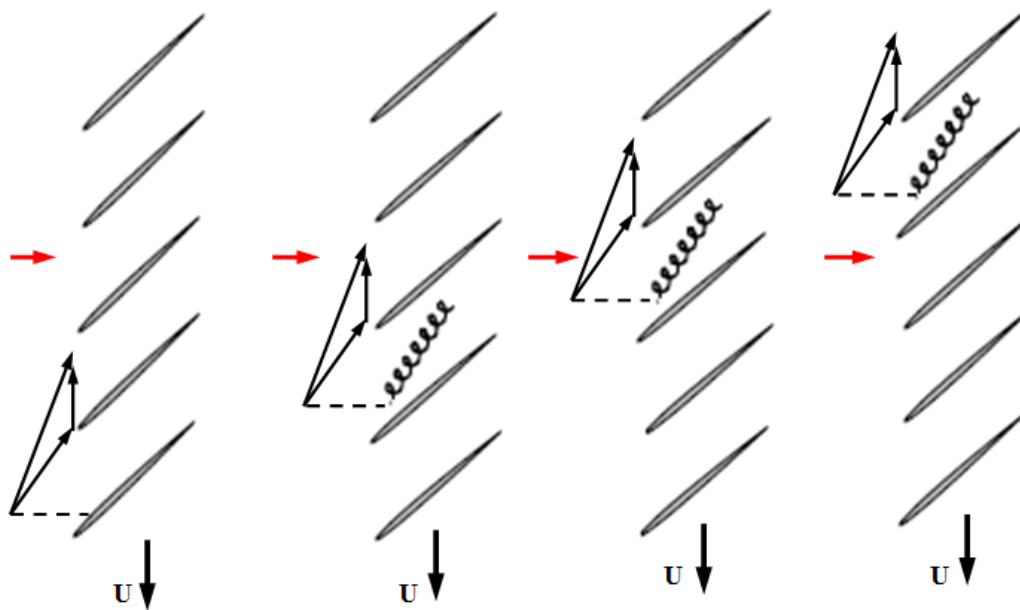


Figure 2. 1 - Rotating Stall Propagation(Individual column of blades defecting stall development)

The development of stall is shown in Figure 2.1. This representation is a single row of blade viewed from the top showing how stall propagates in time. At some point stall is present on the certain blade passage. It is still unknown, and uncertain why stall does not happen on all blades at the same instance as

shown on the figure. One possible hypothesis is dimensional tolerance.(Pampreen, 1993) Another possibility may be that the few blades are produced with different profiles, in short, manufacturing imperfections or could be blades are produced at higher stagger angles. This could cause inlet air non-uniform angle of attack compared with the other blades. If this results one blade to stall, the flow angle relative to its axis increases, in addition there is blockage due to stall at the beginning, causing some of incoming flows diverted towards neighboring blades. This increases more the angle of attack and more blockage. Normal flow fortunately occur over that blade as it rotates since it moves away from the disturbance thus it recovers from high angle of attack to low angle of attack. But the neighboring blade passage that the stall transferred cause by the higher angle of attack mention above still operating in stalled flow region(stall cell) and continuously moving from that blade to the other and propagates around the annulus leading to a complete stall. The stall cell propagates in the same direction as the blade rotation in the inertial coordinate system. However, rotating stall moves in opposite direction to the blade rotation at a fraction of the blade speed with respect to axial coordinate system. It varies from 20 to 75% of the blade speed along the blade rotational motion(de Jager, 1995). This rotating stall cells had reportedly move faster also with typical frequencies from 10 to 50 times larger of those fully developed stall.

Typically stall cells have been reported to be one to nine stalled cells depending on the type of compressor. Stalled cells can be either abrupt or progressive. The later has gradual reduction of pressure ratio after the stall while the former has a sudden drop across entry and exit pressure and often happens in a single stalled region.

The average flow is steady with respect to time is one characteristics of stall but has non uniform mass decrease over its circumferential regions. This results cyclic imbalance of pressure along the blades that would cause fatigue vibrations that will eventually break the blade over time. The non-uniform distribution of shaft work leads to temperature increase that reduces blade life.

There are several types of rotating stall base from de Jager(de Jager, 1995): Full span stall(Figure 2.2(Pampreen, 1993) where entire height is stalled along the annulus in different regions. Part span(Figure 2.3(Pampreen, 1993) where stalled regions usually at the tip of the blades. And small or large scale span which is a combination of the two where small or large part of the annular flow path is blocked.

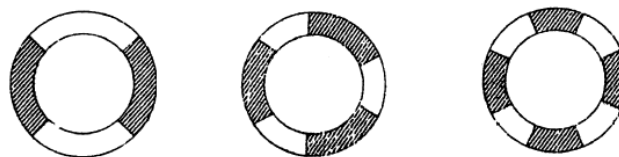


Figure 2. 2 - Full-Span Stall(Pampreen, 1993), viewed in axial direction

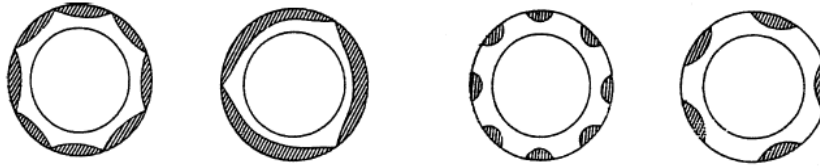


Figure 2.3 - Part-Span Stall(Pampreen, 1993), viewed in axial direction

Looking back at Figure 1.8, where onset of rotating stall can generate a sequence of pattern. When at point 2(Figure 1.8(a)) at the un-stalled, the tendency of the point to proceed to the stalled characteristics at point 3(Figure 1.8(b)) can occur and remain to operate on that point until measure is taken on the compressor to recover and bring back to point 2. Detection of this stall formation cannot be easily noticed except for the loud noise and irregular vibration or by some sophisticated sensors and if left for a period of time can be a precursor to a more dangerous and severe flow stability higher than stall, which is often called surge.

2.2. THE CONCEPT OF SURGE

Surge flow exhibit when flow of incidence in compressor blades starts to misaligned with their metallic angles, often resulted separation that produces losses and instability. This is closely related to stall phenomena and usually happens with low mass flow and airflow can simply stop, entering a surge cycle.

The behavior of surge attributed its characteristics on the type of compressors and the diffusers(de Jager, 1995). In high speed compressors shock wave is present while in low speed compressors, surge appears as in moderate pulse.

From pressure fluctuations and fluid flow perspective, there are four classes of surge(de Jager, 1995). Mild surge where no flow reversal, small periodic fluctuations of pressure base on Helmholtz resonance frequency. Second is classic surge is at lower frequency but has large oscillations, still no flow reversal. Third is modified surge, it is a combination of stall and classic surge. This is governed with non-axis symmetric flow in the entire annulus. The last one is deep surge, this is a strong version of classic surge where flow reversal is high and axis-symmetric flow.

At constant rotor speed, increasing the pressure at the exit of the plenum may cause mild surge to occur. This may followed by a modified surge that could develop further into deep surge.

2.3. FUNDAMENTALS CHOKED FLOW

Choked occurs with high mass flow at a point where passage blades are blocked that fluids cannot flow freely where in some cases flow reversal happens since delivery pressure drop significantly lower than the inlet pressure. Choked is a local instability that could affect the whole compression system. It is characterized by large amplitude cycle oscillations in mass flow rate. As mention, a complete flow reversal is possible. In contrast to stall, the average flow through the compressor is unsteady but the

circumferential flow is uniform. A lot of conditions during stall can also be present in choked like rotor blades are stressed due to oscillation and unbalance shaft work distribution. In addition, back pressure increases higher than the delivery pressure.

Choked flows are formed when there is a section in the flow passage area reaching a $Ma = 1$. It is elaborated for isentropic flows(White, 1994) that this critical flow area imposes a maximum mass flow. It is obvious that this phenomena must be seriously considered when designing a flow passage and more precisely on a turbo machine because as been mention, mass flow will always be limited.

2.3.1. COMPRESSIBLE FLOW

When fluid velocity is above Mach(Ma) number of 0.3, it is considered compressible flow. Mach number is comparable with the sound velocity, Ma is equal to one when fluids speed equals sound speed. In air, sound velocity is a function of state(such as a function of static temperature(T)). In transonic region, which this study falls into, is in the characteristic range between $0.8 < Ma < 1.2$. In such flows the following phenomena can happen: choked flows, surge flows and shock waves occurs.

Shock waves(AndersonJr., 1984) exhibits when flow enters at transonic state and are characterized by a thermodynamic state discontinuity. Usually velocity decreases with an increase of static pressure(p) and static temperature(T). This really provoke compression, which is the purpose of the compressor but are mainly a source of losses and noise. In a wall bounded flows such as happening in axial compressor region, shock waves are more complex due to interaction of the wall boundary layer. Flow reversal can be due to a shock wave(Sebghati, 1992) in high speed compressor operation. There is a high pressure behind the shock wave that can deform the casing and inlet. Rotational moments can then alter the twist of the rotor and blades.

2.4. ON ROTATING STALL AND SURGE - A LITERATURE SURVEY

Earlier research about stall and surge were based on the assumption of incompressible flow. Later on, there were successful attempt that featured compressibility and two dimensional flow on the work of Bonnaure((Bonnaure, 1991). Further work on non-linear methods of instabilities can be found on the two works of McCaughan(McCaughan, 1989a, 1989b).

As mentioned, the flow inception behind stall is not well understood both on high speed and low speed compressors. Studies about flow inception on high speed compressor was perform by He et al.,(1997). They numerically simulated stall in an isolated compressor blade row. The result they found was that the stall of supersonic inflow usually occur in one dimensional surge like pattern without experiencing rotating stall at first.

Another numerical simulation on stall inception was conducted by Niazi et al.,(2000) in an isolated transonic compressor blade row. Result showed that at low mass flow rates, leakage at the tip section is stronger and the effect of tip shock interaction leads to compressor stall. They able to control stall back to normal state by incorporating bleed valves at the diffuser walls as a means of stall/surge control.

Related numerical studies conducted by Hah et al.,(2004) using RANS analysis for isolated transonic compressor rotor produced indication that axial velocity has similarity to the stall signals captured from pressure transducers mounted upstream of rotor. It was revealed that the shock in axial position were detached from the rotor blade and varies from blade to blade and that this non-uniform shock triggers onset of stall.

Stall mechanism in an isolated transonic axial compressor rotor with different tip gap heights settings were studied by Haixin et al.,(2006). It was found out that both small tip gap at the trailing edge and large tip gap at the leading edge triggers stalls. Other researchers, Grietzer et al.,(1993) and Chima(1996) also studied similar setting and found out that various effects of different tip clearances on the flow field produced similar outcome of stall inception.

In addition, many experimental works have been attempted to detect stall and surge build up such the work of Indue et al.,(1991) and Lawless et al.,(1994). Precursor to stall and surge inception by collecting data of pressure signals based on correlation scheme done experimentally by the work of Dhingra et al.,(2003). The data were taken from both high and low speed compressor for comparison and the result showed consistent behavior for different rotor speeds. One important technique they found out was the proper location of the sensor.

2.5. COMPUTATIONAL STUDIES OF COMPRESSOR FLOW

In the design and analysis of fluid flow specially involving complex operation such that of a turbo machinery, computational technique through computational fluid dynamics have been widely used. In the early years, most of the work done was two dimensional potential flow solutions due to the limitations of the computational resources, meshing technique, three dimensional discretization schemes and stable time marching scheme. In addition, required thorough validation and some other aspects were not ready.

Effort to improved numerical technique increased in the course of time. Number of scientific research to achieved breakthrough continued up until the present. MacCormack(MacCormack, 1969) successfully developed technique to integrate Navier-Stokes equation. Followed by meshing and grid generation technique development around general two dimensional and three dimensional geometry configurations. Then, stable implicit time marching were introduced successfully and used by Briley et al., (1984) and Beam et al.,(1978). These development, associated with the increase in the computer processing speed and

storage led the revolution of Computational Fluid Dynamic(CFD) studies. Further improvements of CFD techniques led to the ability of investigating flow fields around three dimensional and multiple row blades in real time. Studying instabilities, what limits its operating range and other problems can now be simulated and can be answered through CFD(Chima, 1987), (Chima, 1992), &(Hathaway, 1987).

Therefore CFD technique plays very important role in the design and analysis of compressor operations. Applications for different fluid flow problem cases both internal or external flows were performed using CFD.

2.6. TURBULENCE MODELING OF FLOW IN CFD

The physics behind onset of stall in axial compressor is complicated and to produce accurate result, high resolution turbulence model is necessary. As the compressor operate towards stall, flow separation occurs, large eddies and wakes start to grow thicker and thicker. Predicting such flows requires turbulence models that would resemble closely and capture the scenario accurately.

Most CFD methods used in the simulation and analysis of stall in axial compressors are based on Reynolds Averaged Navier-Stokes(RANS) approach, in which time-averaged mean effects are solved and turbulence closure models are used to provide the flow field turbulent effects, such the eddy viscosity, turbulent wake etc..

Base on number of additional equations used in the estimation of the flow turbulent viscosity, RANS closure model were divided in several forms. Spalart-Allmaras(Spalart & Allmaras,(1994)) model derived Navier - Stokes equation which transport equation for the turbulent viscosity or the turbulent kinetic energy is solved with length scales empirically specified. Specifying empirical length scales cannot be so appropriate for complex turbulent flows. To solved these issue two equation models were made which two transport equations for two turbulent variables(turbulent kinetic energy and turbulent dissipation rate) are solved to estimate the flow field base on the predicted length scale and velocity scale. This is how k- ϵ model(Jones et al.,(1972)) was established which solved the turbulent kinetic energy(k) and turbulent dissipation energy(ϵ). Similar two equation solution was presented by Wilcox(Wilcox, 1988), known as k- ω model that introduced new term on the second variable which solved the turbulent dissipation rate(ω). Menter's k- ω -SST(Shear Stress Transport) model(Menter, 1994) solved Wilcox's k- ω model on near wall turbulent properties and switch to k- ϵ model to solved turbulent properties that are away/far from the wall. Base on the evolution of the RANS closure model discuss above, Menter's k- ω -SST(Shear Stress Transport) is appropriate choice to be used on this work. More details of this on the next chapter.

2.7. BOUNDARY CONDITION ON STUDIED DOMAIN

In axial compressor, the physics on stall inception is very complex, and there is a need to capture phenomena in an accurate physical interpretation of system working process. One that should be look into is the proper domain(rotor-stator) boundary condition used in the simulation. The flow field complexities is inherent by unsteady and three dimensional interactions between adjacent row blades. One major drawback, in simulating flow through multiple blade rows is the relative motion on the domain be it at rotor or at the stator blades(Rai). To avoid false reflections of the system work, stable and accurate boundary conditions must be used to capture correct local and global fluxes on the rotor or stator interface. There are works that models boundary conditions on the flow through series of rotor-stator cascades in turbo machineries(Wyss) et al.), (Denton, 1990) & Saxer et al.,(1994). These are the isolated blade row analysis, averaging plane methods, averaging passage methods and fully unsteady methods.

In this work, we adapt the single averaging passage method. On this set-up single blade or vane from inlet to exit were solved all corresponding fluxes from upstream to downstream. This method allows solving the blade rows and does not model any of the transient interactions between the successive blade rows. Details on the implementation will be covered on the use of the CFD solver on Open Foam(to be discuss on succeeding chapters). The equivalent term related to this approach is called cyclic boundary condition(cyclicGgi in OpenFOAM). This is the most convenient way of solving the compressor domain which lowers the computational time instead of using the entire domain that compose a more than million grid cells. Details of the averaging plane methods, averaging passage methods and fully unsteady methods are discuss on the following work references: [(Wyss) et al.), (Denton, 1990) & Saxer et al.,(1994), (J. J. Adamczyk, 1985), (Adamczyk et al., (1986), and (Rai)].

CHAPTER 3: NUMERICAL FORMULATION AND CFD TOOLS

The solution of the 3-dimensional Navier-Stokes equations is required to analyzed the flow details in compressors. Due to the complex nature of the governing equations there is a limits for analytical solutions that is why numerical techniques are required. Therefore, numerical formulation and CFD(OpenFOAM) tools employed in this study are documented on this Chapter.

Details of the OpenFOAM solver used can be found in Section 4.5.1, here the numerical methods used to implement the transonic density-based solver will be discuss. In the solver, primitive variables $[\rho, U, p]^T$ (transpose matrix) are reconstructed by a Monotone Upstream-Centered Schemes(MUS)(Leer, 1977). This will return inviscid numerical fluxes after the primitive variables were used as input to the approximate Riemann solver. Euler equations are solve through Godunov scheme(Toro, 1999), and then central difference discretization follows in which the resulting discretized form is nothing more than the conservative Navier-Stokes equation. These will result on a set of algebraic equations which are solved by a direct inversion method(Malalasekera et al. (1995)). For unsteady calculation, time discretization can reach 3rd order, and the *local time-stepping* is implemented as an accelerating convergence technique. The succeeding sections will provide further details.

3.1. NAVIER-STOKES EQUATIONS

The complete form of the N-S presented in the differential form(Reis, 2013) is read

$$\frac{\partial \mathbf{U}}{\partial t} + \nabla \cdot \mathbf{F}_c(\mathbf{U}) = \nabla \cdot \mathbf{F}_d(\mathbf{U}, \nabla \mathbf{U}) \quad (3-1)$$

where \mathbf{U} is a conservative state vector

$$\mathbf{U} = \begin{pmatrix} \rho \\ \rho u \\ p v \\ p w \\ p E \end{pmatrix} \quad (3-2)$$

$\mathbf{F}_c = (F_c^x, F_c^y, F_c^z)$ is the convective flux tensor

$$F_c^x = \begin{pmatrix} \rho u \\ \rho u^2 + p \\ \rho u v \\ \rho u w \\ (\rho E + p)u \end{pmatrix}, F_c^y = \begin{pmatrix} \rho v \\ \rho v u \\ \rho v^2 + p \\ \rho v w \\ (\rho E + p)v \end{pmatrix}, F_c^z = \begin{pmatrix} \rho w \\ \rho w u \\ \rho w v \\ \rho w^2 + p \\ (\rho E + p)w \end{pmatrix} \quad (3-3)$$

Furthermore, $E = p \left[C v T + \frac{1}{2}(u^2 + v^2 + w^2) \right]$

where, $C v$ is the specific heat at constant volume and T is the static temperature. Also, p is static pressure, and is related to total energy and velocities below:

$$p = \rho RT \quad (3-4)$$

$$p = (\gamma - 1) \left[E - \frac{1}{2} \rho (u^2 + v^2 + w^2) \right] \quad (3-5)$$

In Equation (3-5), γ is the specific heat ratio, equivalent to 1.4 for air.

$\mathbf{F}_d = (F_d^x, F_d^y, F_d^z)$ is the dissipative flux tensor

$$F_d^x = \begin{pmatrix} 0 \\ \tau_{xx} \\ \tau_{xy} \\ \tau_{xz} \\ u\tau_{xx} + v\tau_{xy} + w\tau_{xz} + q_x \end{pmatrix}, F_d^y = \begin{pmatrix} 0 \\ \tau_{yx} \\ \tau_{yy} \\ \tau_{yz} \\ u\tau_{yx} + v\tau_{yy} + w\tau_{yz} + q_y \end{pmatrix}, \quad (3-6)$$

$$F_d^z = \begin{pmatrix} 0 \\ \tau_{zx} \\ \tau_{zy} \\ \tau_{zz} \\ u\tau_{zx} + v\tau_{zy} + w\tau_{zz} + q_z \end{pmatrix}$$

and τ_{ij} the dissipative stress tensor

$$\tau_{ij} = \begin{pmatrix} \tau_{xx} & \tau_{xy} & \tau_{xz} \\ \tau_{yx} & \tau_{yy} & \tau_{yz} \\ \tau_{zx} & \tau_{zy} & \tau_{zz} \end{pmatrix} \quad (3-7)$$

are considered symmetric and a linear function of velocity gradients due to Newtonian fluid assumptions (Malalasekera et al. (1995)).

In addition,

$$\begin{aligned} \tau_{xx} &= \lambda(u_x + v_y + w_z) + 2\mu u_x \\ \tau_{xy} &= \tau_{yx} = \mu(u_y + v_x) \\ \tau_{xz} &= \tau_{zx} = \mu(u_z + w_x) \\ \tau_{yy} &= \lambda(u_x + v_y + w_z) + 2\mu u_y \\ \tau_{yz} &= \tau_{zy} = \mu(v_z + w_y) \end{aligned} \quad (3-8)$$

and

$$q_x = -k \frac{\partial T}{\partial x}$$

$$q_y = -k \frac{\partial T}{\partial y} \quad (3-9)$$

$$q_z = -k \frac{\partial T}{\partial z}$$

In these equations, μ is the molecular viscosity and k is the thermal heat conduction coefficient of the fluid. In Equation (3-9), λ , from the Stokes hypothesis, is $-\frac{2}{3}\mu$.

All quantities in the Navier-Stokes equations have been non-dimensionalized by their corresponding reference values. The following reference parameters have been used:

$$L_{ref} = \text{Diameter of the rotor, at the blade trailing edge}$$

$$V_{ref} = a_{ambient, upstream of the inlet} = a_\infty$$

$$\rho_{ref} = \rho_{ambient, upstream of the inlet} = \rho_\infty \quad (3-10)$$

$$p_{ref} = \frac{\rho_{ref} V_{ref}^2}{\gamma}$$

Navier-Stokes equations becomes Euler equations if viscosity and thermal conduction is neglected which are solved first by Godunov for compressible flow (Toro, 1999). When dealing with problems that admit discontinuities such as shocks, it becomes necessary to solve the N-S equations in a conservative form so that convergence of solution is certain (Wendroff et al. (1964)).

3.2. RANS EQUATIONS IN A ROTATING FRAME OF REFERENCE

In order to solve turbulence, the transonic density-based libraries are implemented under the N-S equations with mean flow quantities: the so called Reynolds-Average Navier-Stokes (RANS) equations becomes Favre-average Navier-Stokes equation with little variation from the former due to compressible flow solution. In principle, time average of the quantities, its variant uses a mass-average because density changes in a compressible flows. This work will used the Favre equations but in reference to the Reynolds-Average Navier-Stokes equation remain the same.

To define the flow quantities of RANS:

$$A = \tilde{A} + A'' \quad (3-11)$$

where the double prime is the fluctuation and the tilde is the mass-average quantity and has the form

$$\tilde{A} = \frac{\overline{\rho A}}{\bar{\rho}} \quad (3-12)$$

with

$$\overline{\rho A} \equiv \frac{1}{\Delta t} \int_{t_0}^{t_0 + \Delta t} \rho A dt. \quad (3-13)$$

Eq. 3-1 expanded with Eq. 3-11 gives place to the RANS equations, see William(William).The following pseudo heat fluxes and stresses appear (also called Reynolds Stress)

$$(\tau_{ij})_{Turb} = -\overline{\rho u_i'' u_j''} \quad (3-14)$$

$$(q_j)_{Turb} = -C_p \overline{T'' \rho u_j''}. \quad (3-15)$$

The closure model of the RANS equations is made by expressing the Reynolds stress (Eq. 3-14) with the mean quantities. This is done with a linear relation between Reynolds stress and the mean strain tensor S_{ij} when applied to the well known turbulence model, (k- ω (SST)) for this work(Wilcox, 1988).

$$S_{ij} = \frac{1}{2} \left[\frac{\partial \tilde{U}_i}{\partial x_j} + \frac{\partial \tilde{U}_j}{\partial x_i} \right] \quad (3-16)$$

that is read,
$$(\tau_{ij})_{Turb} = -2\mu_{Turb} \left(S_{ij} - \frac{1}{3} \frac{\partial \tilde{U}_k}{\partial x_k} \delta_{ij} \right) + \frac{2}{3} \tilde{\rho} \tilde{K} \delta_{ij}. \quad (3-17)$$

Eq. 3-17 is the same with the linear constitutive equation for Newtonian flows

$$(\tau_{ij})_{Lam} = -2\mu_{Lam} \left(S_{ij} - \frac{1}{3} \frac{\partial \tilde{U}_k}{\partial x_k} \delta_{ij} \right), \quad (3-18)$$

being $(\tau_{ij})_{Lam}$ the laminar stress tensor: this analogy is called Boussinesq hypothesis(Schmitt, 2007).

Note the last term in Eq. 3-17 is added to correct the trace of Reynolds stress(Eisfeld, 2006).

3.3. RANS NUMERICAL FORMULATION IN OPENFOAM SOLVER

RANS equation in OpenFOAM were written in vectorial form, where quantities are already in the mean value(Göncü et al. (2005)). This is express in the following equation below base on (Borm et al.(2011)):

$$\frac{\partial \rho}{\partial t} + \nabla \cdot (\rho \vec{U}_{rel}) = 0$$

$$\frac{\partial \rho \vec{U}}{\partial t} + \nabla \cdot (\rho \vec{U}_{rel} \otimes \vec{U}) + \nabla p = -\rho(\omega \times \vec{U}) + \nabla \cdot \sigma$$

$$\frac{\partial \rho E}{\partial t} + \nabla \cdot ((\rho E + p) \vec{U}_{rel} + p \vec{U}_{rot}) = \nabla \cdot (\sigma \cdot \vec{U}) - \nabla \cdot \vec{q} + \nabla \cdot (\mu + \beta^* \nabla K) \quad (3-19)$$

$$\sigma = (\mu_{Turb} + \mu_{Lam})(\nabla \vec{U} + (\nabla \vec{U})^T) - \frac{2}{3}(\nabla \cdot \vec{U})\delta_{ij} - \frac{2}{3}\rho K \delta_{ij} \quad (3-20)$$

Equation 3-20 is the total shear stress tensor which is the sum of Equations 3-17 and 3-18. It is usually called effective turbulent quantity(Landmann, 2008).

3.1. HYPERBOLIC SOLUTION

Borm et al.(Borm et al.(2011)) formulated these equations for a transonic density-based solver implemented in OpenFOAM. It uses Approximate Reimann Solver(ARS) to calculate the inter-cell's flux based on characteristic's speed. Then, a Godunov scheme solves the hyperbolic system.

3.1.1. GODUNOV SCHEME

The Godunov scheme can be written in the conservative form (Toro, 1999)

$$\mathbf{U}_i^{n+1} = \mathbf{U}_i^n + \frac{\Delta t}{\Delta x} (\mathbf{F}_{i-1/2} - \mathbf{F}_{i+1/2}). \quad (3-21)$$

One must consider the following conservative form of the 1dimensional Euler equations, to understand how the Godunov scheme is assembled:

$$\mathbf{U}_t + \mathbf{F}(\mathbf{U})_x = 0, \quad (3-22)$$

with the conservative state vector and the flux

$$\mathbf{U} = \begin{pmatrix} \rho \\ \rho u \\ \rho E \end{pmatrix} \quad \mathbf{F} = \begin{pmatrix} \rho u \\ \rho u^2 + p \\ (\rho E + p)u \end{pmatrix} \quad (3-23)$$

One can divide the spacial domain in N computing cells $I_i = [x_{i-1/2}, x_{i+1/2}]$ of length $\Delta x = [x_{i+1/2} - x_{i-1/2}]$ with a "height" of $\Delta t = [t^n - t^{n+1}]$ (Figure 3.40). Integrating Eq. 3-22 on cell I_i , first in space and then in time, it results will be the following:

$$\int_{x_{i-1/2}}^{x_{i+1/2}} \mathbf{U}(x, t^{n+1}) dx = \int_{x_{i-1/2}}^{x_{i+1/2}} \mathbf{U}(x, t^n) dx + \int_t^{t+1} \mathbf{F}(\mathbf{U}(x_{i-1/2}, t)) - \int_t^{t+1} \mathbf{F}(\mathbf{U}(x_{i+1/2}, t)) \quad (3-24)$$

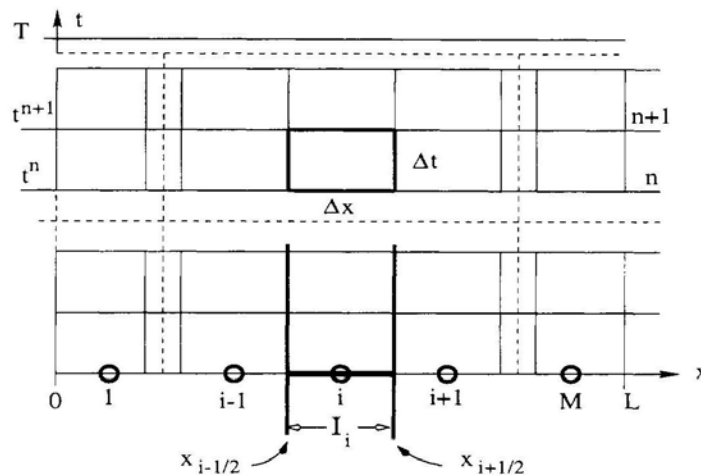


Figure 3. 1 - Descrization of mesh cells (Toro, 1999)

The Godunov scheme is written in the following form below,

$$\mathbf{U}_i^n = \frac{1}{\Delta x} \int_{x_{i-1/2}}^{x_{i+1/2}} \mathbf{U}(x, t^n) dx \quad (3-25)$$

$$\mathbf{F}_{i\pm 1/2} = \mathbf{F}[\mathbf{U}(x_{i\pm 1/2}, t)] \quad (3-26)$$

This is the result when equation 3-26(Godunov flux or inter-cell numerical flux) and equation 3-25 is re-written into equation 3-24.

3.1.2. SOLUTION OF THE RIEMANN PROBLEM IN EULER EQUATIONS

Considering the following initial valued problem with discontinuous data, the Riemann problem(Toro, 1999)

$$\begin{aligned} \text{Hyperbolic system} & : \quad \mathbf{U}_t + \mathbf{F}(\mathbf{U})_x = 0, \\ \text{Initial condition} & : \quad \mathbf{U}(x, 0) = \mathbf{U}^{(0)}(x), \\ \text{Boundary condition} & : \quad \mathbf{U}(0, t) = \mathbf{U}_l(t), \quad \mathbf{U}(L, t) = \mathbf{U}_r(t), \end{aligned} \quad (3-27)$$

in a domain $x_l < x < x_r$ using the explicit conservative formula of Eq. 3.54 The Godunov flux at interface $x_{i+1/2}$ is defined by:

$$\mathbf{F}_{i+1/2} = \mathbf{F}\left(\mathbf{U}_{i+1/2}(0)\right) \quad (3-28)$$

being $\mathbf{U}_{i+1/2}(0)$ the exact similarity solution $\mathbf{U}_{i+1/2}(x/t)$ of the Riemann problem.

This(Eq. 3-28) is the exact solution of the Riemann problem applied to the Euler equations but it is not efficient due to large number of iterations. Harten Lax Van Leer Contact (HLLC) approximate Riemann solver is the practical solution of this issue and it is used in the simulations.

3.1.3. THE HLLC APPROXIMATE RIEMANN SOLVER

Harten, Lax and Van Leer (HLL)(A. Harten et al.,(1983)) introduced the HLL approximate Riemann solver which consisted in defining a new wave structure. Because they considered just two waves(Toro, 1999), the solver becomes unacceptable when solving the Euler equations because the contact wave is missing. Toro, Spruce and Spears(E. Torro et al.(1994)) introduced the HLLC approximate Riemann solver that takes the HLL and recovers the contact wave. Base on Figure 3.2, the star region is composed by two states and the structure of the solution is presented.

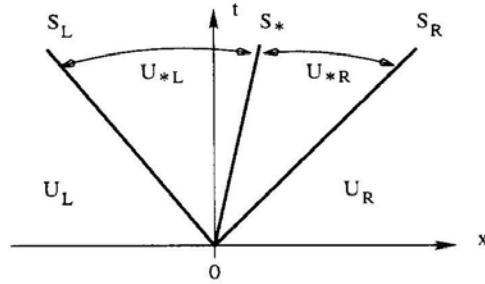


Figure 3. 2 - HLLC approximate solution structure(Toro, 1999)

Then, the HLLC solver is given by:

$$\mathbf{U}(x, t) = \begin{cases} \mathbf{U}_L & \text{if } \frac{x}{t} \leq S_L \\ \mathbf{U}_{*L} & \text{if } S_L \leq \frac{x}{t} \leq S^* \\ \mathbf{U}_{*R} & \text{if } S^* \leq \frac{x}{t} \leq S_R \\ \mathbf{U}_R & \text{if } \frac{x}{t} \geq S_R \end{cases} \quad (3-29)$$

Relating the states in the star region (Toro, 1999), the Godunov flux to be applied into the Godunov scheme can be written as:

$$\mathbf{F}_{i+\frac{1}{2}}^{hllc} = \begin{cases} \mathbf{F}_L & \text{if } \frac{x}{t} \leq S_L \\ \mathbf{F}_{*L} = \mathbf{F}_L + S_L(\mathbf{U}_{*L} - \mathbf{U}_L) & \text{if } S_L \leq \frac{x}{t} \leq S^* \\ \mathbf{F}_{*R} = \mathbf{F}_R + S_L(\mathbf{U}_{*L} - \mathbf{U}_L) & \text{if } S^* \leq \frac{x}{t} \leq S_R \\ \mathbf{F}_R & \text{if } \frac{x}{t} \geq S_R \end{cases} \quad (3-30)$$

It only remains to calculate the wave speeds which can be done directly from data

$$S_L = u_L - a_L, S_R = u_R + a_R \quad (3-31)$$

and

$$S_L = \min\{u_L - a_L, u_R + a_R\}, S_L = \max\{u_L - a_L, u_R + a_R\} \quad (3-32)$$

where u denotes the particle speed and a the sound speed. For different approaches in calculating wave speeds or more details about the Riemann problem, see (Toro, 1999).

3.1.4. RIEMANN SOLVER FOR CAPTURING SHOCKS IMPLEMENTED IN OPENFOAM

As mention in the last section the soundness and practicality of handling turbulent shocks of Approximate Riemann Solver(ARS) called Harten Lax Van Leer Contact(HLLC) introduced by Harten, Lax and Van Leer(HLL) (A. Harten et al.,(1983)) was improved by Toro, Spruce and Spears (E. Torro et

al.(1994)) using the original HLL, to recover contact wave which is missing when applied to Euler equation.

The performance and accuracy of Approximate Riemann Solver(ARS) using HLLC to capture shocks was tested rigorously in transonic density-based solver on the work of Toro(E. Toro et al.(1994)). The result achieved perfect accuracy in slowly moving discontinuities. On the other hand, highly smeared results were produced in fast moving contact discontinuities. This means that the algorithm was reliable. Base on these result, HLLC solver in *rhoPimpleDyMFoam* solver can be used with safety in transonic flows in which implemented on this work. The parameters of the simulation implemented in OpenFoam code is given in Appendix 5.

3.2. TURBULENCE MODELING

It is widely accepted that the 3D Navier-Stoke are the correct representation of turbulent flow(McDonough, 2007). Every length scales are modeled in a RANS approach such as Large Eddy Simulation(LES)(Frisch, 1995) or Direct Numerical Simulations(DNS). Landmann(Landmann, 2008) improved Kolmogorov scheme and its micro-scale theory, pointing out that one needs $O(Re^{3/4})$ to resolve all turbulent length scales per space dimension. Due to the fact that turbulence is a three dimensional phenomena, one would need $O(Re^{9/4})$ grid cells.

OpenFOAM have numbers of turbulence models available and these transonic density-based solvers can use every RANS based model, like the ones that returns turbulent viscosity u_T . Borm(O. Borm et al.,(2011)) points out there might be some conflict in rotor-stator problems when using a turbulence model that use vorticity terms because velocity jumps in the interface. The Shear stress transport(SST) model was used and doesn't have this problem: it is described below.

3.2.1. BOUNDARY LAYER SHEAR STRESS TRANSPORT (SST)

Menter(Menter, 1993) introduced the SST model. This is a two equation model that takes the approach of the $k - \omega$ (Wilcox, 1988) at the inner region of the boundary layer, using the $k - \epsilon$ in the outer region and free-stream. It modifies the definition of eddy viscosity by taking into account the transport of turbulent shear stress. This modification proved to be very important for accuracy in adverse pressure gradients(D. Johnson et al.(1985)) which is a requisite in aerodynamic turbulence models(Menter, 1994). The $k - \omega$ formulation makes it robust and a good choice for the logarithmic and viscous sub-layer regions. For the outer region and free-stream, $k - \omega$ predictions are very sensible to the free-stream specific dissipation rate ω , therefore SST switches to $k - \epsilon$ model which hasn't this behavior. In SST transport equations one can read the (1) Lagrangian derivative, (2) production term, (3) destruction term and (4) the dissipation term

$$k: \underbrace{\frac{D\rho k}{Dt}}_1 = \underbrace{\tau_{ij} \frac{\partial u_i}{\partial u_j}}_2 - \underbrace{\beta^* \rho W k}_3 + \underbrace{\frac{\partial}{\partial x_j} \left[(\mu_{Lam} + \sigma_k \mu_{Turb}) \frac{\partial k}{\partial x_j} \right]}_4 \quad (3-33)$$

$$\omega: \underbrace{\frac{D\rho\omega}{Dt}}_1 = \underbrace{\frac{\gamma}{VT} \tau_{ij} \frac{\partial u_i}{\partial u_j}}_2 - \underbrace{\beta^* \rho W^2}_3 + \underbrace{\frac{\partial}{\partial x_j} \left[(\mu_{Lam} + \sigma_k \mu_{Turb}) \frac{\partial k}{\partial x_j} \right]}_4 + 2\rho(1 - F_1)\sigma_{\omega 2} \frac{1}{\omega} \frac{\partial k}{\partial x_j} \frac{\partial \omega}{\partial x_j} \quad (3-34)$$

where constants: $C_{k\omega}$, $C_{k\epsilon}$ correspond to $k - \omega$ model, $k - \epsilon$, respectively

$$C_{k\omega} \begin{cases} \sigma_{k1} = 0.85 & \sigma_{\omega 2} = 0.5 & \beta_1 = 0.0750 \\ \beta^* = 0.09 & k = 0.41 & \gamma_1 = \frac{\beta_1}{\beta^*} - \sigma_{\omega 1} k^2 / \sqrt{\beta^*} \end{cases}$$

$$C_{k\epsilon} \begin{cases} \sigma_{k2} = 1 & \sigma_{\omega 2} = 0.856 & \beta_1 = 0.0828 \\ \beta^* = 0.09 & k = 0.41 & \gamma_2 = \frac{\beta_2}{\beta^*} - \sigma_{\omega 2} k^2 / \sqrt{\beta^*} \end{cases}$$

The constants $C_{k\omega SST}$ will result of a combination between $C_{k\omega}$ and $C_{k\epsilon}$ that reads

$$C_{k\omega SST} = F_1 C_{k\omega} + (1 - F_1) C_{k\epsilon} \quad (3-35)$$

and the model closes with the following relations

$$F_1 = \tanh \left\{ \left[\max \left(\frac{\sqrt{k}}{\beta^* \omega d}, \frac{500\nu}{d^2 \omega} \right), \frac{4\sigma_{\omega 2} k}{CD_{kw} d^2} \right] \right\}^4, \quad (3-36)$$

$$F_2 = \tanh \left[\left[\max \left(\frac{2\sqrt{k}}{\beta^* \omega d}, \frac{500\nu}{d^2 \omega} \right) \right]^2 \right], \quad (3-37)$$

$$CD_{kw} = \max \left(2\rho\sigma_{\omega 2} \frac{1}{\omega} \frac{\partial k}{\partial x_i} \frac{\partial \omega}{\partial x_i}, 10^{-10} \right), \quad (3-38)$$

$$\nu_{Turb} = \frac{a1k}{\max(a1\omega, \Omega F_2)}, \quad (3-39)$$

being ν_{Turb} the kinematic turbulent viscosity. The derivation of Eq. 3-33 and 3-34 comes from a transformation of the $k - \epsilon$ model to a $k - \omega$ formulation with the following relation

$$\omega = \frac{\epsilon}{\beta^* k} \quad (3-40)$$

and then a combination of both $k - \epsilon$ and $k - \omega$ models with a function F_1 that acts like a switch in the inner and outer regions of the boundary layer. Full details are given in the works of Davidson (Davidson, 2006). Other approaches can be found from (Menter, 1992) & (P. Spalart et al., (2007)).

3.3. SPATIAL DISCRETIZATION

The neighboring cells in every grid are computed per length scales to solve the field properties by discretization. The method of discretization implemented in this transonic density-based libraries is known as the method of lines(Morton et al.,(1967)) which allows the selection of numerical methods with different accuracy for time and space.

The interpolation formulae of the inviscid terms is done with Van Leer's MUSCL(Leer, 1977) which defines them as second-order accurate in space. Taking the Godunov integral average for a specific quantity φ_i^n in cell $I_i = \left[x_i - \frac{1}{2}, x_i + \frac{1}{2} \right]$, the piece-wise linear reconstruction of MUSCL is given by:

$$\varphi_i^n(x) = \varphi_i^n + \frac{(x - x_i)}{\Delta x} \Delta\varphi, \quad x \in [0, \Delta x] \quad (3-41)$$

where $\frac{\Delta\varphi}{\Delta x}$ is a chosen slope of $\varphi_i(x)$ in cell I_i . Figure 3.3 shows the average and its linear reconstruction.

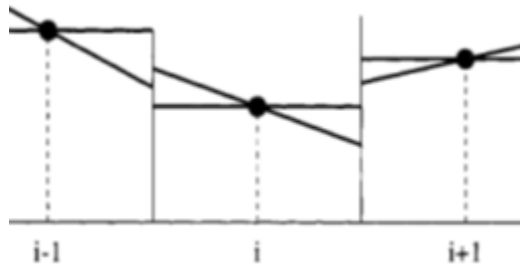


Figure 3. 3 - Cells discretization method (Toro, 1999)

It is also of great importance the extreme points of $\varphi_i^n(x)$, they will define the right $\varphi_{i+1/2}$ and left $\varphi_{i-1/2}$ states introduced in Section 3.1.2 and are given by:

$$\varphi_{i-1/2} = \varphi_i^n - \frac{1}{2}\Delta\varphi, \quad \varphi_{i+1/2} = \varphi_i^n + \frac{1}{2}\Delta\varphi. \quad (3-42)$$

The slope is read:
$$\Delta\varphi = \frac{1}{2}(1 + \omega)\Delta\varphi_{i-1/2} + \frac{1}{2}(1 - \omega)\Delta\varphi_{i+1/2} \quad (3-43)$$

with
$$\Delta\varphi_{i-1/2} \equiv \varphi_i^n - \varphi_{i-1}^n, \quad \Delta\varphi_{i+1/2} \equiv \varphi_{i+1}^n - \varphi_i^n \quad (3-44)$$

and ω is a free parameter in the real interval $[-1, 1]$. Setting $\omega = 0$ leads to a secondorder accurate upwind-biased linear interpolation. The MUSCL scheme needs to add more features when in presence of strong gradients. They are called *limiter functions* or *limiters* and are build to reduce the solution wiggles near discontinuities.

In all simulations the Venkatakrishnan(Venkatakrishnan, 1995) limiter is used. It is second order accurate $\omega = 0$ and reduces the reconstructed gradient by the following factor,

$$\psi = \begin{cases} \frac{1}{\Delta_2} \left[\frac{(\Delta_{1,max}^2 + \epsilon^2) \Delta_2 + 2\Delta_2^2 \Delta_{1,max}}{\Delta_{1,max}^2 + 2\Delta_2^2 + \Delta_{1,max} \Delta_2 + \epsilon^2} \right] & \text{if } \Delta_2 > 0 \\ \frac{1}{\Delta_2} \left[\frac{(\Delta_{1,min}^2 + \epsilon^2) \Delta_2 + 2\Delta_2^2 \Delta_{1,min}}{\Delta_{1,min}^2 + 2\Delta_2^2 + \Delta_{1,min} \Delta_2 + \epsilon^2} \right] & \text{if } \Delta_2 < 0 \\ 1 & \text{if } \Delta_2 = 0 \end{cases} \quad (3-45)$$

where,

$$\Delta_{1,max} = \phi_{max} - \phi_i \Delta_{1,min} = \phi_{min} - \phi_i \quad (3-46)$$

In Eq. 3-46, ϕ_{max} and ϕ_{min} are the maximum and minimum values of all neighbor nodes and the owner itself. The parameter ϵ^2 is meant to control the amount of limiting and it was found that it should be proportional to a local scale length, i.e.

$$\epsilon^2 = (K\Delta h)^3 \quad (3-47)$$

It was found (Venkatakrishnan, 1995) that setting $K = 5$ provided the best convergence properties with the best shock resolution thus this value is used in all simulations. The viscous terms are built with central difference discretization which is second order. Therefore, this solver is second order in space although lower order can be used.

3.4. TIME DISCRETIZATION

3.4.1. STEADY SOLVER

To attain convergence steady state condition must be reached on the solution. In every control volume, Eq. 3-1 can be written in a semi discrete form

$$\frac{\partial vU}{\partial t} = -\mathbf{R}(\mathbf{U}) \quad (3-48)$$

with v for volume and the residual vector \mathbf{R} being the full spatial discretization and a non-linear function of the conservative state vector. Integrating Eq. 3-48 with time, will result a steady state $\mathbf{R}(\mathbf{U}) = 0$ or an unsteady solution and both solutions are available in the density-based libraries.

It is important to note that time accuracy in steady cases is irrelevant. The accuracy of the solution only depends on spatial discretization making the advantage of method of lines clearer. From the other side, in unsteady flows, the aim is to get the highest temporal accuracy possible. Runge-Kutta (A. Jameson et al., (1981)) time stepping is available and will be used in the simulations. It is given by:

$$\begin{aligned} \mathbf{U}^0 &= \mathbf{U}^n \\ \mathbf{U}^1 &= \mathbf{U}^0 - \alpha_1 \frac{\Delta t}{\Delta x} \mathbf{R}(\mathbf{U}^0) \\ \mathbf{U}^2 &= \mathbf{U}^0 - \alpha_2 \frac{\Delta t}{\Delta x} \mathbf{R}(\mathbf{U}^1) \\ \mathbf{U}^3 &= \mathbf{U}^0 - \alpha_3 \frac{\Delta t}{\Delta x} \mathbf{R}(\mathbf{U}^2) \end{aligned} \quad (3-49)$$

$$\mathbf{U}^4 = \mathbf{U}^0 - \alpha_4 \frac{\Delta t}{\Delta x} \mathbf{R}(\mathbf{U}^3)$$

$$\mathbf{U}^{n+1} = \mathbf{U}^4$$

with the following coefficients:

$$\begin{aligned} \alpha_1 &= 0.11 \\ \alpha_2 &= 0.2766 \\ \alpha_3 &= 0.5 \\ \alpha_4 &= 1.0 \end{aligned} \tag{3-50}$$

By reducing the residual of equation 3-48 towards machine zero, a steady state will be reached.

3.4.2. UNSTEADY SOLVER

On the onset of stall, the approach is to calculate the unsteady behavior. This approach from the solver is called dual time-stepping(DTS) and it is a common practice. Explicit Runge-Kutta and convergence acceleration techniques are not time accurate, therefore, Jameson(Jameson, 1991) introduces a pseudo-time τ solver that will re-formulate Eq. 3-48 in the following form,

$$\frac{\partial v\mathbf{U}}{\partial \tau_t} = \frac{\partial v\mathbf{U}}{\partial t} + \mathbf{R}(\mathbf{U}) = \mathbf{R}^*(\mathbf{U}) \tag{3-51}$$

$\mathbf{R}^*(\mathbf{U})$ is a new residual and the physical time derivative $\frac{\partial}{\partial t}$ is approximated by a second order accurate three-point backward difference(Blazek, 2001). Hence,

$$\frac{\partial v\mathbf{U}}{\partial \tau_t} = \frac{3v^{n+1}\mathbf{U}^{n+1} - 4v^n\mathbf{U}^n + v^{n-1}\mathbf{U}^{n-1}}{2\Delta t} + \mathbf{R}(\mathbf{U}^{n+1}) = \mathbf{R}^*(\mathbf{U}^{n+1}), \tag{3-52}$$

with the steady state techniques mentioned above being used to reduce the residual $\mathbf{R}^*(\mathbf{U})$. When the pseudo-time solver converges $\frac{\partial \Omega \mathbf{U}}{\partial \tau_t} \approx 0$, the physical time step advances.

3.5. THE CONVERGENCE TECHNIQUES

There are numbers of convergence technique namely: the Local Time Stepping (LTS), Implicit residual smoothing (IRS), and Multigrid. The first will be discussed on this section, the second is mention in Section 3.4 introduced by Jameson(Jameson, 1983), and the last technique, one can refer to a number of literatures such as those from (Blazek, 2001), (A. Andrea et al.,(1993)) and (R.Swanson et al., (1991)).

In these section we will describe the only accelerating convergence technique implemented in the density-based libraries: the Local Time Stepping (LTS).

The LTS consists in using the maximum allowable time step taking the dissipative and convective contributions. Hence, according to Blazek(Blazek, 2001) they can be given by:

$$\Delta t_d = \max\left(\frac{4}{3\rho}, \frac{\gamma}{\rho}\right) \left(\frac{\mu_{Lam}}{Pr_{Lam}} + \frac{\mu_{Turb}}{Pr_{Turb}}\right) \left(\frac{\Delta x}{\nu}\right)^2, \quad \Delta t_c = (|U| + c)\Delta x \quad (3-53)$$

and Andrea et al. (A. Andrea et al., (1993)) proposes the following final time step,

$$\Delta t = C_{cfl} \frac{(\Delta t_d \Delta t_c)}{(\Delta t_d + \Delta t_c)} \quad (3-54)$$

Applying all of these concepts to CFD and more precisely to residuals, one can make the following statement. Every cell residuals can be seen as a sequence and the whole mesh is the set of sequences in which it is true that at each step they have a value. If a steady state is to be reached, it means steadiness is attained and will surely converged.

CHAPTER 4: THE TEST CASE AND SETTINGS AT OPENFOAM SOLVER

In this chapter the description of the axial compressor being studied is introduced. The geometry configuration of the compressor will also be presented. The numerical scheme and boundary procedure discuss in the previous chapter will be implemented in the solver. The general set up of the test case will be implemented in the Open Foam solver. The necessary work to prepare the case in CFD *OpenFoam* tool and to extract results in *Paraview* will also be discuss. The actual procedures and the real work of running fluid flow problem in a test case using CFD is the main take away learning by the author. This chapter is the main highlight of the work.

4.1. THE TEST CASE - NASA ROTOR 67

The test case is the NASA(National Aeronautics and Space Administration) Rotor 67 shown in Figure 4.1 below, labeled L.P. COMPRESSOR call out in the diagram. This is part of low pressure(LP) turbo fan's compressor set of the jet engine responsible for generating thrust in common commercial airplanes.

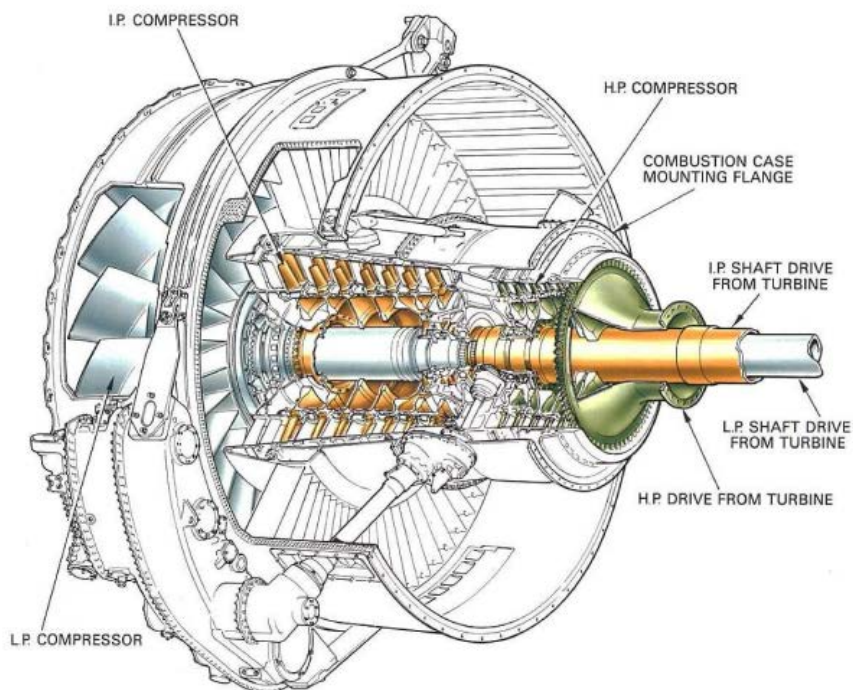


Figure 4. 1 - Rolls Royce Jet Engine. Courtesy: (Royce)

The geometrical inputs of NASA Rotor 67 was reported in Table 1 on NASA Technical Paper 2879(A.J. Strazisar et. al.,(1989)). It has 14 stacking blade profiles given, each has 35 specified coordinates points in radial, axial, and angular coordinates that comprised the whole rotor geometry. The

input points were used to create the three dimensional model using CAD tool(Autodesk Inventor 2015). The resulting 3D CAD model of the rotor is shown Figure 4.2 where blades, hub and shroud are captured accurately. This are used for specifying the flow domain and boundary condition in setting up the case in CFD. The CAD model has also tip-gap clearance between shroud and tip of the blade of about 0.1 cm.

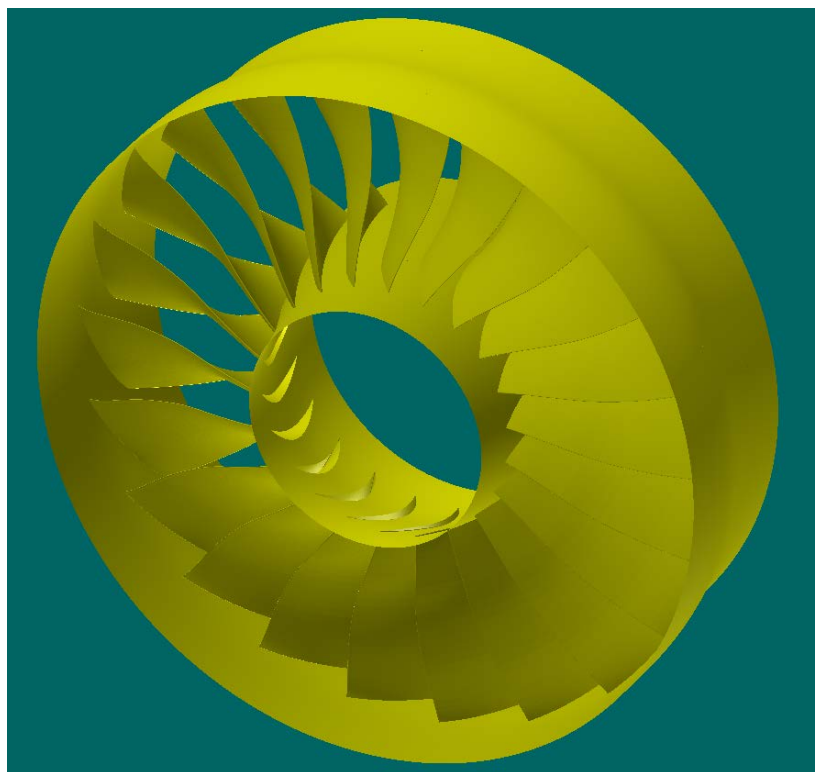


Figure 4. 2 - NASA Rotor 67

4.1.1. TEST PARAMETER DESCRIPTION OF THE ROTOR

Aside on simulating compressor stall in CFD, the work also aim by solving three dimensional flow of the transonic high speed axial fan, NASA rotor 67, and compare the compressor performance map to the experimental result.

This low aspect($\sigma=1.56$) ratio rotor is the first stage rotor of a two stage transonic fan designed and tested with laser anemometer measurements at the NASA Glenn Research Center. The design pressure ratio is 1.63, at a mass flow rate of 33.25 kg/sec. The rotor has 22 blades with tip radii of 25.7 cm and 24.25 cm at the leading and trailing edge, respectively. The hub/tip radius ratio is 0.375 at the leading edge and 0.478 at the trailing edge. The design rotational speed is 16 043 rpm, and the tip leading edge speed is 429 m/sec with a tip relative Mach number 1.38. To determine the rotor mass flow rate, a calibrated aerodynamic survey probes(orifice) shown in Figure 4.3 was used. A detailed description of blade and flow-path geometry, as well as measured data on total pressure, temperature, static pressure and flow angle data, can be found in the work of A. J. Strazisar et al.(A.J. Strazisar et. al.,(1989)). Figure 4.4

shows the locations where velocities were measured for this compressor labeled aero station 1 and aero station 2. The hub consists of two stationary and one rotational segments. The rotor hub is in the region of $-3.533 \text{ cm} < x < 7.106 \text{ cm}$ and rotational wall conditions were applied to this region.

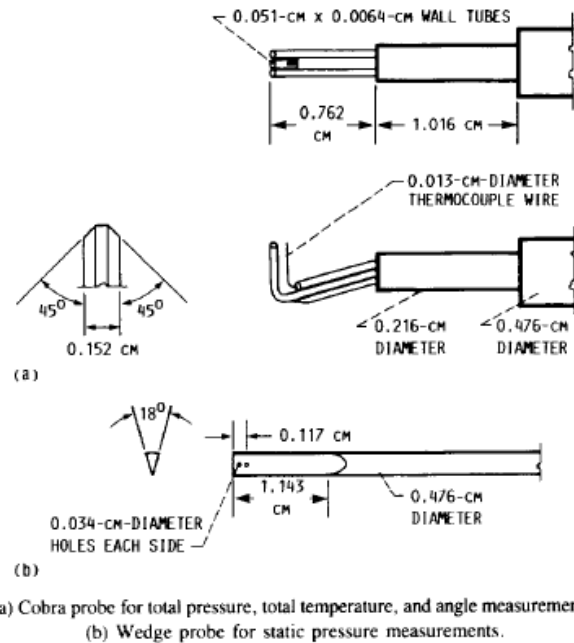


Figure 4.3 - Aerodynamic survey probes(A.J. Strazisar et. al.,(1989))

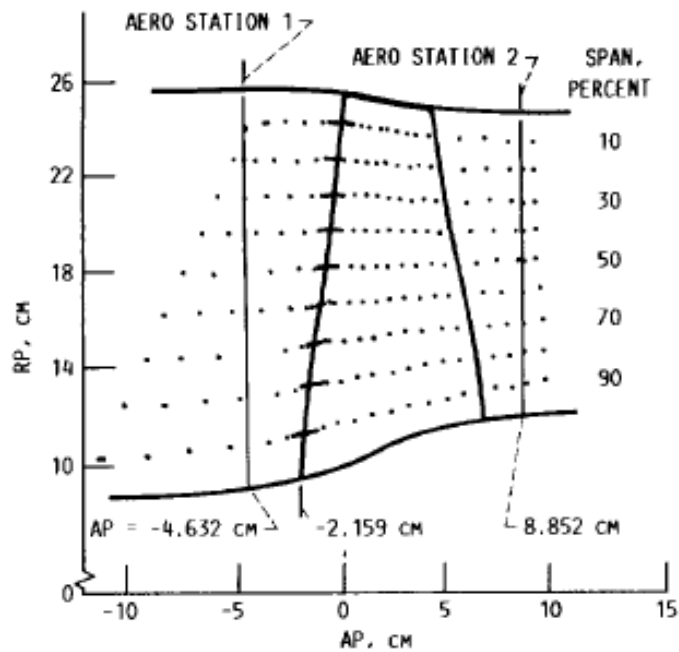


Figure 4.4 - Laser Anemometer and aerodynamic survey locations(A.J. Strazisar et. al.,(1989))

4.2. OPENFOAM OVERVIEW

The three dimensional flow and stall simulation will be done using Computational Fluid Dynamics software with the appropriate solver that fits the case. The CFD software used on this work is called *Open Source Field Operation and Manipulation (OpenFOAM)*. It is an open-source software, for computer simulations of fluid dynamics and is freely available to anyone, distributed under General Public License-GPL. Due to the open-source nature of *OpenFOAM*, it is easy to add new features. Since the source code can be access, the user can modify and implement the code to fit special requirement with the advantage of understanding how CFD methods work. This is why *OpenFOAM* is also a great tool, as L. Pirkl noted "When used properly, it can beat any commercial code available in terms of costs, speed or accuracy.(Pirkl, 2016)

4.2.1. OPENFOAM WORK FLOW AND CASE STRUCTURE

OpenFOAM was written to be a library of functions for easy creation of applications for solving continuum mechanics problems. It all provides access to essential applications required for continuum mechanics modeling, pre-processing, solving and post-processing. Figure 4.5 shows the workflow in *OpenFOAM*.

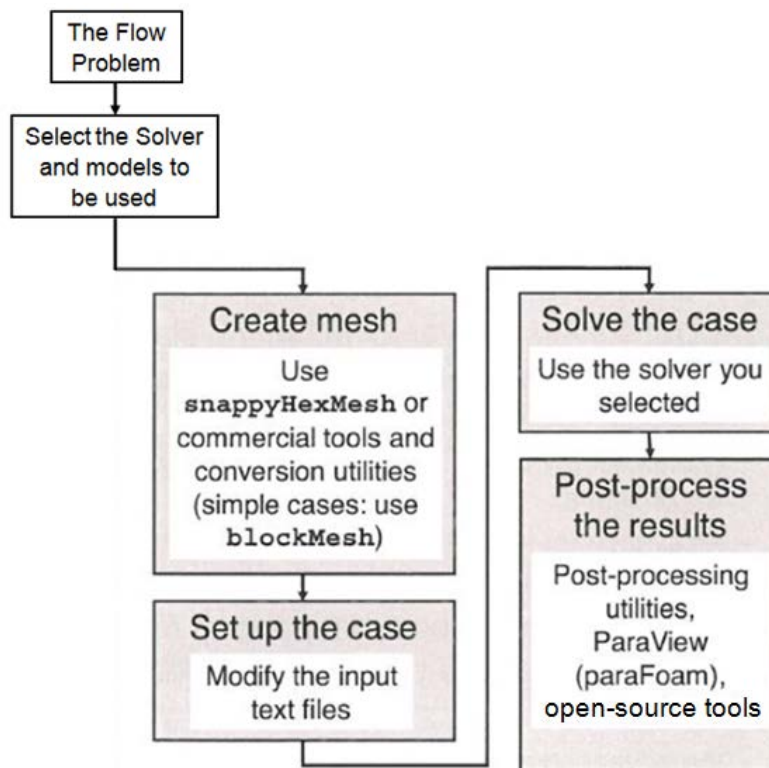


Figure 4. 5 - OpenFOAM Workflow

Libraries are pieces of code in C++ object oriented programming language that can be used to build solvers or utilities. These libraries are organized based on the type of flow problems and assigned folder names as an identity label of the flow it is going to solved. Therefore, the user can select a folder that fits, duplicate the folder and set up the case. On the same manner, *OpenFOAM* have variety of solvers that are hard coded and usually designed for a specific type of problem like steady state or transient flows, incompressible or compressible flows and other complex physics also have dedicated solvers, which are ready. Thus user can select the correct solver as well within *OpenFOAM*. Utilities are executables that performs small tasks usually for pre-processing and post-processing the solution data. One worthy to mention is the unstructured meshing utility called *snappyHexmesh* that is used on this work and will be covered in section 4.4.

Preparing and setting up the case is where the real engineering application of the flow problems is carried out. Figure 4.6 is sample of a case structure that must be set up correctly to solve a flow problem successfully. These means modifying codes, adding features, filling up parameters etc. on the library files that embodies the whole physics of the flow problem. The solver is the main code that collects the entire codes from libraries to run and execute the solution. The results can be post process by a post processing tool, *Paraview*, which is compatible with *OpenFOAM*.

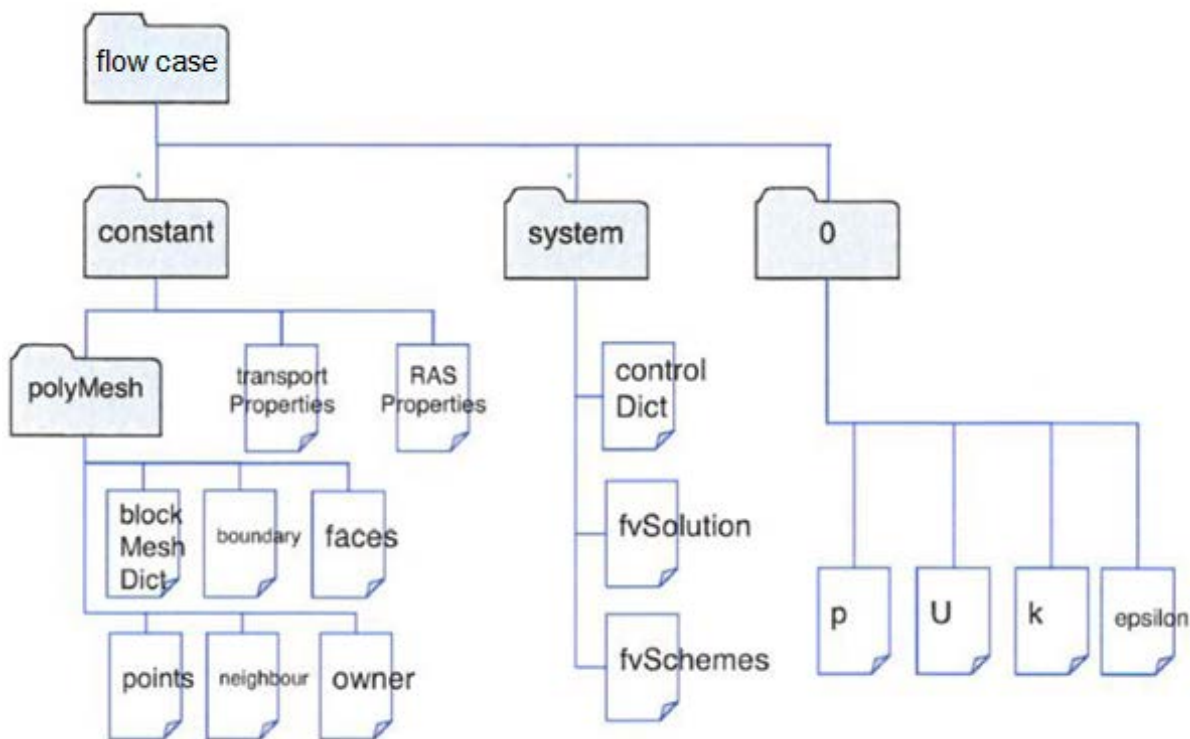


Figure 4. 6 - A sample OpenFOAM case structure

4.3. DATA

4.3.1. EXPERIMENTAL DATA EXTRACTION

Experimental data is available at peak efficiency and near stall given on the work of A.J. Strazisar et. al.(A.J. Strazisar et. al.,(1989)). The tangential and axial velocity data were collected using laser anemometer(LA). Its technique is as follows, they used window numbering refer to as WNBEG along pitch-wise to cover 360 degrees of the rotor. 1100 windows in a single passage measured 50 positions along θ . Results were often presented in blade to blade(B2B) with coordinates in radius-theta-meridional(r - θ -M). They took samples, 30 in axial position with nine surface revolutions which gives 50x30x9 measuring positions in a rotor passage. Figure 4.7 illustrates how the positions of the measurements were defined.

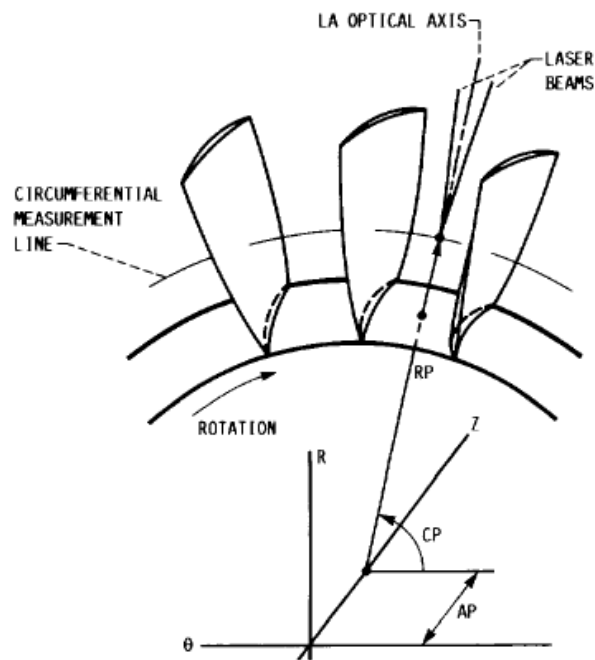


Figure 4. 7- Data Coordinate Measurement(A.J. Strazisar et. al.,(1989)) , RP-radial position, AP-axial position, CP-circumferential position

There are two plots that should be understood from the experiment to get good interpretation: the stream-wise and pitch-wise. Stream-wise will follow a streamline and a pitch-wise that follow along pitch, each has always in constant percent(%) span position. A stream-wise plot will be defined by constant pitch percentage and pitch wise plot will be defined by constant chord percentage position as shown in Figure 4.8. The starting window number(WNBEG) for laser anemometer survey is available for all plots. The streamline define the pitch also, as 50 windows per passage define a range for pitch. How the windows are numbered is shown in Figure 4.9.

Radial measurement were taken up-stream and downstream of the rotor for the velocity blade surveys, including p_0 and T_0 that were used to calculate the overall rotor aerodynamic performance. National Advisory Committee for Aeronautics(NACA) corrected all data into standard day condition at sea level: $p_0 = 101325\text{Pa}$ and $T_0 = 288.15\text{K}$. For more details refer NASA Technical Paper 2879(A.J. Strazisar et. al.,(1989)).

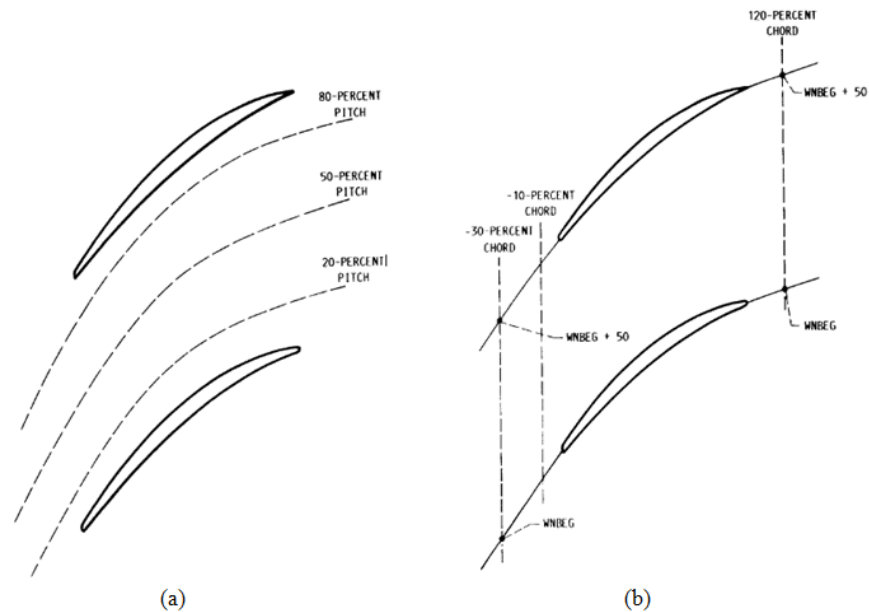


Figure 4. 8 - (a) Streamlines (b) Constant chord percentage line(A.J. Strazisar et. al.,(1989))

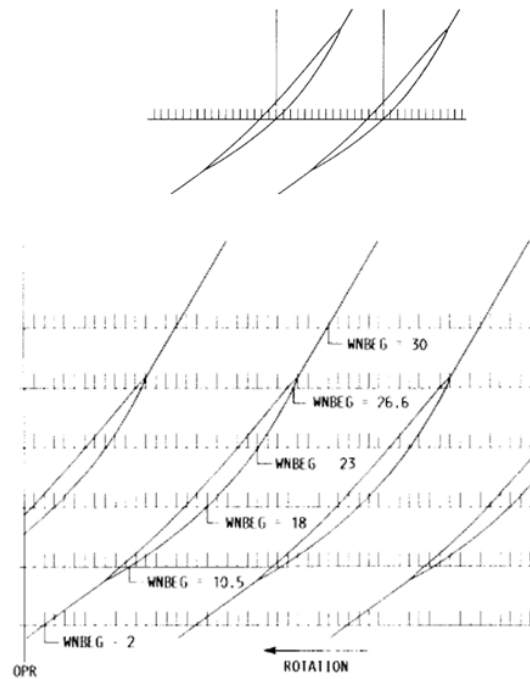


Figure 4. 9-Window numbering(A.J. Strazisar et. al.,(1989)) with emphasis each blade having same window point(top)

4.3.2. NUMERICAL DATA EXTRACTION(POST-PROCESSING)

How experimental data is extracted should have similar resemblance on how numerical result should also be gathered in order to get better results comparison. With open source software, *Paraview*, numerical data extraction from a rotor is not straightforward. This is due to the way how experimental data is taken, a Cartesian referential is not appropriate to understand rotating geometries and solutions, while the visualizer, *Paraview*, does not have the necessary tools in the *Graphic User Interface(GUI)* to perform blade to blade cuts. To do the task, there is a python code developed by Borm(Borm, 2013), that works with *Paraview*.

With regards on extracting streamlines along span, a utility called Plot on Interception Curves from *Paraview* is used. It is being done by making a sphere with enough radius intercepting at span region to create the cut to approximate a streamline with constant pitch percentage. See Figure 4.10 illustrating the cut and purported data points, all plots of other percent cuts was done similarly.

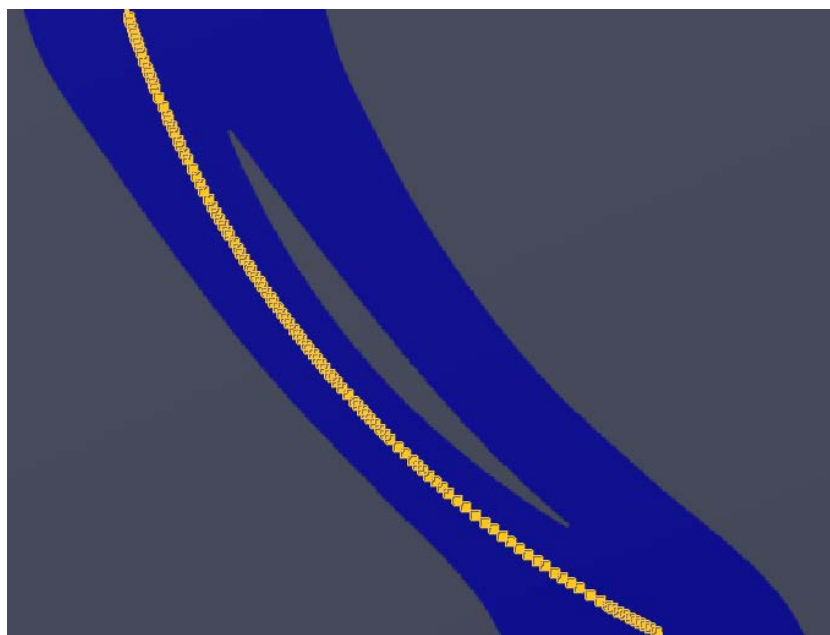


Figure 4. 10 - Data extraction in *Paraview*

It is also important to take notice that the simulation is using only one passage and the domain used in simulation is of C-type(not blade-to-blade). The streamline percentage of the experimental data(Figure 4.8(a)) has its equivalent authors' logical interpretation to be of similar numerically extracted data. Base on the concept of repeating stages(Mohsen Assadi, 2017), 80-percent pitch in the suction(Figure 4.8(a)) side wall, stream-wise in experimental data is equivalent to 20-percent pitch in the pressure side of the numerical simulation data. This means, cut beyond 50 percent of the suction side in the experiment has equivalent result as the pressure side of the numerical simulation taking the percentage reference of the pressure side wall to the right, details is shown in Figure 4.11.

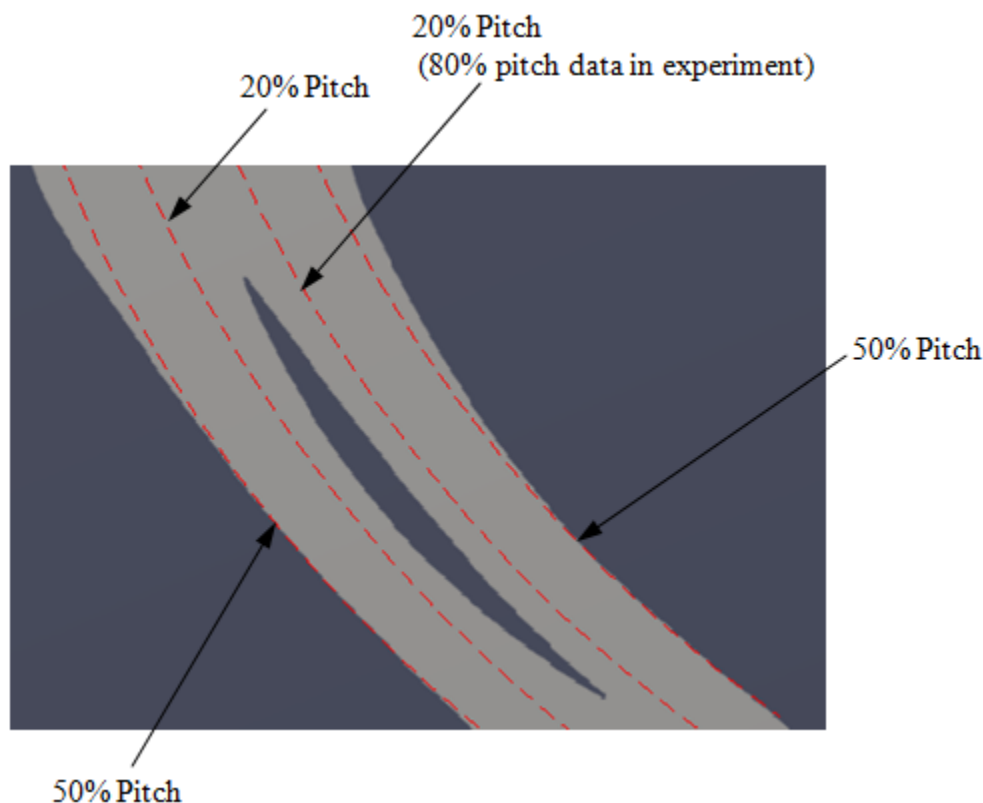


Figure 4. 11 - Streamwise pitch percentage of the flow passage

The extraction of pitch-wise lines can be straight forward, taking into account that chord percentage (the axial chord in pitch-wise), coordinates of leading edge (LE) and trailing edge (TE) were taken and gathering the data follows naturally. Plotting the pitch-wise data can be difficult due to radius-theta-meridional ($r-\theta-M$) plane and window numbering (WNBEG) on experimental data which should correlate the numerical results. Since only one passage is simulated, it is necessary to identify where all the relevant WNBEG windows is in one numerical passage. Recalling that the domain has 22 number of blades, passage pitch range is associated with 16.3636 degrees ($\frac{360}{22}$) at constant chord percentage to cover the overall domain and then get the two known window points.

OpenFOAM has a *functionObject* utility called *patchAverage* that acts like the radial surveys upstream and downstream of the rotor by area averaging and mass averaging of the variables on assessing overall aerodynamic performance. Area averaging is applied in this case because density varies in the simulation due to transonic nature flow of the fluid. *patchMassFlow* function object is also used to know if there is conservation of mass between the inlet and outlet of the rotor.

Finally, we often want more quantitative data from the case flow results. Discuss above, values can be taken directly from *Paraview* through plot over a line or curve with the filter *Plot Over Line*, this was utilized in some plots. While this is a bit convenient, we want to extract the values to a text file using

functions objects. This makes it easier to compare against data coming from other sources and it suited for this work when we want to compare the results for the velocity and pressure and create plots.

This is done by creating a file in the system folder with user appropriate filename on the type of parameter extracted. This contains the start and end coordinate extraction points with a specified fields, like velocity for example. Then the following line(see Figure 4.12) will be added at the end of the *controlDict* dictionary file. This is the sample on the plot of the residuals shown in the introductory part of Chapter 5, which plots the residuals for the pressure and velocity. After the simulation, the file is written in the *postProcessing* folder in *.dat* file type and data's can be extracted using plotting tools, in this work, using Microsoft excel. Similar code lines were applied to other parameter fields that are going to be extracted to gather necessary data's for the entire work.

```

functions
{
    residuals
    {
        #includeEtc
        "caseDicts/postProcessing/numerical/residuals.cfg"
        fields (p u);
    }
}

```

Figure 4. 12 - Sample of a *function object* code for Plotting and data extraction(Residuals plots sample)

4.4. MESHING

4.4.1. THE ROTOR GEOMETRY

The input data for rotor and the casing geometries from NASA Technical Paper 2879(A.J. Strazisar et. al.,(1989)) was converted into 3D model using Autodesk Inventor, a commercial design software. This creates blade surfaces and camber coordinates with given angles BETA in the meridional direction as introduced from the Technical paper. The blade surface and the camber line were defined with 35 points in the radial, theta-meridional plane and thickness was set symmetric to camber line. All 14 blade sections were linearly stacked from the hub. The created 3D rotor geometry from the input data is shown in Figure 4.13. One can say that the resulting 3D CAD rotor is a complex geometry due to the twisting of the blade and an angled span. By inspection, this conforms by the given reference, shown in Figure 4.14 in which stacking is not linear.



Isometric view(Partially looking from bottom)



Top view

Figure 4. 13 - Rotor Blade - CAD modeled

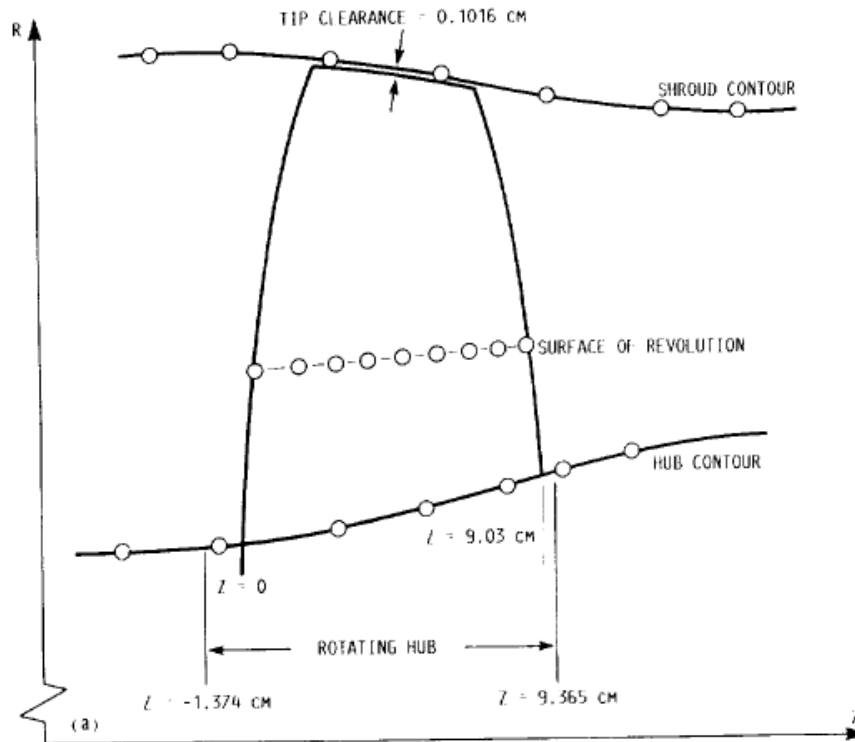


Figure 4. 14 - Meridional Plane(A.J. Strazisar et. al.,(1989)

4.4.2. CREATING THE TRI-SURFACE PATCHES

The modeled rotor geometry needs triangulation or tri-surface meshing as a requirement for the fluid computational domain. An open-source software called Salome("https://www.salome-platform.org/") have one of its varied capabilities which is to mesh CAD models. The modeled 3D geometry is then imported to Salome for surface meshing or triangulation. Figure 4.15 shows the resulting mesh. The rotor geometry needs to have a complete boundary patches that comprises the overall flow domain that should be triangulated in the same manner. Figure 4.16 illustrates the rotor geometry with the additional patch boundaries which are the two side face patches(on the figure only one side is shown) and the shroud. One can notice that it is empty inside which means the meshed patches will serves as the geometry tri-surface boundaries in the process of creating the computational domain. The blade edges, tip and hub patches have fine meshes than the rest of the surfaces as shown(figure 4.15) to captures corner and edge transition accurately.

After rotor and additional geometries are meshed, it is exported to Stereolithography(STL) format with mesh retained giving each patch geometry a filename. These stl files are place at /constant/tri-surface folder and read by OpenFoam during unstructured meshing of the computational domain. The triangulated surface filenames are: Rotor_BLADE.stl, Rotor_HUB.stl, Rotor_INLET.stl, Rotor_OUTLET.stl,

Rotor_SHROUD.stl, Rotor_SIDEFACE1.stl and Rotor_SIDEFACE2.stl. STL geometries group into one makes up the flow patch domain as can be seen in Figure 4.16.(one side face stl geometry is hidden)

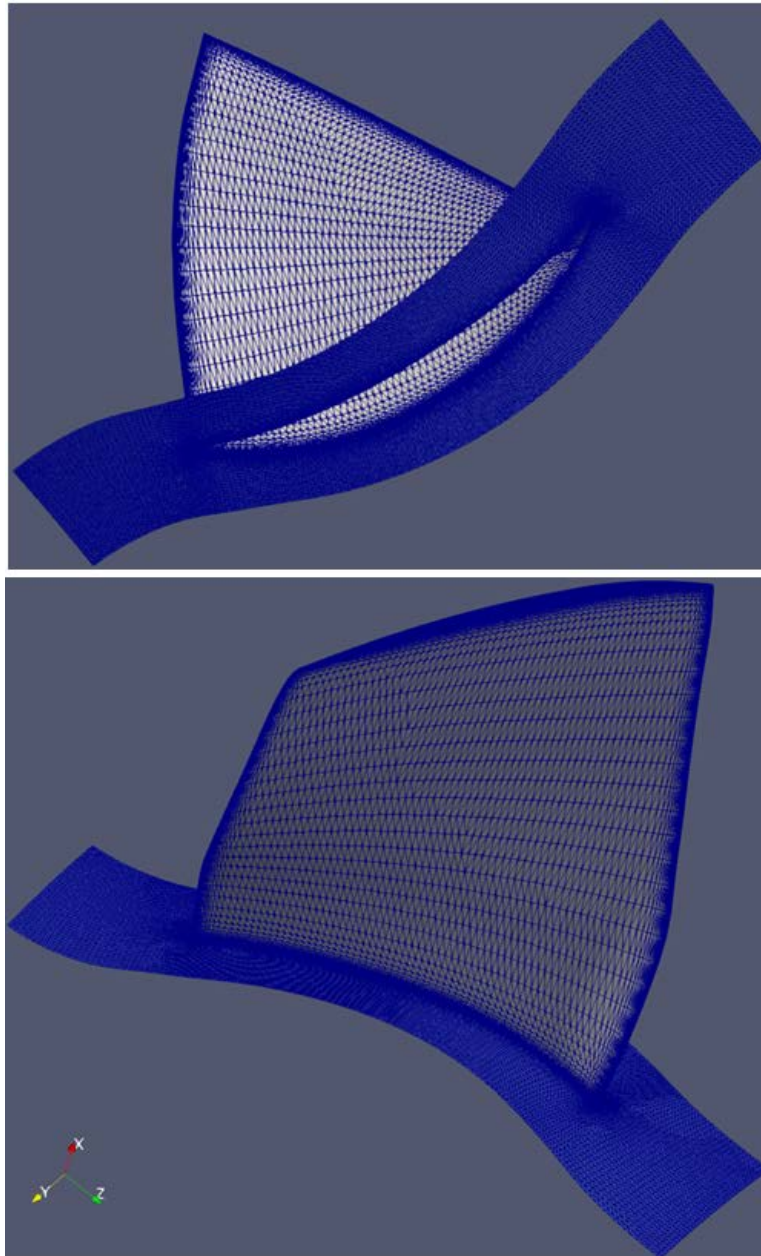


Figure 4. 15 - 3D mesh of the rotor geometry in Salome

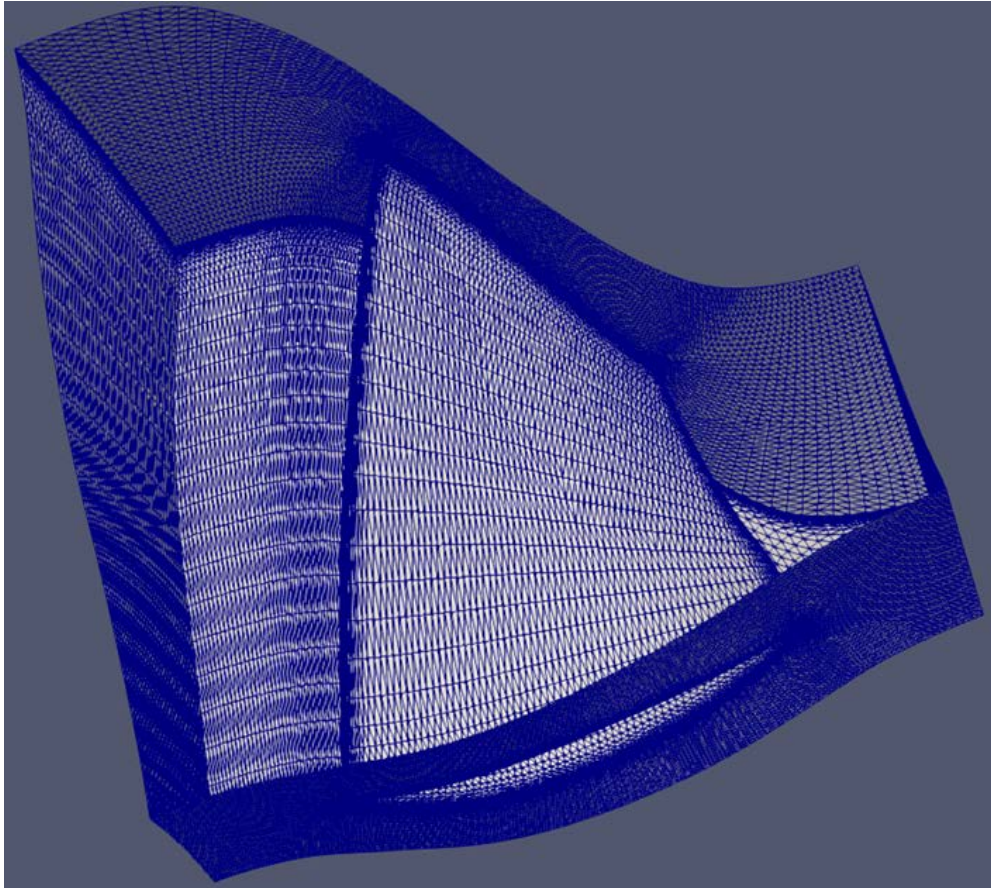


Figure 4. 16 - The tri-surface .stl geometries as one flow domain(one face is hidden to see inside)

4.4.3. MESHING THE COMPUTATIONAL DOMAIN

The success and accuracy of the solutions from any *OpenFOAM* simulation are subject to mesh quality of the computational domain. The computational domain is created using *snappyHexMesh* utility which generates 3-dimensional hexahedra(hex) meshes automatically from the triangulated surface geometries(tri-surface) created in section 4.4.2. The generated mesh will approximately conform to the input tri-surface boundaries by iterative refining processes. Edges of stl tri-surface geometries are extracted using *surfaceFeatureExtract* sub-dictionary in *snappyHexMesh*. The silhouette of the blade was extracted using open source editor called *Blender*("https://www.blender.org/") to capture LE and TE edges and exported as .OBJ file so it will be readable in *OpenFoam*. These edges are used as feature refinement to achieved quality meshing at edges and corners. The required background mesh was created in *Salome* and exported as *unv* file and converted to *OpenFoam* mesh through *ideasUnvToFoam* command. There are two main and one optional process in *snappyHexMesh*: *castellation*, *snapping* and *adding layers* respectively.

SnappyHexMesh needs background mesh which defines the extent of the computational domain as the first step. The tri-surface .stl geometries inside the background mesh is shown in Figure 4.17. Within the

vicinity of the tri-surface boundaries and edges, mesh level refinement of background mesh cells were refine further.

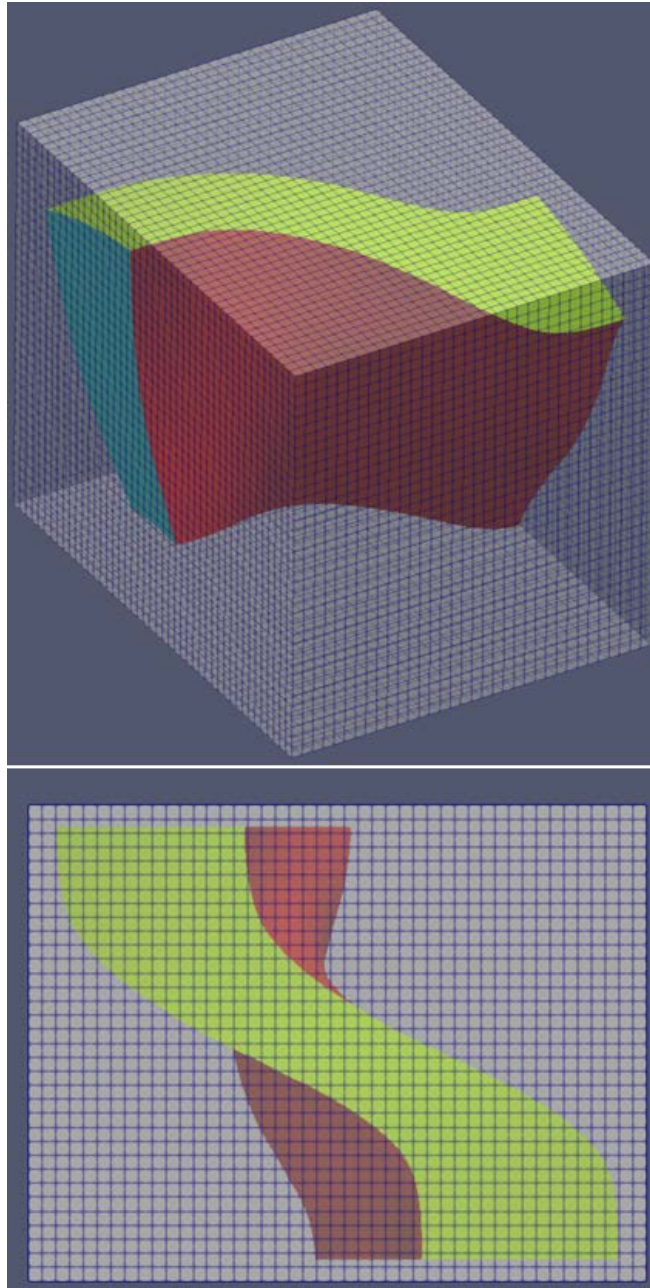


Figure 4. 17 - Background mesh with tri-surface .stl geometries inside(iso and top view)

Local mesh refinements is done also on the surface boundaries and edges that intersects with the background mesh. Intersects between tri-surface boundaries and background mesh is done according to the *castellatedMeshControls* sub-dictionary using *eMesh* file from *surfaceFeatureExtract* and tri-surface boundaries. Then the system recognized the computational domain region and splits the cells that intercept to the background mesh. After splitting is completed a user keep point specified in *locationInMesh* sub

dictionary removed unused cells creating the castellated computational domain mesh. Figure 4.18 shows the castellated mesh of the fluid computational domain.

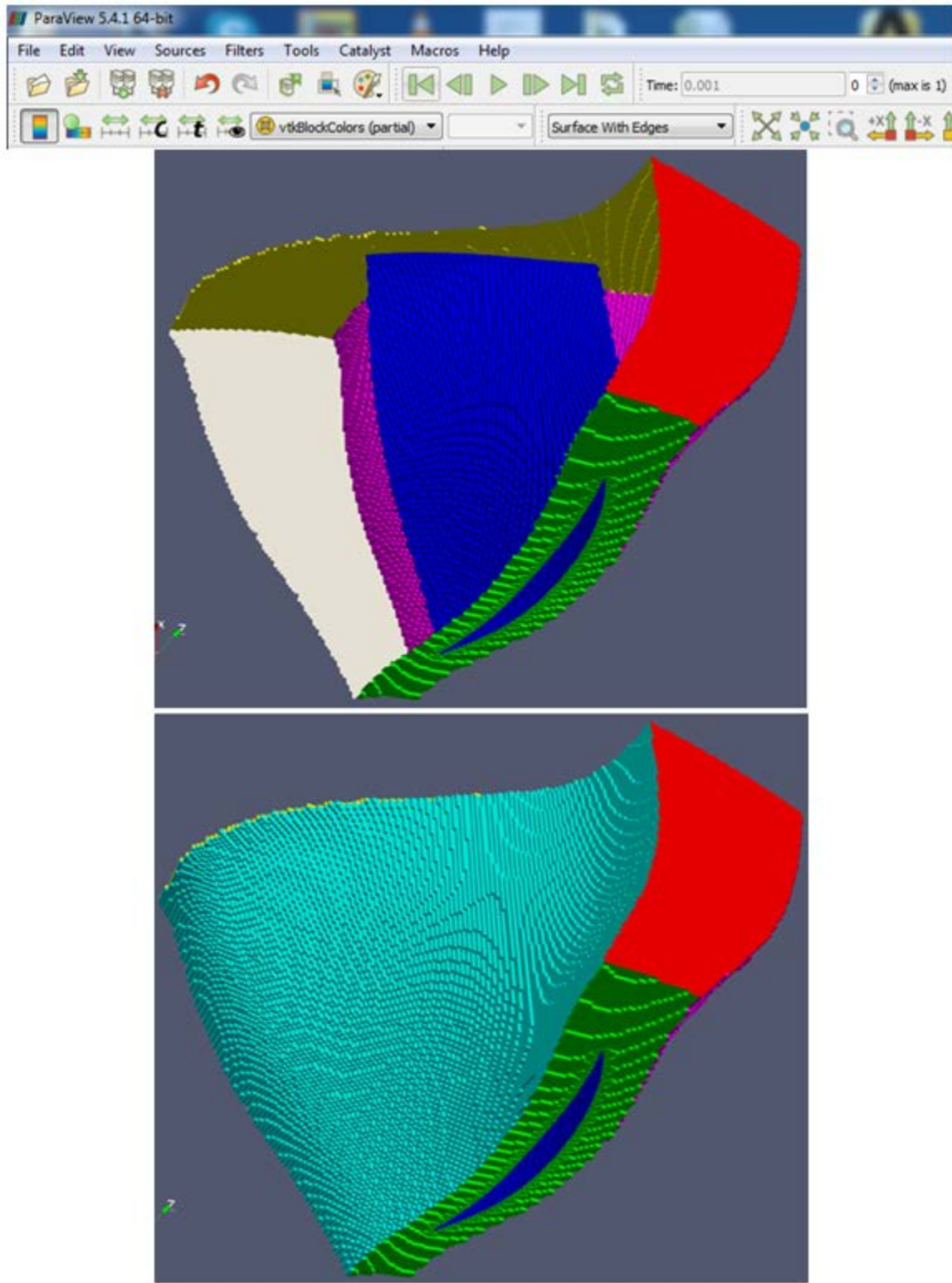


Figure 4. 18 - Castellated Mesh of the Fluid Computational Domain(Bottom) and tri-surface boundaries(Top)

To preserve the geometry features of the tri-surface boundaries after castellated process, the next phase is surface snapping. This involves moving the cell vertex points onto the surface geometry to remove the jagged castellated surface from the mesh. With the latest displaced boundary vertices, internal mesh of the flow domain is then solved. The cells closest to the interface are snapped to the actual surface then faces are merge and smoothen. This is controlled by the *snapControls* sub-dictionary settings in the *snappyHexMeshDict* dictionary. Figure 4.19 shows the result of surface snapping mesh process.

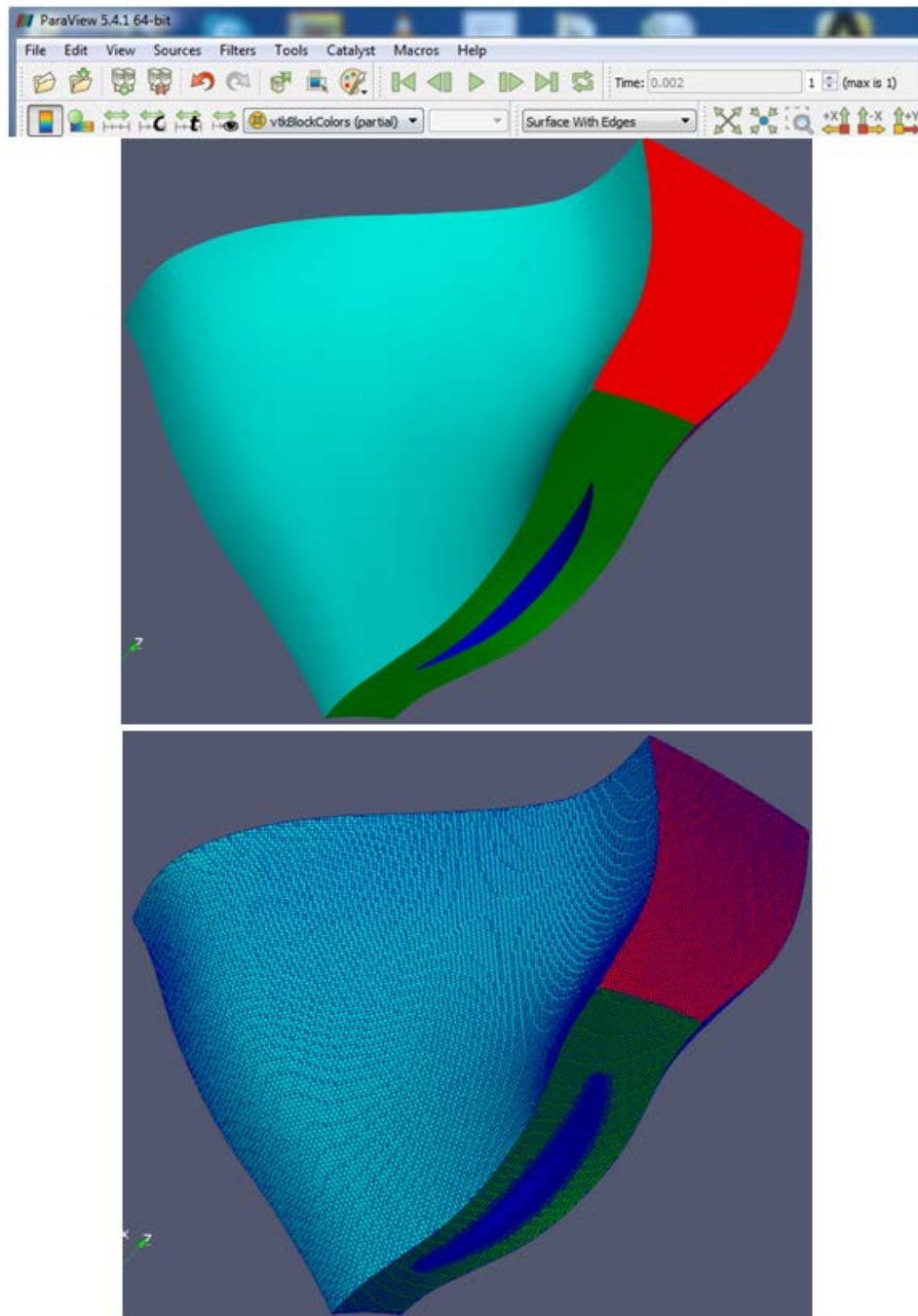


Figure 4. 19 - Surface snapping result in snappyHexMesh. mesh off(top), mesh on(bottom)

At this point the domain is completely mesh internally and externally. The third steps of *snappyHexMesh* process is adding layers which is considered optional.(Greenshields, 2017) This layer is added to the external surfaces few thickness in length base on user specification to refine more the external faces, this is necessary if the boundary layer thickness plays important role on the simulation. In this work boundary layer thickness is an important factor due to friction since this is turbulent transonic high velocity flow, but due to the complexity of the geometry adding layers will not always be successful(Giljarhus, 2018). On *snappyHexMeshDict* file, *addLayers* parameter is set to false(disabled) and resolved by testing multiple *snappyHexMesh* sensitivity runs with different refinements levels to get the finest mesh possible outcomes . Sample of sensitivity runs on different meshes are shown in Figure 4.20.

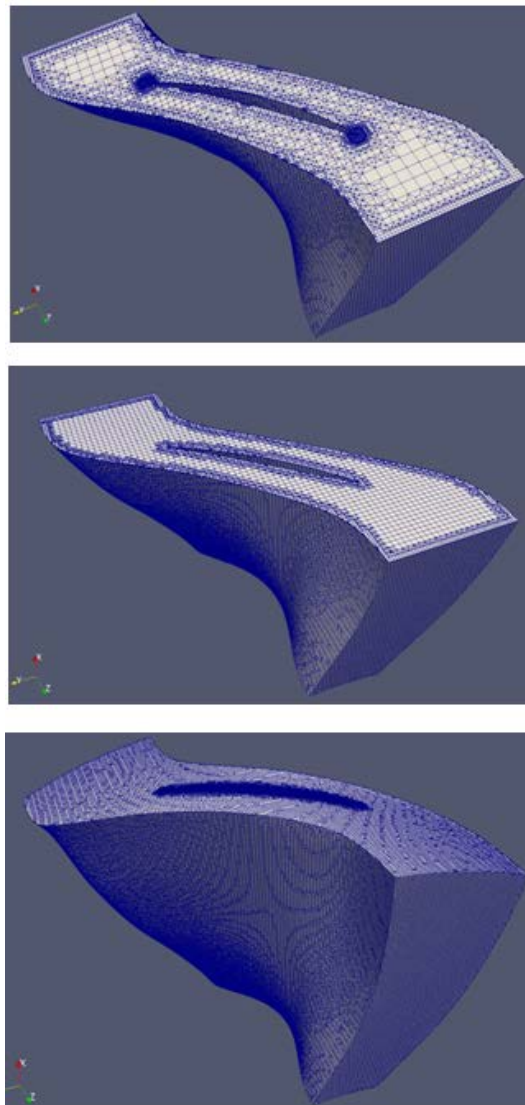


Figure 4. 20 - Different mesh refinement level sensitivity run of the computational domain in *snappyHexMesh*.
courser mesh(top), medium mesh(middle), finest attainable mesh (bottom)

Under these three main processes of *snappyHexMesh*, sub-dictionaries under each step process has parameters that needs to be filled out correctly in order to execute *snappyHexMesh* in *OpenFoam* otherwise meshing of the domain will not be successful. The complete *SnappyHexMeshDict* dictionary with parameters input of this work is shown on Appendix 1.

SnappyHexMesh unstructured meshing in *OpenFoam* is done by running *snappyHexMesh* in the case folder path DOS-prompt by keying-in *snappyHexMesh* command. The mesh results for each stage of the *snappyHexMesh* algorithm can be seen in Figure 4.18 to 4.19, of the castellated mesh and the snapped mesh respectively. Figure 4.22 shows the final mesh in the simulation with the finest mesh achievable where *snappyHexMesh* run is successful. It is worthy to mention that the tip gap portion on the final mesh is more refine to ensure that the grid has adequate resolution to resolve the leakage flow around the tip and the solid wall boundary layers. The finished run time and successful *snappyHexMesh* meshing can be seen on Appendix 2.

To checked the quality of the mesh, a utility in *OpenFOAM* libraries called *checkMesh* is run. *checkMesh* provides a list of values for certain mesh quality measures. It also produces a full report with mesh quality metrics and element count statistics. Details of the *checkMesh* quality report is shown on Appendix 3. If Mesh OK, there are no major problems. However, special attention is given to non-orthogonality and skewness values which must stay under 70 and 10 respectively. Figures 4.20 and 4.21 presents some mesh details. It contains 641232 mesh cells base on *checkMesh* quality report.

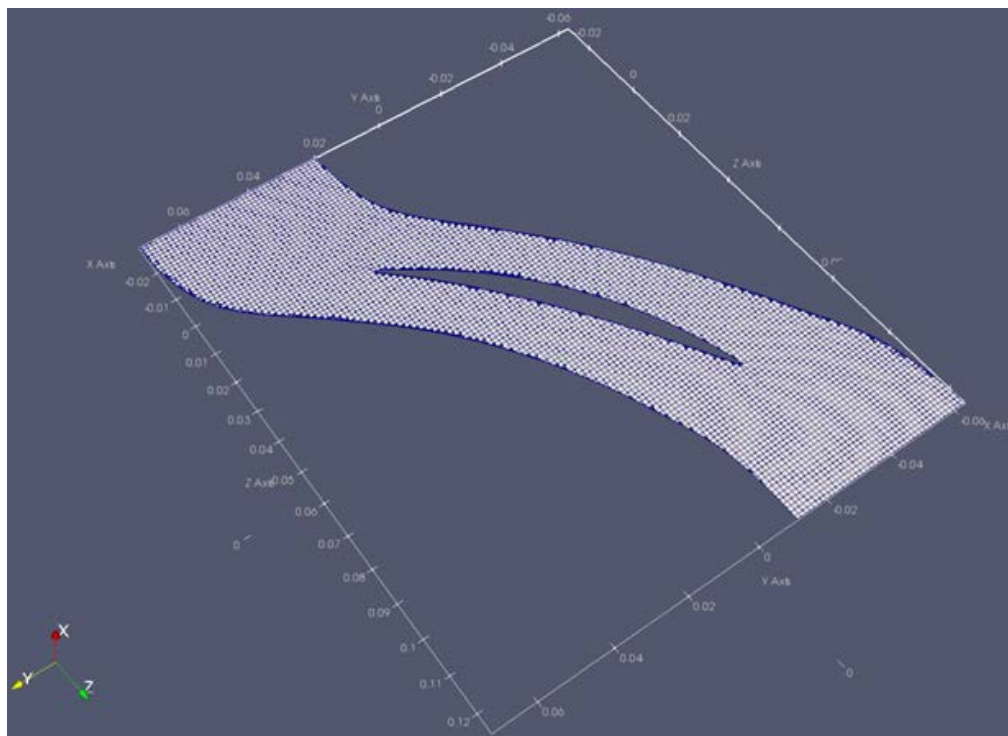


Figure 4. 21 - Blade section mesh detail

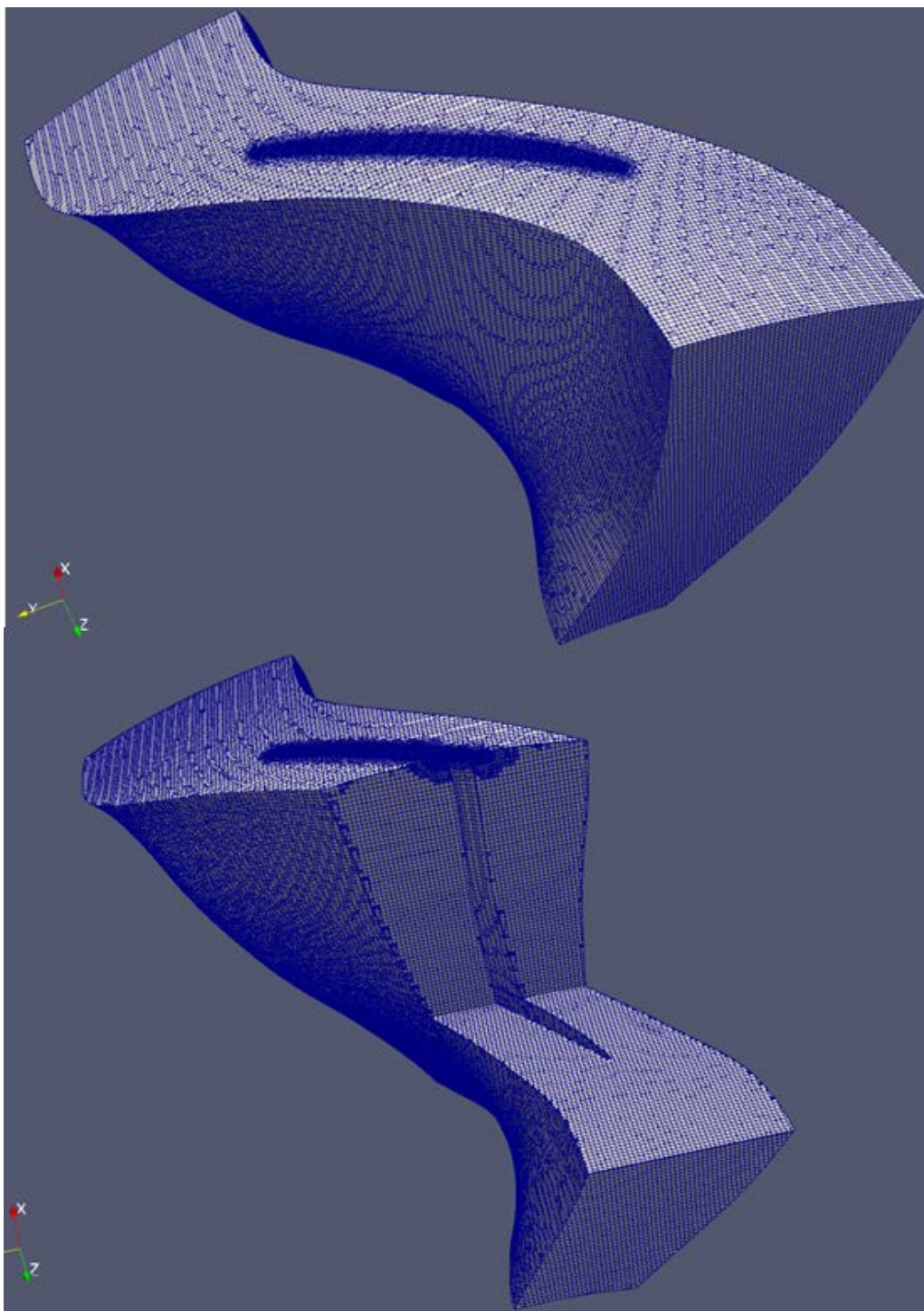


Figure 4. 22 - snappyHexMesh results of the computational domain. whole mesh(top), interior mesh cut-out view(bottom)

4.4.4. THE PASSAGE ROTOR COMPUTATIONAL DOMAIN

In this work, only one passage is meshed. Figure 4.23 shows the passage flow studied. It is impractical to conduct full annulus simulation because of huge computational time cost for a full annulus simulation

that consist of 22 blades. For 6.4×10^5 mesh cells, 22 blades can easily reach 14 million cells if whole annulus is considered and that can be intractable in modern computers. Using one passage is common practice because the simulation tool has option on specifying boundaries that virtually computes the full annulus. This boundary condition is referred to as *cyclicGGI* in *OpenFOAM* that would average field values on the meeting interface and then treated as periodic "circular array" base on the included angle input of one passage to reach full 360 degrees(More details on this on the boundary sections).

As mentions earlier, a single blade passage is modeled assuming blade passage to succeeding passage periodicity. Although full annulus analysis is needed to simulate the compressor rotating stall inception, the same flow phenomena can occur in a single blade passage during actual stall(Hah et al.,(2006)) and this is adequate assumption according to Davis et al. (Davis et al.,(2005)).

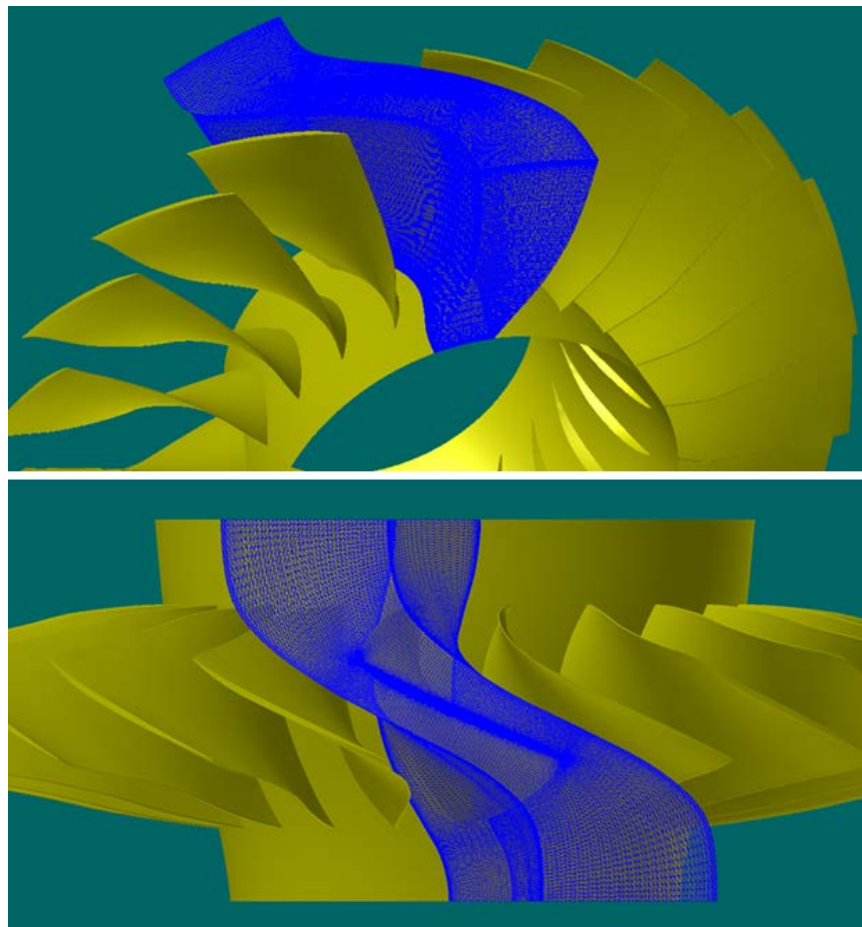


Figure 4. 23 - Passage Rotor Domain

4.5. NUMERICAL SET UP

4.5.1. THE SOLVER

Density-based solver implemented in *OpenFOAM* libraries named *rhoPimpleDyMFoam* is used in the simulations. A brief explanation of the selected solver name "*rhoPimpleDyM*" signifies the following:

ρ or density-based is for pressure and velocity coupling for high Mach number(transonic) compressible flows of the continuity equation. Algorithms of *PISO* and *SIMPLE* are combined to become *PIMPLE* algorithm which is used as an iterative procedures for coupling momentum and mass conservation equations for transient flows. "*DyM*" means dynamic mesh functionality which can handle optional mesh motion and topology changes described in *dynamicMeshDict* file. The *dynamicMesh* dictionary in this simulation is set to *staticFvMesh*, thus there will be no mesh motion because we are in the relative frame of reference.

Fluids and a rotating body interaction results velocity vectors that differs each other with respect to the rotating frame of reference. In this regard, additional dictionary to be coupled to the solver is added named *MRFZones* which denotes *Multiple Rotating Frames* and must be specified to the desired blade speed and the direction of rotation is specified with positive or negative value. The simulation has blade speed of 16042 rpm equivalent to 1680 rad/second. This dictionary not only sets the blade velocity but it is where also the relative frame of reference is defined in the mesh. The set of cells that defined the relative frame of reference was taken from the utility called *cellset* or *regionCellSets* in *OpenFOAM*.

transportProperties dictionary used Sutherland's law and links the absolute temperature to the dynamic viscosity, which is set to $1.8 \times 10^{-5} \text{ kg m}^{-1} \text{ s}^{-1}$. Additional details about the solutions and how governing equations implemented into the solver were already given in Chapter 3. See also Appendix 5.

4.5.2. TURBULENCE MODELING

As described in Chapter 3, the transonic density-based libraries were implemented in *OpenFOAM* using RANS equation for solving turbulence, so *turbulenceProperties* dictionary will be set to *RASModel*. Turbulence model specification comes with the *RASProperties* dictionary and it is set to *kOmegaSST*(k - ω -Shear Stress Transport) as the model of choice mention in Section 2.6. We considered computing the flow down to the walls and the distance to the nearest walls should be about two wall units(Piomelli, 1996) ($y^+ \sim 1$). This is some percentage of the total boundary layer thickness somewhere at the viscous sub-layer region shown in Figure 4.24.

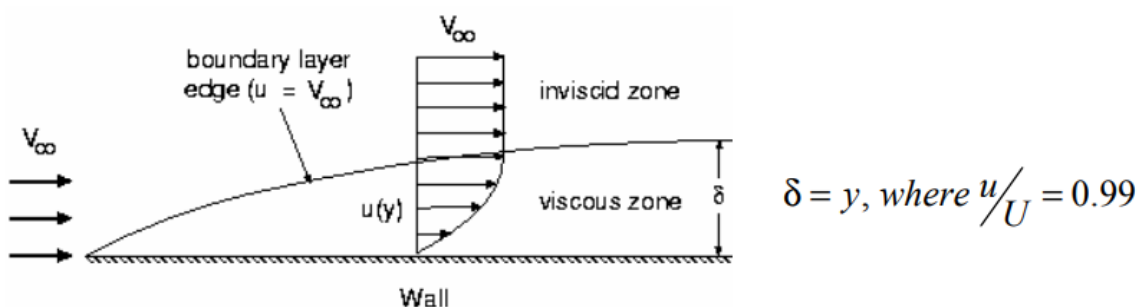


Figure 4. 24 - Boundary layer regions(Bakker, 2002)

4.6. INITIAL AND BOUNDARY CONDITIONS

In obtaining a meaningful solution, initial and boundary conditions must be supplied to the computational domain which are needed for defining both mesh and each field for Navier-Stokes equation. Figure 4.25 details the boundary conditions used in the analysis. At the start, the calculation of the flow properties everywhere inside the plenum are assumed to be uniform, such that pressure at inlet to outlet are the same and the velocity is a function of total temperature, T_0 at the inlet. As the compressor begins to draw air in, the pressure at inflow drops relative to the outflow and the mass flow rate begins to gradually change with time. The mass flow reaches either steady state or at cycle oscillation, depending on whether the compressor is running close to design conditions or at off-designed stalled conditions. The implementation of the initial and boundary conditions is presented in this section.

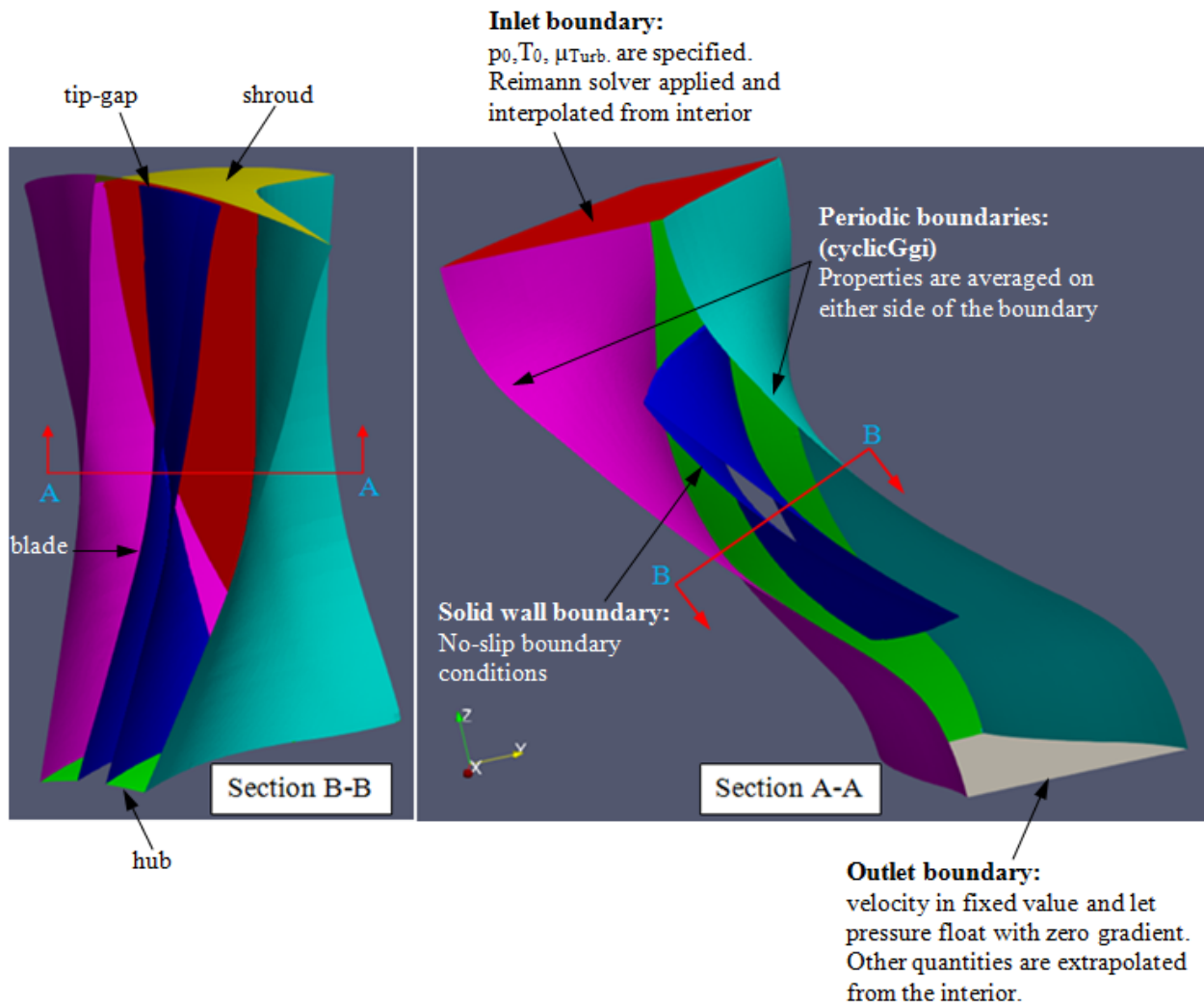


Figure 4. 25 - Boundary conditions used in the analysis

4.6.1. INLET BOUNDARY CONDITION

In this boundary, the stagnation temperature, T_0 , and the total pressure, p_0 , are assumed to be known. These quantities may be set as ambient conditions as the compressor is drawing air from the atmosphere. Therefore, standard day conditions are imposed at inlet so that all solution data can be compared with experimental results. Table 4.1 shows the parameter values at this boundary condition. In order to built the compressor map, a back pressure is specified equal to 115000 Pa to compare with experimental data. Since the compressor does not have inlet guide vane(IGV), it is safe to assume that swirl does not exist at inlet and the tangential velocity component is set to zero. At the inlet, to account for the effect of acoustic disturbance, Reimann characteristic equation explain in section 3.1.2. is applied.

Inlet Boundary Condition
$p_0 = 101325 \text{ Pa}$
$T_0 = 288.15 \text{ K}$
$\mu_{\text{Turb}} = 0.0001 \text{ Pa s}^{-1}$

Table 4. 1 - Inlet Boundary Conditions

4.6.2. OUTLET BOUNDARY CONDITION

The exit static pressure is iteratively adjusted until the prescribed mass flow rate is achieved. All other quantities such as the density, the three components of velocity and turbulence quantities are interpolated from the interior of the domain. There is a back-flow control that switches the pressure at outlet to *zeroGradient* if indeed backflow occurs. This is implemented in OpenFOAM foam through *inletOutlet* boundary condition name sub-dictionary to fix the velocity with *fixedValue* and let pressure float with *zeroGradient*.

4.6.3. WALL BOUNDARY CONDITION

All walls are modeled as adiabatic and with no slip conditions. This condition is applied to the hub, casing and blade surfaces. The velocity on the walls of the inlet is set to zero, while the velocity for the grid points on the compressor blades and shaft, that part which is moving, is set to $\vec{\omega} \times \vec{r}$. The temperature values at the solid surfaces are directly extrapolated from the interior flow field since it is assumed that adiabatic wall boundary condition. The pressure is found by solving the momentum equation in the normal direction to the blade surfaces. The density values are found from continuity equation after temperature and pressure are computed. Turbulence wall boundary conditions in OpenFOAM is at *turbulenceProperties* dictionary with *thermophysicalProperties* values that can be found in Appendix 5.

4.6.4. PERIODIC BOUNDARY CONDITION

Since only one passage is modeled, it is assumed that the flow through first blade and the last blade passage are nearly identical and a periodic boundary condition is applied. At the two side faces, the flow properties values are computed by averaging the properties on either side of the periodic boundaries. The C-grid cut accounts for the neighboring blade passages, see Figure 4.26.

Implementing periodic boundary in *OpenFOAM* uses *General Grid Interface*(GGI) for cell periodic boundary faces that does not match before interpolation can be done. Because the number of cells in the suction side is usually different in the pressure side, *cyclicGGI* is used as periodic boundary-this couples the two rotationally cyclic face patches. The dictionary reads as below, see Figure 4.27.

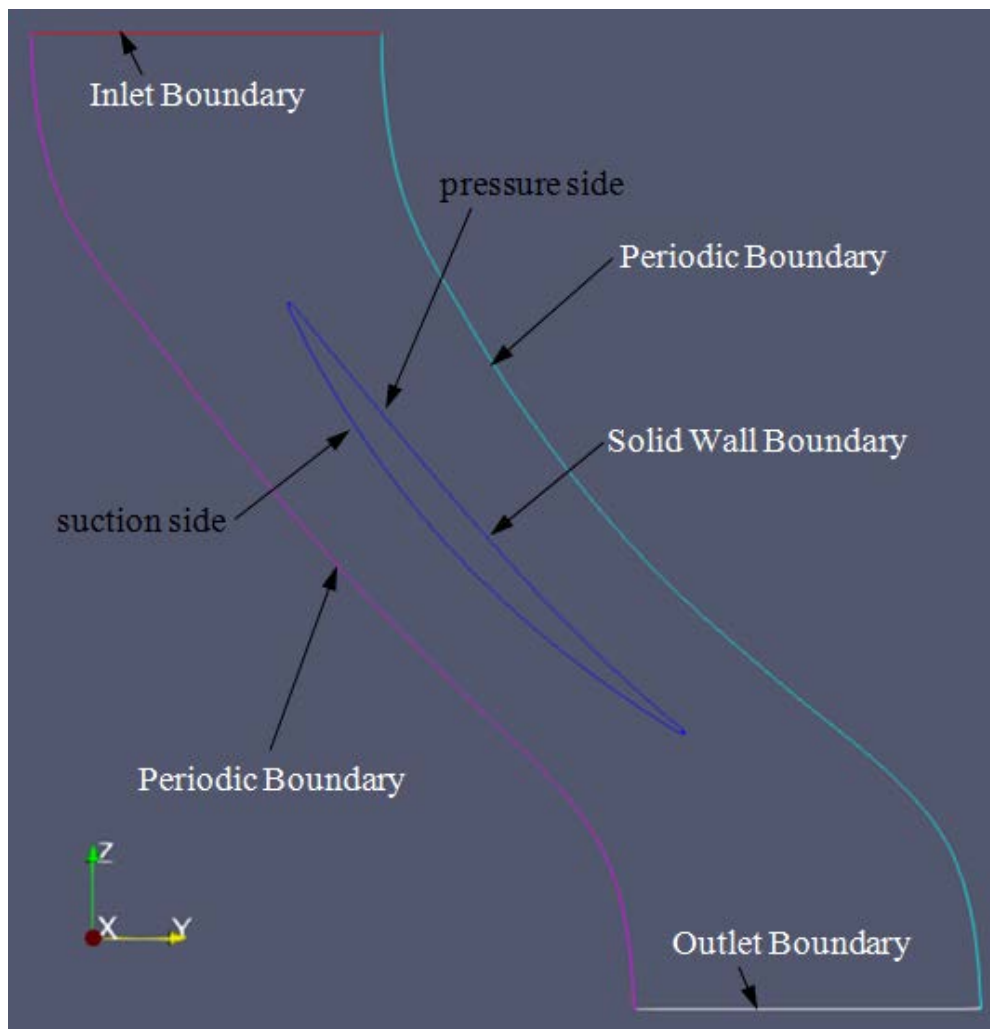


Figure 4. 26 - C-Grid boundary cut of the computational domain

```

1 /*----- C++ -----*/
2 |=====|
3 | \ \ \ \ | F i e l d | OpenFOAM: The Open Source CFD Toolbox
4 | \ \ \ \ | O p e r a t i o n | Version: 5.x
5 | \ \ \ \ | A n d | web: www.OpenFOAM.org
6 | \ \ \ \ | M a n i p u l a t i o n |
7 /*-----*/
8 /* windows 32 and 64 bit porting by blueCAPE: http://www.bluecape.com.pt */
9 | Based on windows porting (2.0.x v4) by symscape: http://www.symscape.com |
10 /*-----*/
11 FoamFile
12 {
13     version      2.0;
14     format       ascii;
15     class        polyBoundaryMesh;
16     location     "0.002/polyMesh";
17     object       boundary;
18 }
19 // *****
20
21     Periodic
22     {
23         type      cyclicGgi;
24         nFaces    5379;
25         startFace 1870025;
26         shadowPatch Periodic_2;
27         zone      periodicZone;
28         bridgeOverlap false;
29         rotationAxis (0 0 1);
30         rotationAngle -16.363636;
31         separationOffset (0 0 0);
32     }
33     Periodic_2: vice versa
34
35 // *****

```

Figure 4. 27-Periodic boundary cyclicGgi dictionary

Periodic, the boundary condition name and refers to the repetition of the rotor domain. *type* specifies the kind of boundary condition whether *nFaces* and *startFaces* refer to which faces the boundary is assigned. *shadowPatch* is the name of the boundary patch which makes a pair for the repetition, therefore this needs similar entry as the boundary name assigned as *periodic_2*. *zone* defines the global position for the boundary faces to treat the parallelism assigned as *periodicZone*. *bridgeOverlap* is a parameter that checks if every face in the specified boundary is covered in the corresponding pair, setting to *false* disallows partially or completely uncovered faces. *rotationAxis* defines the rotation axis of the *rotationAngle*. *rotationAngle* specifies how many degrees (-16.363636° for 22 blades to cover full 360°) the patch should be rotated about its rotation axis to match the *shadowPatch*. *separationOffset* is used for translational cyclic patches, that is why it is set to (0,0,0).

CHAPTER 5: RESULTS AND DISCUSSION

The numerical schemes and case settings discussed in the last two chapters were implemented as a case of the NASA Rotor 67 CFD simulation. After setting all the required fields of the case explained in section 4.2.1, *rhoPimpleDyMFoam* solver has to be checked that the case run and solution converged. The solution is converged and the final residual of the equation is solved when the residual is approaching zero. Getting and plotting the residual is explained in section 4.3.2. Sample plot of the converged residual is shown in Figure 5.1. The sample parameters taken which are pressure, horizontal and vertical component of velocities converged at almost 140 iterations (time is not a physical time, but solver iteration of the solutions) giving very small or relatively zero deviation of the correct solution. Therefore, the discretization and physical model is adequate in which CFD solution converged and gives good result. In Appendix 4, a portion of the *rhoPimpleDyMFoam* solver output will re-enforce these results showing other indicators of successful convergence.

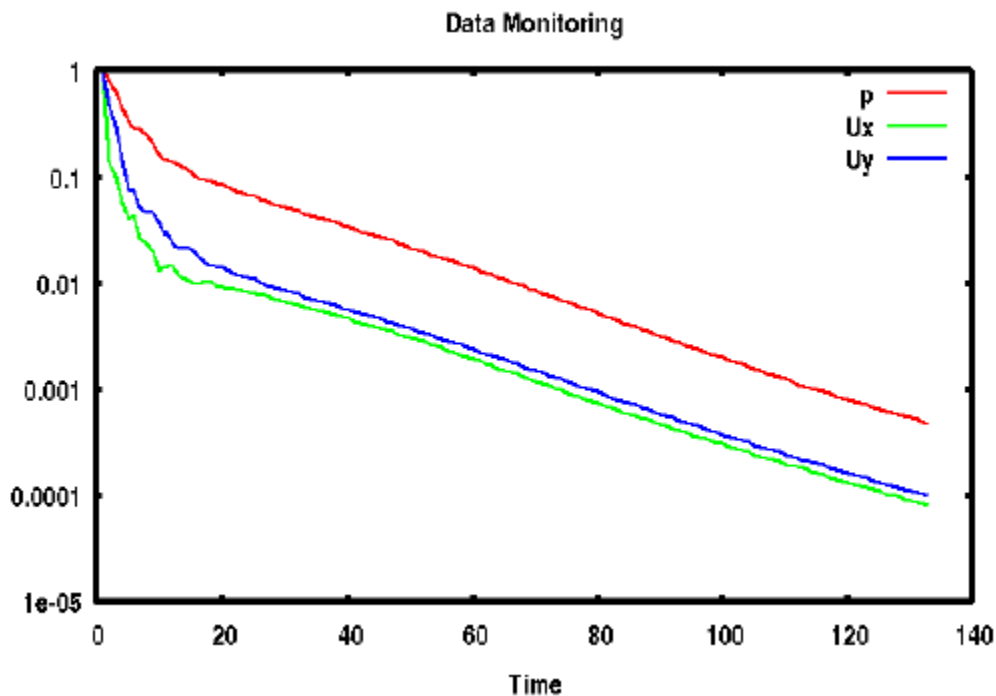


Figure 5.1 - Sample of the residual plot

In this chapter, results and discussions are being presented. Securing the required data and relevant extraction and calculation of parameters to produce plots, graphs and contour representations were discussed in the last four chapters. In Section 5.1, comparison of the experimental data with the CFD results are given in the form of contour plots, graphs and streamlines at the peak efficiency condition while Section 5.2 presents the results on the onset of stall and stall initiation.

5.1. RESULTS ON PEAK EFFICIENCY CONDITION

In the present study, the solver was applied to the flow simulation of NASA Rotor 67 compressor at peak efficiency conditions, for which experimental results may be found in Reference work of A.J. Strazisar et al. (A.J. Strazisar et al., (1989)) The CFD case results are presented and compared with the experimental data.

As pointed out in Section 4.6, the flow properties in the computational domain were assumed to be uniform and were set to their inlet free stream ambient condition values. As the flow field advanced in time, the pressure at the inlet drops relative to the outlet flow. This drop in pressure depends on the compressor speed. Since NASA Rotor 67 is a transonic compressor at its design speed, the pressure drops, particularly in the blade suction side near the leading edge and expected to produce close to no pressure in that region. The pressure was allowed to drop in the suction side of the blades gradually to achieved steady state flow. To observed possible stall, different speeds were tried in the simulation: sampling 30% of the design speed, 50% and 100% of the design speed. At each time step mass flow is collected at each trial together with the total pressure. Thus, total pressure were also checked. The radial distribution of the total stagnation pressure were averaged across the annulus to calculate the total pressure ratio using equations discussed in Chapter 1 which is Equation (1-10) in particular for pressure ratio. Figure 5.2 shows the periodic fluctuations of mass flow rate values can be observed. Total pressure fluctuations also plotted in Figure 5.3. There is 1.2% difference between the computed mean mass flow rate versus the experimental data, the later is 36.62 kg/sec while the former is 34.23 kg/sec base on the result. What this means is that the mass flow and total pressure fluctuations on this peak efficiency operating condition are very small, less than 1%.

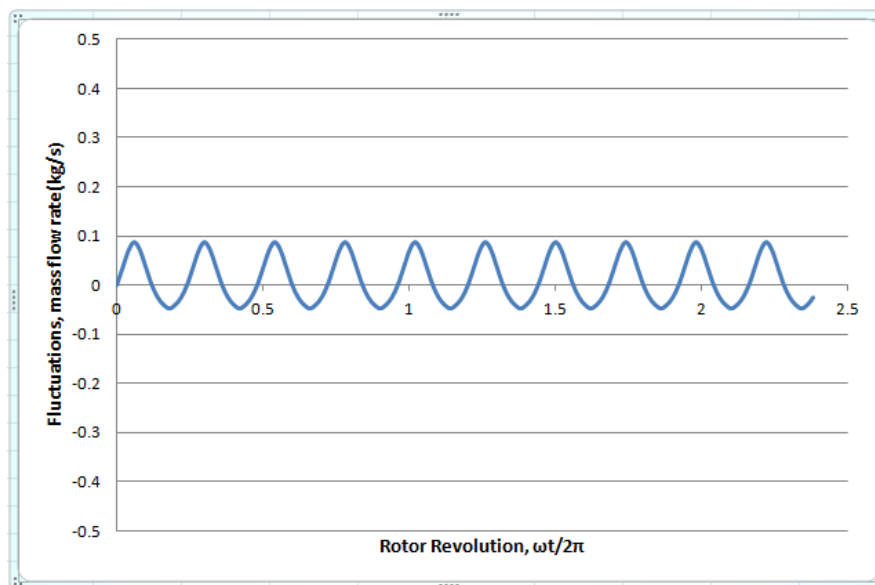


Figure 5.2 - Peak Efficiency condition time history of mass flow rate fluctuations

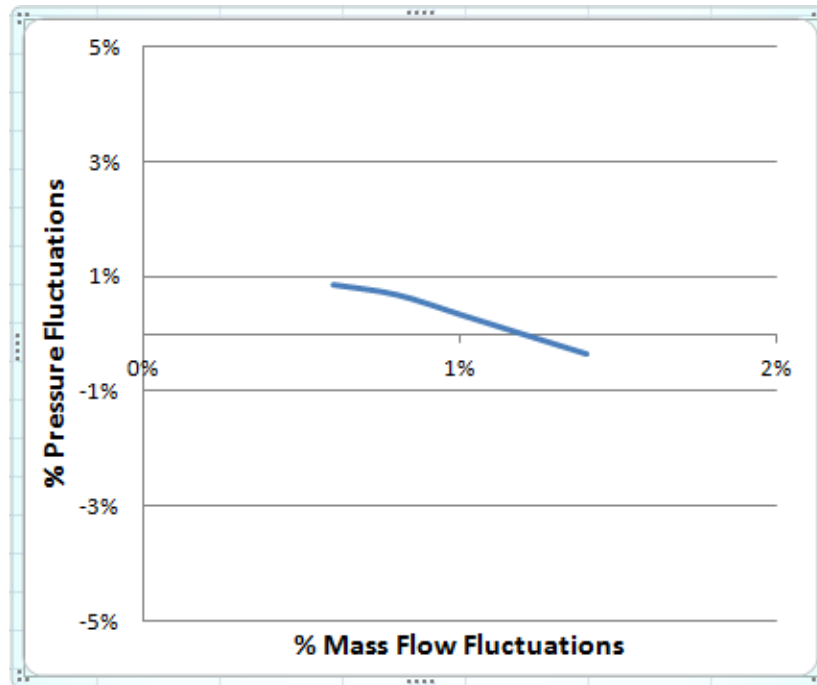


Figure 5. 3 - Pressure and mass flow rate fluctuations at peak efficiency conditions

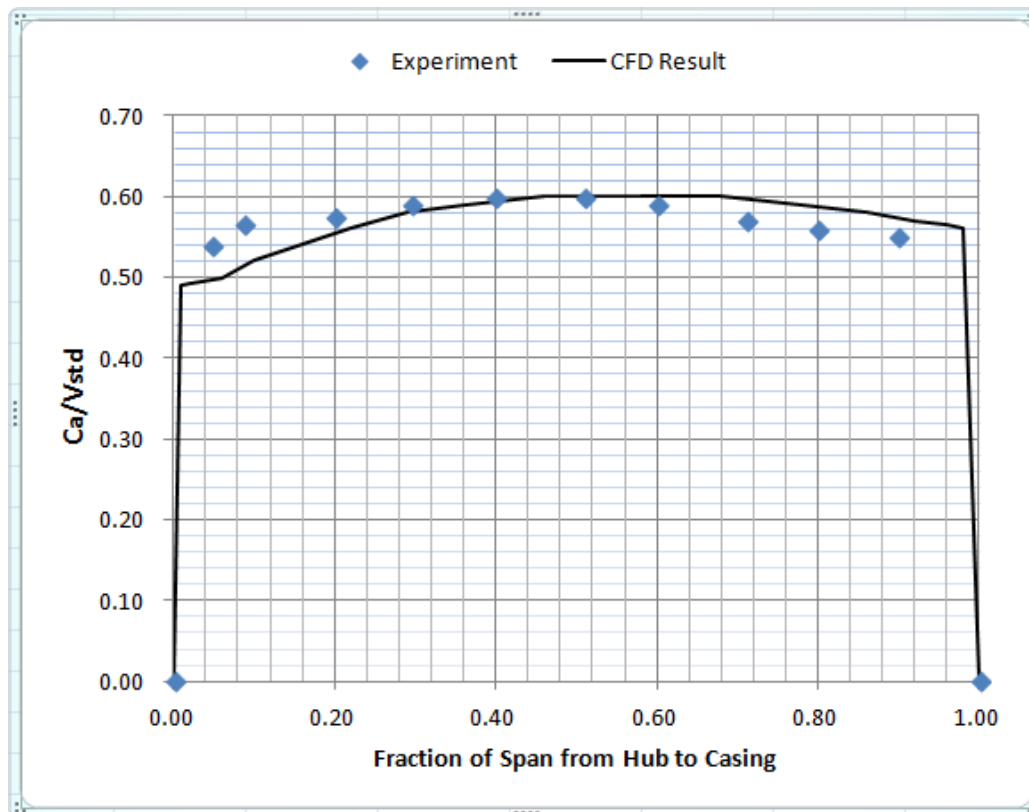


Figure 5. 4 - Comparison between the CFD Results and experimental results of inlet axial velocity(C_a) at peak efficiency conditions

Figure 5.4 shows a comparison between CFD prediction and the measured normalized axial velocity distribution at the inlet survey station 1 in Figure 4.4. The velocity is normalized by critical velocity at standard day conditions, $V_{std} = 310.63$ m/sec. CFD result is compared to the measured data and good agreement were obtained as shown on Figure 5.4. It is also seen that the grids have enough resolutions to capture the boundary layer profiles near the walls at 0%(hub) and 100%(shroud).

The shock boundary layer interactions, 3-dimensional shock system, clearance flow and three-dimensional separation makes a very complicated flow pattern for a transonic flow such as this NASA Rotor 67. Relative Mach number comparison between experiment and CFD result at a specified span location is shown of Figures 5.5 through 5.6. Figure 5.5 shows the relative Mach number contours at the 70% span locations, measured from the shroud. Experimental contours were obtained from the work of (Anthony J. Strazisar, 1989) et al. Good quality contour maps can be hardly produced as can be seen, this were attributed due to background noise, blade flash stability of the laser anemometer, non-uniform survey locations in viscous regions and the wakes due to turbulent flows all contributing to poor quality plots. Experimental contours undergone interpolation and smoothing as detailed on the Reference work(Anthony J. Strazisar, 1989) et al. The Mach numbers were 0.95 and 0.60 at the inlet and outlet respectively on the experimental result.

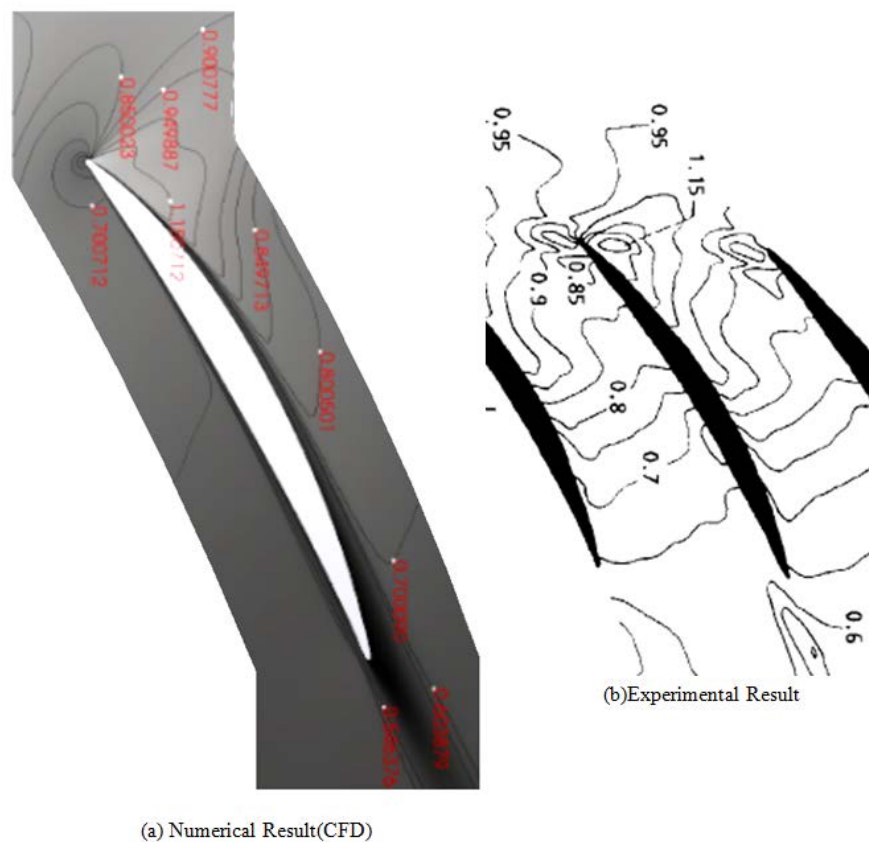


Figure 5. 5 - Mach number plot at 70% span from shroud near peak efficiency

CFD calculations showed that most of the flow at this span location is subsonic. But small regions having supersonic flow, with relative Mach numbers about 1.150712 were observed few position ahead of the suction surface of the blades. The numerical results in Figure 5.5 show shear layers over the blade and in the trailing edge that are not visible in the experimental contour plots. This may be due to lack of adequate stable measurement locations in the viscous regions as earlier mention.

Figures 5.6 and 5.7 show the experimental and CFD computed result of relative Mach number at 10% span at two different azimuth locations 30% and 50% pitch. To emphasized zero percent and 100 percent chord on these plots represent the blade leading and trailing edge, respectively. There are shock structure that was observed and the comparisons generally agree well with each other, though there is a maximum difference of five percent(5%) between the experiment and the computed.

The static pressure contours and shock locations of the flow passage at two different radial positions, 30% and 70%, are shown in Figure 5.8. This shows how the pressure through the compressor builds up. Following Bernoulli theory, both of these radial locations pressure drops on the blades suction surfaces as

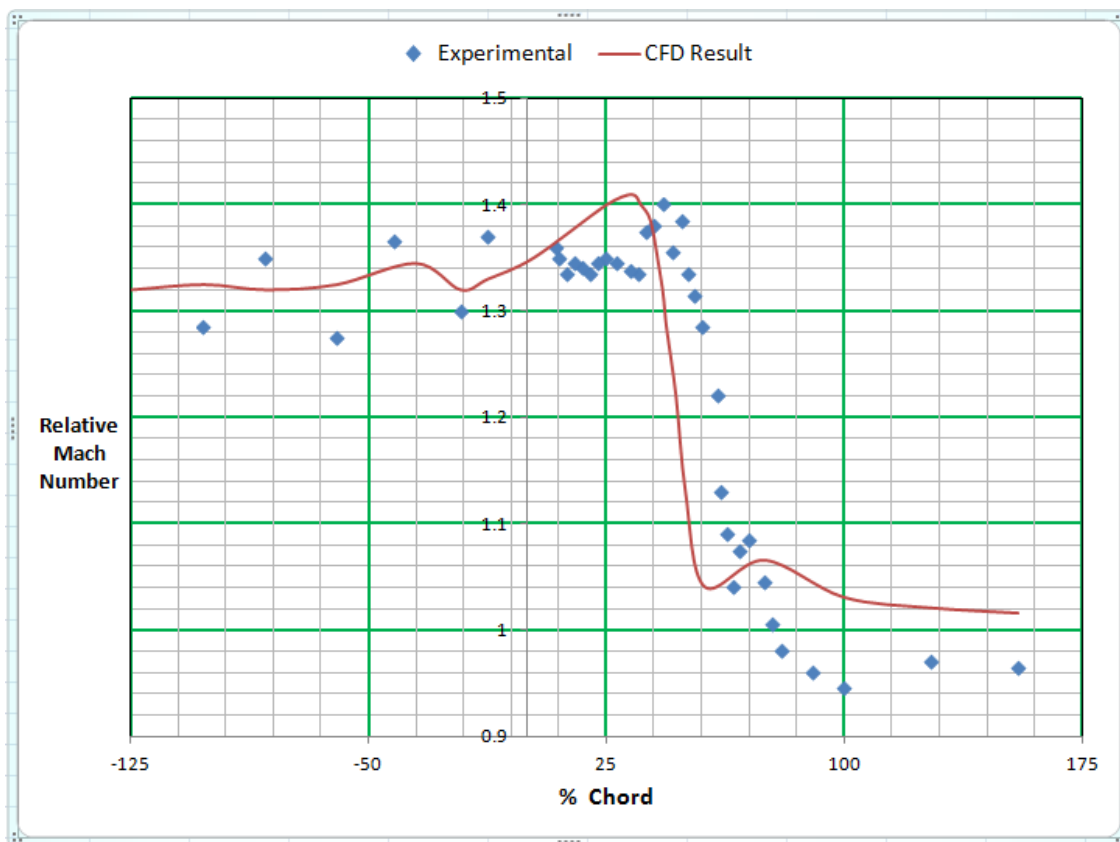


Figure 5. 6 - Comparison between experiments and CFD results of relative Mach number at 10% span and 30% pitch at peak efficiency conditions

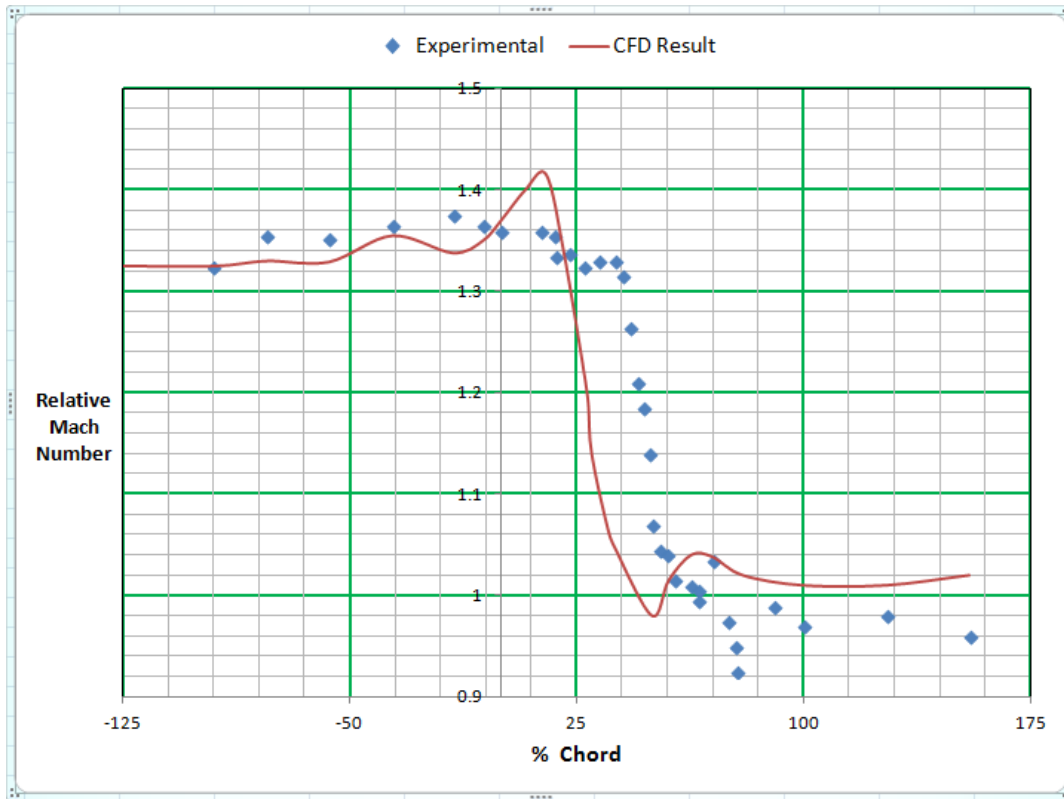


Figure 5.7 - Comparison between experiments and CFD results of relative Mach number at 10% span and 50% pitch at peak efficiency conditions

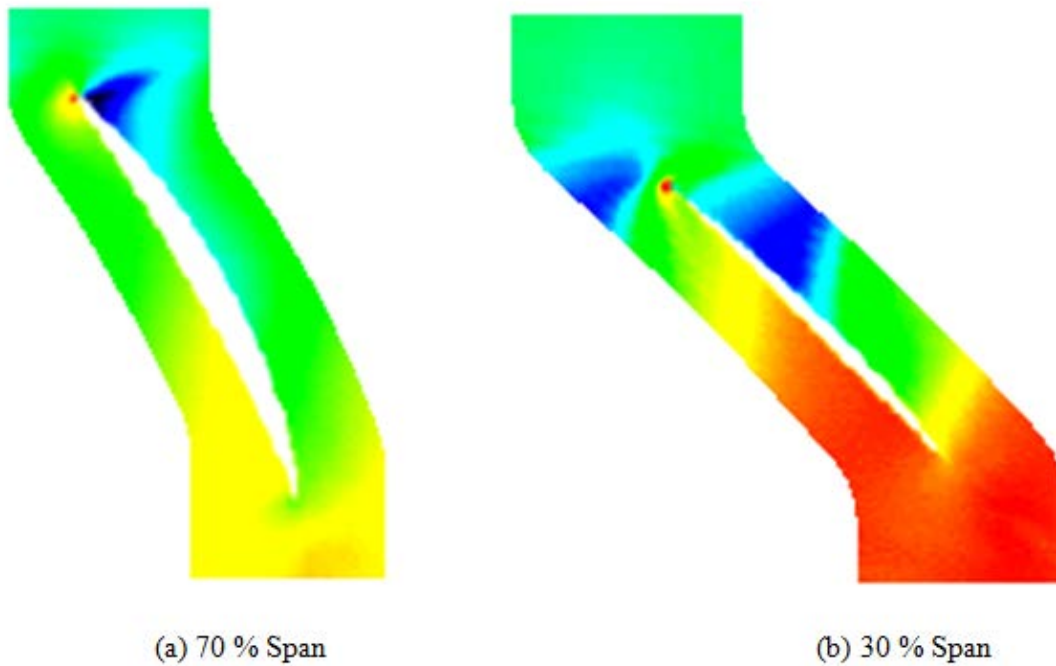


Figure 5.8 - Static pressure gradient contour plots at 30% and 70% span at peak efficiency conditions

a consequence of flow acceleration. The static pressure gradient is much higher at 30% span than that of 70% span location, which means it(30% span) has a low total pressure. This conforms with the theory since at 30% span, radial velocity is higher than that of 70% span. Also a bow shock occurs, the shock is very strong at the upper portion of the blade(near tip) than close to the hub(70% span). This is strongly influenced by a vortex roll-up on the leading edge that is close to the hub. Details of this will be discuss on the next section. At the pressure side of the blades, no shock forms on this surface boundary layer.

Figure 5.9 shows the relative velocity vectors at 50% span viewed from the top of the rotor. It can be seen that the shock of the flow domain, velocity vectors nearly covers the gap of the blade, suggesting choke conditions are imminent. There is no evidence of reversed flow as velocity profiles are well behaved in the passage. The velocity flow field were almost identical on the entire domain, such a well-behaved flow is of course expected at the peak efficiency conditions.



Figure 5. 9 - Relative velocity vectors at mid-span(50% span) at peak efficiency condition

5.2. STALL INITIATION

The stable design condition results under peak efficiency condition was discuss in the previous section of the test case NASA Rotor 67. It had find out that at selected operating point, it has a very small pressure and mass flow fluctuations. From the contour and velocity vector plots, no disturbance were observed and the flow were uniform. As been discuss earlier on introductions and literature review, from this stable

point when mass flow is increased or decreased, instability and disturbance grow leading unstable conditions. In this section, this is what we are going to find out by initiating stall through reduction of mass flow, as this is also one of the main goal of this work. Results will be presented in the succeeding sections.

5.2.1. RESULTS OF INDUCING STALL

To study the flow structure as the compressor approaches towards stall, the flow fields along a compressor speed line are simulated. As already been point out earlier, a single blade passage is modeled assuming blade passage to succeeding passage periodicity. Although full annulus analysis is needed to simulate the compressor rotating stall inception, the same flow phenomena can occur in a single blade passage during actual stall inception while requiring much lower computational cost(Hah et al.,(2006)). This assumption is considered adequate up to stall inception point(Davis et al.,(2005)).

As mentioned earlier, the compressor performance map is the relation between the total to total pressure ratio and the compressor mass flow. In this study, the flow solver was run for 10 different operating conditions to construct the overall rotor performance map. This is done by running the compressor to the targeted mass flow rate and letting the static back pressure float. From the pressure difference between the inlet and outlet, that mass flow rate through the compressor can be calculated and the performance map obtained with the operating points. The radial distributions to total temperature and stagnation pressure are mass averaged across the annulus.

The calculated total pressure ratios at full speed are plotted against the normalized mass flow and compared to the experimental data (A.J. Strazisar et. al.,(1989)) is shown in Figure 5.10. The calculated and experimental data are non-dimensionalized by their corresponding choked mass flow rates. The calculated CFD result choked mass flow rate is 34.7 kg/sec and the experimental choked mass flow rate of NASA Rotor 67 is 34.96 kg/sec, there is a 0.7% difference. It can be seen that the performance map agrees well with the experimental data. Three points indicated on the performance map A, B, and C, are the operating points that the detailed flow field was studied. Point A represents the peak efficiency condition that was studied in the previous section, point B represents the near stall operating condition and point C is in stall condition.

A mass flow rate convergence history for points A, B, and C is shown in Figure 5.11. Decreasing the mass flow rate after point B causes the compressor to stall. It is observed that as the mass flow rate through the compressor decreases and the compressor approaches stall, the fluctuations in the mass flow rate is increasing slowly up until near stall where it increases more. Therefore, monitoring these fluctuations can be used to detect the onset of stall.

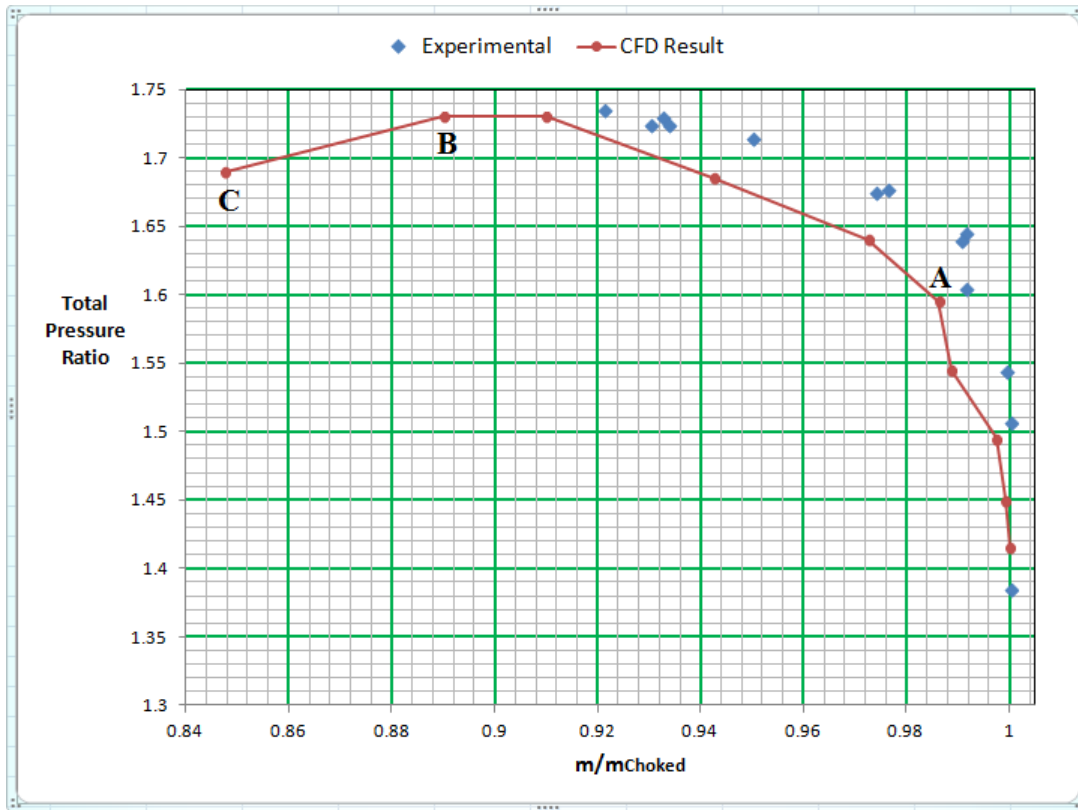


Figure 5.10 - Experimental and CFD Result Comparison of the Performance map

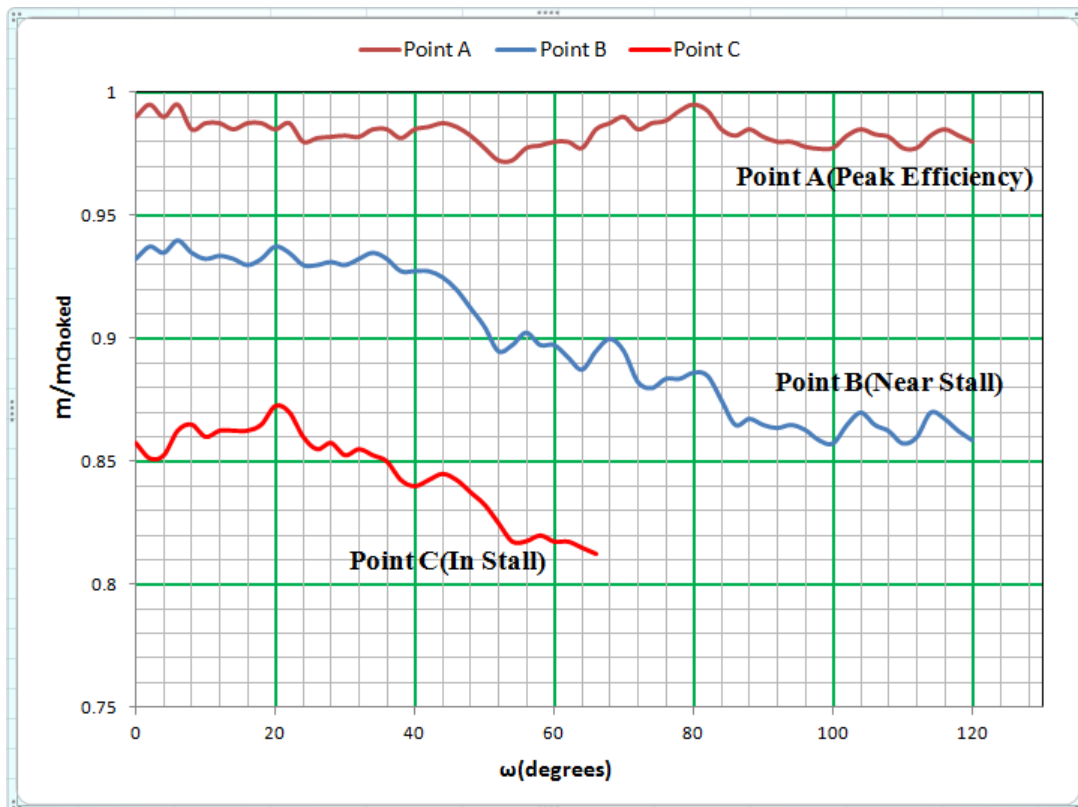


Figure 5.11 - Mass flow rate convergence history for NASA Rotor 67 operating points A, B, and C.

The ratio of the ideal input work needed to raise the total pressure of a working fluid from lower(p_{01}) to higher pressure(p_{02}) to the actual work needed to accomplish this process is called adiabatic efficiency of the compressor. The adiabatic efficiency of the compressor is calculated using the formulas obtained from equations (1-11) to (1-15). Figure 5.12 shows the comparison of the experimental and CFD computed adiabatic efficiency for different operating conditions. As can be seen, the experimental peak efficiency result occurs at a slightly lower mass flow rate as compared to the CFD results.

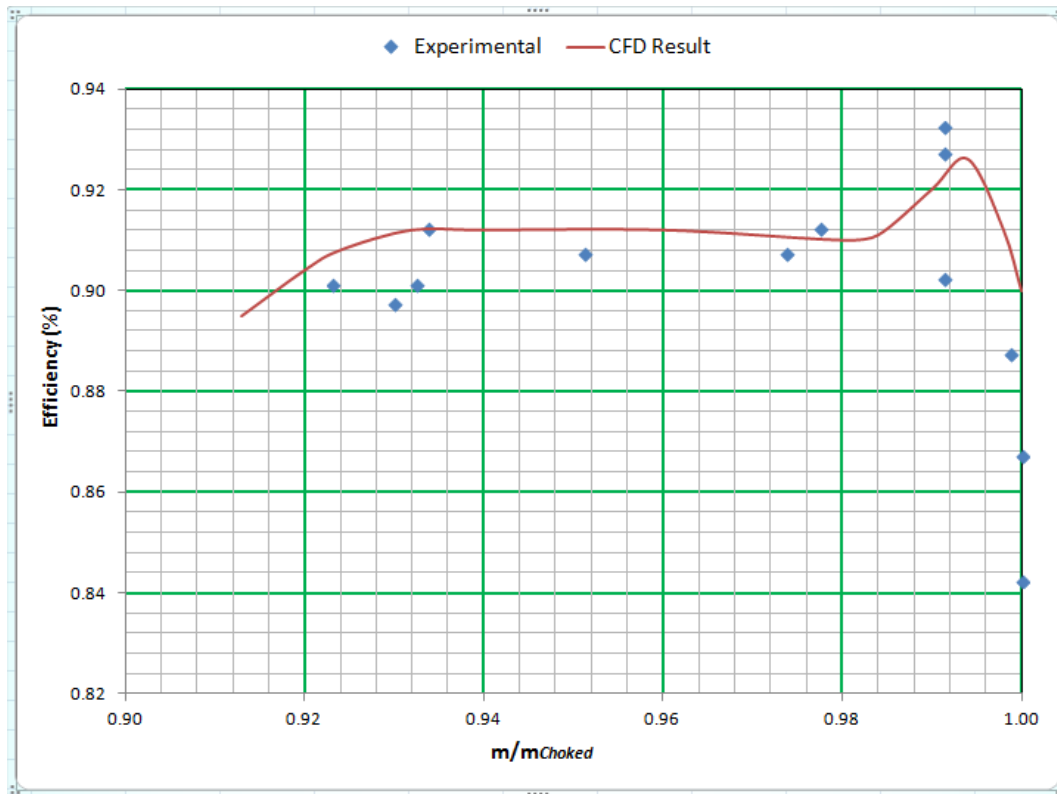


Figure 5.12 - Comparison of experimental (AJ. Strazisar et al. (1989)) and CFD computed adiabatic efficiency

As discussed in Chapter 2, tip clearance flow is one of the causes of flow instabilities leading to stall inception. Flows in this region play a very important role in stall inception of compressors. The interactions between the shock wave and the tip clearance have been the primary cause of stall in transonic compressors. This has been studied by some researchers, experimental (K. Suder et al. (2001)) and numerical (Zaki, 2009) investigation indicated that stall initiates in the tip region of the rotor.

Therefore, the role of the tip clearance flow and the shock wave as the compressor throttles is examined to explore the flow mechanisms and the physical trends leading to stall at the tip region. To do so, the averaged flow fields at two operating points A and B along the compressor map shown in Figure 5.10 are studied. Point A represents the peak efficiency condition and point B represents the near stall operating condition. The flow field in the rotor tip region for both operating points A and B is studied in

detail. The turbulence model used is the $k-\omega$ -SST in carrying out the simulation as discussed earlier. The results shown in the current work are obtained from single passage simulations and copied to the neighboring blade passage for better visualization. Contour plots and vector flow fields are presented.

The shock wave and tip clearance flow and its interactions are investigated. Using *calculator* Filters in *Paraview*, where it is possible to input independent parameter to conduct calculation 'on the fly' using the resulting CFD numerical results were used to plot non-dimensional contour plots. Figures 5.13 and 5.14 shows the non-dimensional static pressure contours in the tip section of the rotor blade and in the tip clearance region respectively for both points A and B. This regions at the tip section of the blade are independent of the frame of reference. When the rotor rotational velocity is combined with the main flow axial velocity, supersonic flow appears due to its transonic flow nature, and the relative Mach number exhibits shock formation when it exceeds unity. Tip vortices and tip clearance leakage flow are generated in the flow due to the pressure difference between the suction side and the pressure side of the rotor blade which is of the same manner with the aerofoil principles. High pressure flow from the blade's pressure surface rolls over the blade tip to reach the lower pressure flow at the blade's suction surface. Rotor tip leakage interacts with the main axial flow creating a vortex sheet that rolls up into the leakage vortex as it travels further. The formation of the tip leakage flow vortex reduces the effective main flow stream area and adds more blockage to the flow passage. As the mass flow rate through the compressor decreases, the angle of the tip vortex will increase, encroaching at a more forward location on the adjacent rotor blade surface. This in turn can cause the flow to spill over the adjacent blade leading edge and induce stall (A.D. Hoying et al. (1998)) & (D.H. Vo et al.).

As the compressor operates towards stall from the peak efficiency point A to the near stall operating point B, as shown in Figure 5.13, the following flow phenomena are observed. Base on the figures, darker regions represent low pressure areas and lightly shaded regions correspond to the high pressure areas. For the peak efficiency operating point A in Figure 5.13a the very dark is the low pressure area extending from the rotor tip till middle passage represents the tip clearance leakage flow vortex as it travels downstream. This figure shows that the shock wave is very close to the rotor leading edge and the shock in the front is uniform. The shock wave passes continuously across the passage where it intersects to the tip vortices and bends. For the near stall operating point B, in Figure 5.13b, the low pressure area which is very dark in the figure near rotor tip represents the tip clearance flow leakage vortex as it travels downstream. This shows that the shock wave is stronger and stands away upstream from the rotor leading edge. The shock wave front becomes non-uniform which indicates the high unsteadiness of the shock wave at the near stall condition. Compared with the peak efficiency condition, the shock wave passes continuously across the passage where it intersects the tip vortex closer to the rotor blade suction surface.

It is worthy of mention that the shock wave then bends prior intersecting the rotor suction surface further upstream compared to the peak efficiency condition.

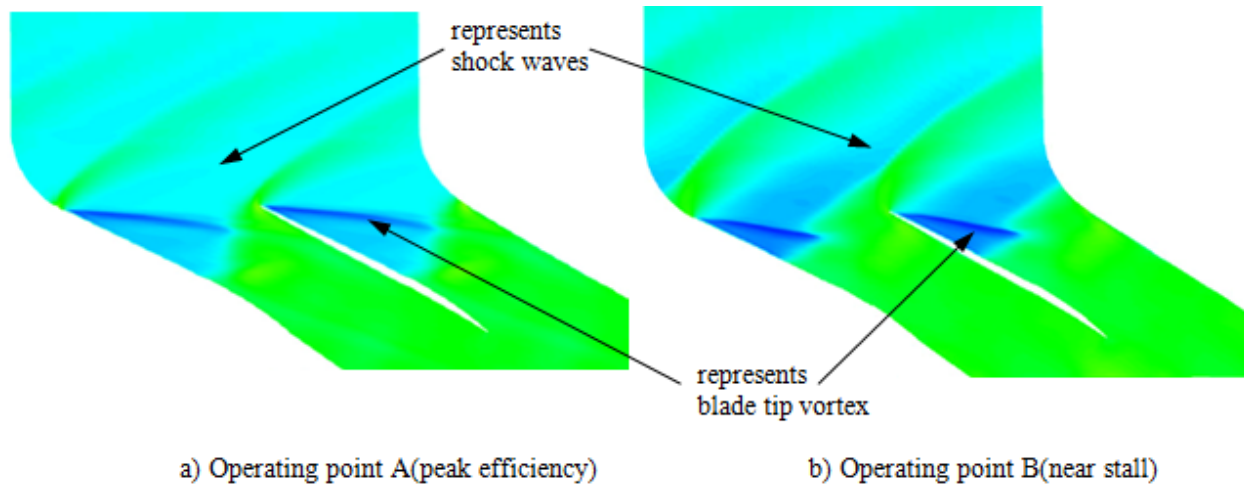


Figure 5. 13 - Tip section static pressure contours

Figure 5.14 shows the flow entropy contours at middle looking in meridional view plane for the peak efficiency operating point A and the near stall operating point B. Darker regions represent low entropy and lightly shaded regions represents high entropy in this figure. It is clearly observed that the entropy rises at the tip section. As can be seen, the entropy increases at the near stall condition as compared to the peak efficiency condition. The shock wave interactions with the tip vortex are not strong in peak efficiency condition as shown in Figure 5.14a while for the near stall condition(Figure 5.14b), it shows that the rotor

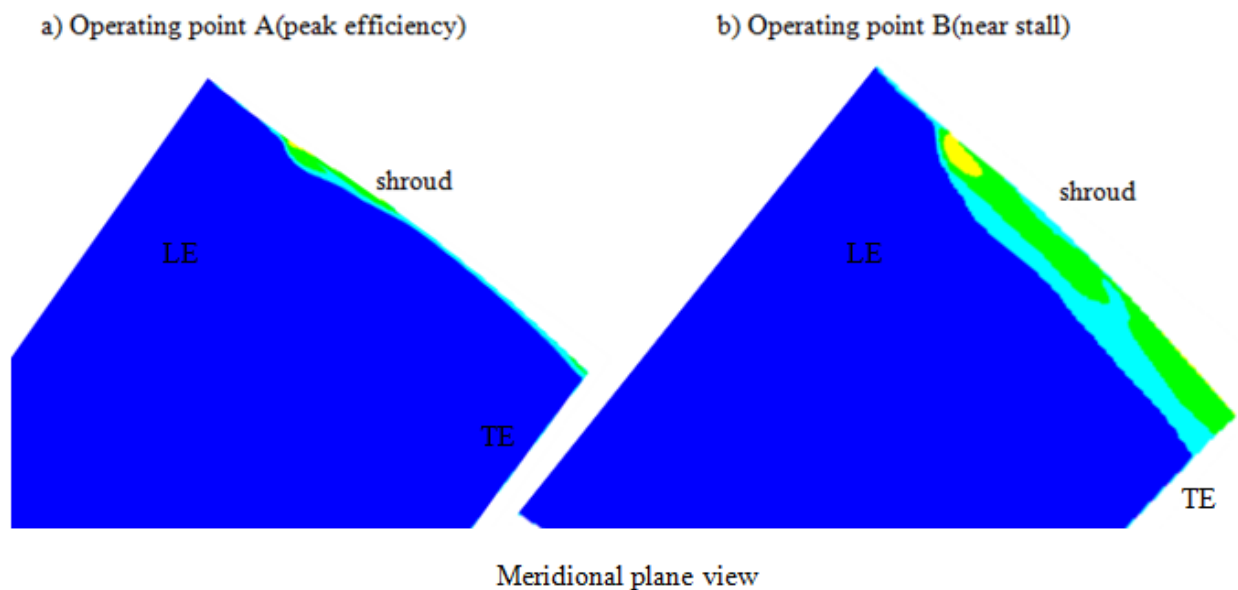


Figure 5. 14 - Entropy contours at meridional plane view at the middle(50% pitch)

blade tip vortex is scattered and large in size. Also the interactions with the shock wave are stronger at near stall condition compared to the peak efficiency condition. This was also indicated in the work of Chima(Chima, 2006) in which he also found out that entropy rises across the rotor blade passage at the tip section of the blade on the near stall operating condition compressor configuration.

The rotor tip gap leakage vortex shedding streamlines for the two operating points A and B is shown in Figure 5.15. On operating point A, it is observed that only the forward portion of the tip leakage flow emerges to form the leakage flow vortex core. There is an interaction that can be observed between the vortex shedding core and shock wave at the leading edge side of the tip gap. The interaction is not strong and slightly alters the shape and trajectory of the vortex. The trajectory of the vortex is parallel to the axial flow direction and the shock wave has a minor impact on the tip vortex trajectory. In Figure 5.15b, for the near stall operating point B, it is again observed that only forward portion of the tip leakage flow emerges to form the leakage flow vortex core, which is now located further ahead compared with the operating point A condition. At near stall condition there is high blade loading in which larger pressure differences between the pressure side surface and the suction side surface of the rotor blade near the tip. The tip vortex is larger in size compared to the peak efficiency design condition. The vortex interacts with the shock wave closer to the rotor suction surface. The interaction is strong and impacts the shape and trajectory of the vortex. The vortex is now perpendicular to the axial flow direction. This agrees with the stall inception conducted by Hoying et al. (A.D. Hoying et al.(1998)) on their vortex kinematic analysis when the trajectory of the tip gap clearance vortex revealed perpendicular to the axial flow direction.

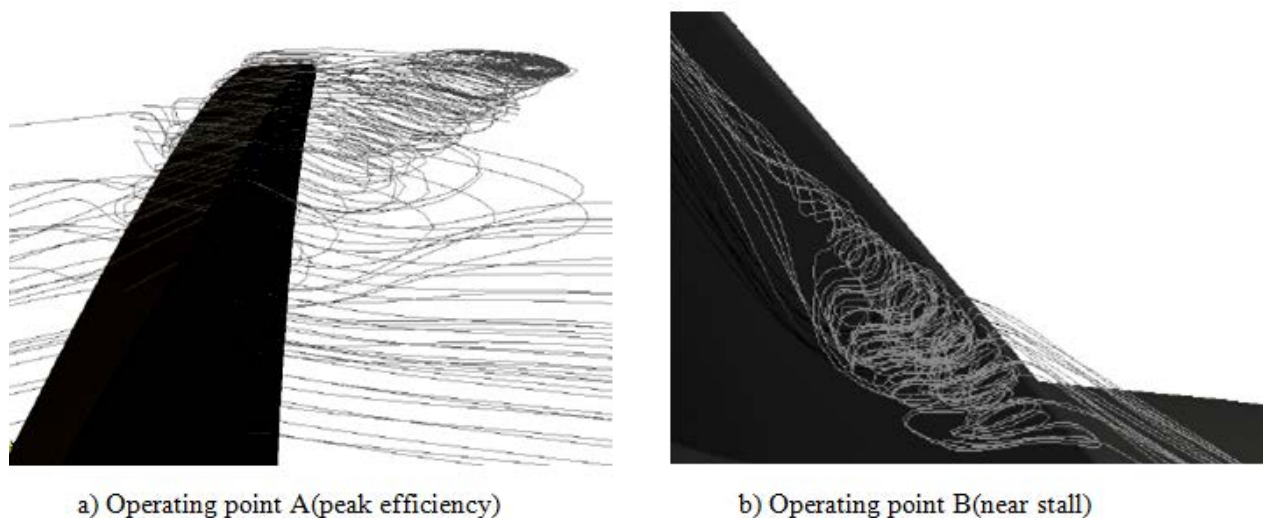


Figure 5. 15 - Tip gap leakage vortex shedding streamlines

There is a low momentum flow in the boundary layer which is subjected to the pressure rise across the shock wave during shock wave-boundary layer interaction. The abrupt pressure rise acts as a high adverse

pressure gradient on the boundary layer and when the shock wave is strong enough, the pressure increase across boundaries will cause the boundary layer separation, due to this, induce flow separation possibility of the shock boundary layer interactions will be assessed. This might occur on locations where the shock wave interacts with the tip clearance leakage flow vortex or at the shroud casing surface. Examining the rotor tip gap clearance flow stream lines at near stall condition shown in Figure 5.15b, it can be observed in this region that no flow separation occurs. Theoretically at the shroud casing surface, tip clearance vortex reversed flow occurs which eliminates the possibility of the flow separation.

In-stall operating condition at point C was analyzed through velocity vectors near the rotor blade tip leading edge as shown in Figure 5.16. This operating condition shows a flow spillage that occurs over at the rotor tip leading edge which can be observed. This observation is in agreement also with Vo et al's (D.H. Vo et al.) work which also showed forward spillage of the tip clearance vortex flow during stall inception. The rapid growth of the tip leakage vortex over tip gap causes some reversed flow.

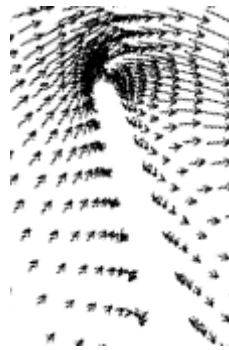


Figure 5. 16 - Operating point C(in-stall condition) velocity vectors near leading edge

CHAPTER 6: CONCLUSION AND FUTURE WORK

The flow investigation on the onset of stall and choke on the NASA Rotor 67 compressor rotor has been made with the open source CFD software OpenFOAM. A density based algorithm supported by a Godunov scheme discretized the average Navier-Stokes equations, which were the main model of the numerical simulation. The tip-gap region geometry is a very important parameter on turbomachinery(Tang, 2004) and so, different operating point conditions on the compressor performance map were thoroughly studied on this region.

The motivation for this work had two components: First, flow investigation of stall and choked. Second, is the author's desire to learn and apply fluid dynamics in CFD tool. As a result, a big range of subjects were learned and mentions here, from pure mathematics to the fundamentals of fluid dynamics and engineering applications. These all were thought to be presented with such a structure that the answers to the following sought questions from the start: How does the rotor blade tip clearance flow affects shock wave during interactions? Does shock boundary layer leading to shock waves causes flow separation? What is the possible behavior of both the shock wave and the rotor tip clearance flow?

To answer the preceding questions, one conclusion can be drawn.

- Compressor stall could be detected by monitoring global flow characteristics such as its flow coefficient fluctuation(mass flow rate) and the pressure coefficient(flow pressures). By exploring the flow field as the compressor throttles towards stall, the following flow phenomena were observed. Upstream from the rotor blade leading edge, the shock wave moves further and becomes stronger. At near stall conditions, the rotor tip clearance flow vortex grows larger and stronger due to the high blade loading. The shock wave and the rotor blade tip gap vortex interactions also become more unsteady and stronger. These create disturbance and those interactions alter the trajectory of the rotor blade tip vortex which in turn generates a low momentum area near the adjacent rotor blade tip leading edge that causes the flow spillage on the surrounding regions. Therefore, the interactions between the rotor blade tip vortex and the shock wave are believed to be the main reason behind the stall inception in the compressor. Other published research were consistent with these findings regarding compressor stall.

Other conclusion that could be drawn along the course of the work were the following:

- Regarding flow structures across rotor, it is clear that the hyperbolic system is being well resolved and did not need many cells base on the unstructured mesh applied(*snappyHexMesh*) to reach good accuracy based on successful convergence and in agreement result with the experimental data.

- The flow structure that was known to exist in anticipation with other research results was captured by the HLLC-tip gap vortex trailing edge vortex and shock. This assured that the solver chosen was robust capturing the implementation of the numerical methods.
- There were huge challenges on learning OpenFOAM and difficulties on extracting numerical data but essentially, all that is needed is patience, persistence and hard work.

For the future work, a similar work but focusing on choke phenomena as a sole subject of the investigation will be worthy to explore since results on choke instabilities on this work is not fully covered.

REFERENCES

- A. Andrea, M.-S. L., and L. A. Povinelli. (1993). "Multigrid time-accurate integration of navier-stokes equations," Tech. Rep. NASA TM 106373, NASA, 1993.
- A. Harten, P. D. L., and B. van Leer. (1983). "On Upstream Differencing and Godunov-Type Schemes for Hyperbolic Conservation Laws," SIAM Review, vol. 25, no. 1, pp. 35-61.
- Adamczyk, J. J. (1985). "Model Equation for Simulating Flows in Multistage Turbomachinery," ASME Paper 85-GT-226.
- Adamczyk, J. J., Celestina, M. L., and Grietzer, E. M. (1993). "The Role of Tip Clearance in High-Speed Fan Stall," Transactions of the ASME, Vol. 115.
- Adamczyk, J. J., Mulac, R. A., & Celestina, M. L. (1986). "A Model for Closing the Inviscid Form of the Average-Passage Equation System," ASME Paper 86-GT-227.
- al., A. J. e. (1981). "Numerical solution of the euler equations by finite volume methods using runge-kutta time-stepping schemes," AIAA 14th Fluid and Plasma Dynamic Conference, 1981.
- al., G. e. (2005). "Computation of turbulent flows around rotating bodies using unstructured grids," Ankara International Aerospace Conference, no. AIAC-2005-078, 2005.
- al., O. B. e. (2011). "Density based navier stokes solver for transonic flows," OpenFoam 6th workshop, 2011.
- Anderson Jr., D. (1984). Fundamentals of Aerodynamics. McGraw-Hill.
- Anthony J. Strazisar, M. D. H., Jerry R. Wood, Kenneth L. Suder. (1989). "Laser Anemometer Measurements in a Transonic Axial-Flow Fan Rotor", NASA Technical Paper 2879.
- Bakker, A. (2002). Lecture 11 - Boundary Layers and Separation.
- Beam, R., and Warming, R. (1978). "An Implicit Factored Scheme for the Compressible Navier-Stokes Equations," AIAA Journal, Vol.16, No. 4, pp. 393-402.
- Blazek, J. (2001). Computational Fluid Dynamics: Principles and Applications. Elsevier, 2001.
- Bonnaure, L. P. (1991). Modeling High Speed Multistage Compressor Stability, Master's Thesis, Massachusetts Institute of Technology.
- Borm, O. (2013). "turbovtk python scripts." <http://sourceforge.net/projects/turbopost/>, (Consulted 09.03.13).
- Briley, W. R., and Macdonald, H. (1984). "Three dimensional viscous flows with large secondary velocity," Journal of Fluid Mechanics, Vol.144, pp. 47-77.
- Chima, R. V. (1987). "Explicit Multigrid Algorithm for Quasi-Three-Dimensional Viscous Flows in Turbomachinery," Journal of Propulsion Power, Vol. 3, No. 5, pp. 397-405,.
- Chima, R. V. (1992). "Viscous Three-Dimensional Calculations of Transonic Fan Performance," in CFD Techniques for Propulsion Applications, AGARD Conference Proceedings, No. CP-510, AGARD, Neuilly-Sur-Seine, France, pp. 21-1 to 21-19.
- Chima, R. V. (1996). "Calculation of Tip Clearance Effects in a Transonic Compressor Rotor," NASA TM 107216.
- Chima, R. V. (2006). "A Three-Dimensional Unsteady CFD Model of Compressor Stability," ASME GT2006-90040, proceedings of the ASME Turbo Expo 2006, Barcelona, Spain, May 8-11, 2006.
- David Japikse, N. C. B. (1997). Introduction to Turbomachinery.
- Davidson, L. (2006). "Turbulence modelling," tech. rep., Chalmers University of Technology, 2006.
- Davis, R. L., and Yao, J. (2005). "Prediction of Compressor Stage Performance from Choke Through Stall," AIAA 2005-1005, 43rd AIAA Aerospace Sciences Meeting, Reno, NV.
- de Jager, B. (1995). "Rotating Stall and Surge Control", Proceedings of the 34th Conference on Decision & Control, New Orleans, LA
- Denton, J. D. (1990). "The Calculation of Three Dimensional Viscous Flow through Multistage Turbomachines," ASME Paper 90-GT-19.
- Dhingra, M., Neumeiery, Prasad, J.V.R, and Shinx, H. (2003). "Stall and Surge Precursors in Axial Compressors", AIAA 2003-4425, 39th AIAA/ASME/SAE/ASEE Joint Propulsion Conference and Exhibit, Huntsville, Alabama.
- E. Toro, M. S., and W. Speares. (1994). Restoration of the contact surface in the HLL-Riemann solver, Shock Waves, vol. 4, pp. 25-34.
- Eisfeld, B. (2006). "Computation of complex compressible aerodynamic flows with a reynolds stress turbulence model," Int. Conference on Boundary and Interior Layers, 2006.
- Frisch, U. (1995). Turbulence. The legacy of A. N. Kolmogorov. Cambridge University Press, 1995.

- Giljarhus, K. E. (2018). Computation Fluid Dynamic, Course Compendium, University of Stavanger.
- Greenshields, C. J. (2017). OpenFOAM, The OpenFOAM Foundation, User Guide version 5.0, <http://openfoam.org>.
- Hah, C., Bergner, J., and Schiffer, H.P. (2006). "Short Length-Scale Rotating Stall Inception in a Transonic Axial Compressor – Criteria and Mechanism", Proceedings of GT2006, ASME Turbo Expo 2006, GT2006-90045.
- Hah, C., Rabe, D. C., and Wadia, A. R. (2004). "Role of Tip-Leakage Vortices and Passage Shock in Stall Inception in a Swept Transonic Compressor Rotor", ASME Paper GT2004-53867.
- Haixin, C., Xudong, H. and Song, F. (2006). "CFD Investigation on stall Mechanism and Casing Treatment of a Transonic Compressor", AIAA-2006-4799, 42nd AIAA/ASME/SAE/ASEE Joint Propulsion Conference and Exhibit, Sacramento, California.
- Hathaway, M. D. (1987). "Three Dimensional Flows in Multistage Compressors," NASA N92-70923, pp. 21-34.
- He, L. a. I., J. O. (1997). "Computations of Blade Row Stall Inception in Transonic Flows", ISABE Proceedings, pp. 697-707.
- Hoying, D. A., Tan, C. S., Vo, H. D., and Greitzer, E. M. (1998). "Role of Blade Passage Flow Structures in Axial Compress Rotating Stall Inception," Journal of Turbomachinery, Vol. 121, pp. 735-742, 1998.
- <https://www.blender.org/>.
- <https://www.salome-platform.org/>.
- Indue, M., Kuroumaru, M., Iwamoto, T., and Ando, Y. (1991). "Detection of a Rotating Stall Precursor in Isolated Axial Flow Compressor Rotors", Journal of Turbomachinery Vol.113, No. 2, pp. 281-289.
- Ingram, G. (2009). Basic Concepts in Turbomachinery.
- Jameson, A. (1983). "Transonic flow calculation," Tech. Rep. MAE Report 1651, Princeton University, 1983.
- Jameson, A. (1991). "Time dependent calculations using multigrid, with applications to unsteady flows past airfoils and wings," AIAA 10th Computational Fluid Dynamics Conference, no. AIAA 91-1596, 1991.
- Jones, W. P., and Launder, B. E. (1972). "The Prediction of Laminarization with a Two-Equation Model of Turbulence," International Journal of Heat and Mass Transfer, Vol. 15, pp. 301-313.
- King, D. A. J. a. L. S. (1985). "Mathematically simple turbulence closure model for attached and separated turbulent boundary layers," AIAA Journal, vol. 23, no. 11, pp. 1684{1692, 1985.
- Landmann, B. (2008). A parallel discontinuous Galerkin code for the Navier-Stokes and Reynolds-averaged Navier-Stokes equations. PhD thesis, Universitat Stuttgart, 2008.
- Lawless, P. B., Kim, K. H., and Fleeter, S. (1994). "Characterization of Abrupt Rotating Stall Initiation in an Axial Flow Compressor", Journal of Propulsion and Power, Vol.10, No. 5, pp. 709-715.
- Leer, B. V. (1977). "Towards the ultimate conservative difference scheme. iv. a new approach to numerical convection," J. Comput. Phys., 1977.
- MacCormack, R. W. (1969). "The Effect of Viscosity in Hypervelocity Impact Cratering," AIAA Paper, 69-35.
- Malalasekera, H. K. V. a. W. (1995). An Introductcion to Computational Fluid Dynamics, The Finite Volume Method, 1995.
- McCaughan, F. E. (1989a). Application of Bifurcation Theory to Axial Flow Compressor Instability," Journal of Turbomachinery, No. 111, pp. 426-433.
- McCaughan, F. E. (1989b). "Numerical Results for Axial Flow Compressor Instability," Journal of Turbomachinery, No. 111, pp. 434-441.
- McDonough, J. M. (2007). Introductory Lectures on Turbulence. Departments of Mechanical Engineering and Mathematics, University of Kentucky, 2007.
- Menter, F. R. (1992). "Improved two-equation k-omega turbulence models for aerodynamic flows," NASA TM 103975, 1992.
- Menter, F. R. (1993). "Zonal two equation k-omega turbulence models for aerodynamics flows," American Institute of Aeronautics and Astronautics, 1993.
- Menter, F. R. (1994). "Two-Equation Eddy-Viscosity Turbulence Models for Engineering Applications," AIAA Journal, Vol. 32, No. 8, pp. 1598-1605.
- Morton, R. D. R. a. K. W. (1967). Difference Methods for Initial Value Problems. Wiley-Interscience, 2nd ed., 1967.
- Niazi, S., Stein, A., and Sankar, L. N. (2000). "Numerical Study of Surge and Stall Alleviation in a High-Speed Transonic Fan Rotor", AIAA Paper 2000-0225.
- Open Source CFD International Conference, Development of a Generalized Grid Interface for Turbomachinery Simulations with OpenFOAM, 2008.
- Pampreen, R. C. (1993). Compressor Surge and Stall. *Concepts ETI, Inc., Norwich, Vermont*.

- Piomelli, U. a. C., J.R. (1996). "Large-Eddy Simulations: Theory and Applications," in Henningson, D., Hallbäck, M., Alfredsson, H. and Johansson, A., Transition and Turbulence Modeling, Dordrecht, Kluwer Academic Publishers, pp. 269-336.
- Pirkel, L. (2016). CFD project? An OpenFOAM? Yes, please!, <https://www.linkedin.com/pulse/cfd-project-openfoam-yes-please-lubos-pirkel/>.
- R. C. Swanson, E. T., and J. A. White. (1991). "An effective multigrid method for high-speed flows," Tech. Rep. ICASE Report No. 91-56, NASA, 1991.
- Rai, M. M. "Three Dimensional Navier Stokes Simulation of Turbine Rotor-Stator Interaction; Part I- Methodology," AIAA Paper 87-2058.
- Reis, A. J. F. (2013). Validation of NASA Rotor 67 with OpenFOAM's Transonic Density-Based solver, PhD thesis, Universidade Nova de Lisboa, 2013.
- Royce, R. The Jet Engine. Rolls Royce, -.
- Rumsey, P. R. S. a. C. L. (2007). "Effective in flow conditions for turbulence models in aerodynamic calculations," AIAA Journal, vol. 45, no. 10, pp. 2544-2553, 2007.
- Saxer, A. P., and Giles, M. B. (1994). "Predictions of Three-Dimensional Steady and Unsteady Inviscid Transonic Stator/Rotor Interaction with Inlet Radial Temperature Nonuniformity," Journal of Turbomachinery, Vol. 116, pp. 347-357.
- Schmitt, F. (2007). "About boussinesq's turbulent viscosity hypothesis: historical remarks and a direct evaluation of its validity," Comptes Rendus Mecanique, vol. 335, pp. 617-627, 2007.
- Sebghati, J. M. (1992). Monitoring Axial Flow Compressor Stall and Surge, Master's Thesis, The University of Tennessee, Knoxville.
- Spalart, P. R., and Allmaras, S. R. (1994). "A One-Equation Turbulence Model for Aerodynamic Flows," La Rech. Aérospatiale, Vol. 1, pp. 5-21.
- Suder, K. L., Hathaway, M. D., Thorp, S. A., Strazisar, A. J., and Bright, M. M. (2001). "Compressor Stability Enhancement Using Discrete Tip Injection," ASME Journal of Turbomachinery, Vol. 123, pp. 14-23.
- Tang, G. (2004). Measurements of the Tip-gap Turbulent Flow Structure in a Low-speed Compressor Cascade. PhD thesis, Faculty of the Virginia Polytechnic Institute and State University, 2004.
- Toro, E. F. (1999). Riemann Solvers and Numerical Methods for Fluid Dynamics. Springer, 2nd ed., 1999.
- Venkatakrishnan, V. (1995). "Convergence to steady state solutions of the euler equations on unstructured grids with limiters," J. Comput. Phys., vol. 118, pp. 120-130, 1995.
- Vo, H. D., Tan, C. S., and Greitzer, E. M. "Criteria for Spike Initiated Rotating Stall", ASME Paper GT2005-68374.
- Wendroff, P. D. L. a. B. (1964). "Difference schemes for hyperbolic equations with high order of accuracy," Communications on Pure and Applied Mathematics, vol. 17, no. 3, pp. 381-398, 1964.
- White, F. M. (1994). Fluid Mechanics. McGraw-Hill.
- Wilcox, D. C. (1988). "Reassessment of the Scale-Determining Equation for Advanced Turbulence Models," AIAA Journal, Vol. 26, No. 11, pp. 1299-1310.
- William, K. G. "Lectures in turbulence for the 21st century".
- Wyss, M. L., Chima, R. V. "Averaging Techniques for Steady and Unsteady Calculations of a Transonic Fan Stage," AIAA Paper 93-3065.
- Zaki, M. A. (2009). Physics Based Modeling of Axial Compressor Stall, PhD thesis, Georgia Institute of Technology, 2009.

APPENDIX 1 - SNAPPYHEXMESH FILE DICTIONARY

```

snappyHexMeshDict-on appendix - Notepad2
File Edit View Settings ?
1 /*-----*- C++ -*-*/
2 |
3 | ===== |
4 | \ \ \ \ \ | F i e l d | openFOAM: The open source CFD Toolbox
5 | \ \ \ \ \ | O p e r a t i o n | Version: 5
6 | \ \ \ \ \ | A n d | web: www.OpenFOAM.org
7 | \ \ \ \ \ | M a n i p u l a t i o n |
8 |-----*/
9 FoamFile
10 {
11     version      2.0;
12     format       ascii;
13     class        dictionary;
14     object       snappyHexMeshDict;
15 }
16 // ***** //
17 castellatedMesh true;
18 snap           true;
19 addLayers      false;//false
20
21 geometry
22 {
23     Rotor_INLET
24     {
25         type      triSurfaceMesh;
26         file      "Rotor_INLET.stl";
27     }
28
29     Rotor_OUTLET
30     {
31         type      triSurfaceMesh;
32         file      "Rotor_OUTLET.stl";
33     }
34
35     Rotor_HUB
36     {
37         type      triSurfaceMesh;
38         file      "Rotor_HUB.stl";
39     }
40
41     Rotor_BLADE
42     {
43         type      triSurfaceMesh;
44         file      "Rotor_BLADE.stl";
45     }
46
47     Rotor_SHROUD
48     {
49         type      triSurfaceMesh;
50         file      "Rotor_SHROUD.stl";
51     }
52
53     Rotor_SIDEFACE1
54     {
55         type      triSurfaceMesh;

```

```
56     file      "Rotor_SIDEFACE1.stl";
57 }
58
59 Rotor_SIDEFACE2
60 {
61     type      triSurfaceMesh;
62     file      "Rotor_SIDEFACE2.stl";
63 }
64
65 Rotor_VOLUMESTL.stl
66 {
67     type      triSurfaceMesh;
68
69     regions
70     {
71         Rotor_INLET {name Rotor_INLET;}
72         Rotor_OUTLET {name Rotor_OUTLET;}
73         Rotor_HUB {name Rotor_HUB;}
74         Rotor_BLADE {name Rotor_BLADE;}
75         Rotor_SHROUD {name Rotor_SHROUD;}
76         Rotor_SIDEFACE1 {name Rotor_SIDEFACE1;}
77         Rotor_SIDEFACE2 {name Rotor_SIDEFACE2;}
78     }
79 }
80 };
81
82 castellatedMeshControls
83 {
84     maxLocalCells 2000000;
85     maxGlobalCells 4000000;
86     minRefinementCells 0;
87     maxLoadUnbalance 0.10;
88     nCellsBetweenLevels 3;
89
90     features
91     (
92     {
93         file      "Rotor_BLADE.eMesh";
94         levels    ((0.002 4));
95     }
96     {
97         file      "Rotor_SIDEFACE1.eMesh";
98         levels    ((0.002 2));
99     }
100    {
101        file      "Rotor_SIDEFACE2.eMesh";
102        levels    ((0.002 2));
103    }
104    {
105        file      "Rotor_INLET.eMesh";
106        levels    ((0.002 2));
107    }
108    {
109        file      "Rotor_OUTLET.eMesh";
```



```
110     levels      ((0.002 2));
111   }
112   {
113     file        "ROTOR_LE_TE.obj";
114     levels      ((0.004 2));
115   }
116 );
117
118 refinementSurfaces
119 {
120   Rotor_INLET
121   {
122     level       (2 2);
123     patchInfo
124     {
125       type patch;
126     }
127   }
128
129   Rotor_OUTLET
130   {
131     level       (2 2);
132     patchInfo
133     {
134       type patch;
135     }
136   }
137
138   Rotor_SHROUD
139   {
140     level       (2 2);
141     patchInfo
142     {
143       type wall;
144     }
145   }
146
147   Rotor_SIDEFACE1
148   {
149     level       (2 2);
150     patchInfo
151     {
152       type patch;
153     }
154   }
155
156   Rotor_SIDEFACE2
157   {
158     level       (2 2);
159     patchInfo
```

```
164     {
165         type patch;
166     }
167 }
168 }
169 }
170
171 Rotor_BLADE
172 {
173     level      (2 2);
174     patchInfo
175     {
176         type wall;
177         ingroups (movingwalls);
178     }
179 }
180
181 Rotor_HUB
182 {
183     level      (2 2);
184     patchInfo
185     {
186         type wall;
187         ingroups (movingwalls);
188     }
189 }
190
191
192
193
194 }
195 }
196
197 resolveFeatureAngle 38;
198
199 refinementRegions
200 {
201     Rotor_VOLUMESTL.stl
202     {
203         levels ((0 2));
204         mode inside;
205     }
206 }
207 }
208
209 locationInMesh (0.10 0.008 -0.02);
210
211 allowFreestandingZoneFaces false; //false
212 }
213
214 snapControls
215 {
216     nSmoothPatch 3;
217     tolerance 1.0;
218     nSolveIter 200;//100
```

```
219     nRelaxIter 5;
220     nFeatureSnapIter 10;
221
222     //- Detect (geometric) features by sampling the surface
223     implicitFeatureSnap false;
224
225     //- Use castellatedMeshControls::features
226     explicitFeatureSnap true;
227
228     //- Detect features between multiple surfaces
229     // (only for explicitFeatureSnap, default = false)
230     multiRegionFeatureSnap false;
231 }
232
233 addLayersControls
234 {
235     relativeSizes false; //was true
236     layers
237     {
238     }
239     expansionRatio 1.0;
240     finalLayerThickness 0.3;
241     minThickness 0.1;
242     nGrow 0;
243     featureAngle 30;
244     nRelaxIter 3;
245     nSmoothSurfaceNormals 1;
246     nSmoothNormals 3;
247     nSmoothThickness 10;
248     maxFaceThicknessRatio 0.5;
249     maxThicknessToMedialRatio 0.3;
250     minMedianAxisAngle 90;
251     nBufferCellsNOExtrude 0;
252     nLayerIter 50;
253 }
254
255 meshQualityControls
256 {
257     maxNonOrtho 65;
258
259     maxBoundarySkewness 20; //was 20
260     maxInternalSkewness 4;
261
262     maxConcave 80;
263     minVol 1e-13;
264     minTetQuality -1;
265     minArea -1;
266     minTwist 0.01;
267     minDeterminant 0.001;
268     minFaceWeight 0.05;
269     minVolRatio 0.01;
270     minTriangleTwist -1;
271     nSmoothScale 4;
272     errorReduction 0.75;
273     relaxed
```

```
274 {
275     maxNonOrtho 75;
276 }
277 }
278
279 mergeTolerance 1e-6;
280
281 // *****
282
```

Ln 190 : 282 Col 10 : 79 Sel 0 5.67 KB ANSI LF INS Default Text

Above, is the snappyHexMesh file dictionary for creating the unstructured meshing of the rotor passage domain using shappyHexMesh. Please refer to the following document, A Comprehensive Tour of snappyHexMesh, 7th OpenFOAM Workshop, 25 June 2012 (<http://www.engys.eu>) for the comprehensive explanation of the parameters involved.

APPENDIX 2 - SNAPPYHEXMESH RUN

```

AVANT-02@HP-LAPTOP-02 MINGW64 OpenFOAM-5.x ~/blueCFD/ofuser-of5/run/sonicDyMFoam/Rotor67Project/TheCaseNasaRotor
$ Created temporary 'TheCaseNasaRotor.foam'
$ SnappyHexMesh
/*-----*/
|
|  =====
|  \      /  F ield      | OpenFOAM: The Open Source CFD Toolbox
|   \    /  O peration  | Version: 5.x
|    \  /  A nd         | Web: www.OpenFOAM.org
|     \/  M anipulation |
|
|-----|
/*-----*/
|
|  Windows 32 and 64 bit porting by blueCAPE: http://www.bluecape.com.pt
|  Based on Windows porting (2.0.x v4) by Symscape: http://www.symscape.com
|
|-----|
/*-----*/
Build : 5.x-7ac8a133a3b0
Exec  : C:/PROGRA~1/BLUECF~1/OpenFOAM-5.x/platforms/mingw_w64GccDPInt32Opt/bin/SnappyHexMesh.exe
Date  : Apr 17 2018
Time  : 21:31:58
Host  : "HP-LAPTOP-02"
PID   : 104276
I/O   : uncollated
Case  : C:/PROGRA~1/BLUECF~1/ofuser-of5/run/sonicDyMFoam/Rotor67Project/TheCaseNasaRotor
nProcs : 1
SigFpe : Enabling floating point exception trapping (FOAM_SIGFPE).
fileModificationChecking : Monitoring run-time modified files using timeStampMaster (fileModificationSkew 10)
allowSystemOperations : Allowing user-supplied system call operations

// ***** //
Create time

--> FOAM Warning :
    From function entry::getKeyword(keyType&, Istream&)
    in file db/dictionary/entry/entryIO.C at line 144
    Reading C:/PROGRA~1/BLUECF~1/ofuser-of5/run/sonicDyMFoam/Rotor67Project/TheCaseNasaRotor/system/controlDict
    found on line 32 the punctuation token '/'
    expected either } or EOF
Create mesh for time = 0

Read mesh in = 0.44 s

Overall mesh bounding box : (0.079356 -0.104702 -0.037225) (0.263776 0.116056 0.132725)
Relative tolerance       : 1e-006
Absolute matching distance : 3.34108e-007

Reading refinement surfaces.
Read refinement surfaces in = 0.82 s

Reading refinement shells.
Refinement level 2 for all cells inside Rotor_VOLUMESTL.stl
Read refinement shells in = 0.221 s

Setting refinement level of surface to be consistent with shells.
Checked shell refinement in = 0 s

```

```
Determining initial surface intersections
-----
Edge intersection testing:
  Number of edges      : 174283
  Number of edges to retest : 174283
  Number of intersected edges : 6118
Calculated surface intersections in = 0.61 s

Initial mesh : cells:56610 faces:174283 points:61180
Cells per refinement level:
  0 56610

Adding patches for surface regions
-----
Patch Type          Region
-----
Rotor_INLET:
1  patch            Rotor_INLET
Rotor_OUTLET:
2  patch            Rotor_OUTLET
Rotor_HUB:
3  wall             Rotor_HUB
Rotor_BLADE:
4  wall             Rotor_BLADE
Rotor_SHROUD:
5  wall             Rotor_SHROUD
Rotor_SIDEFACE1:
6  patch            Rotor_SIDEFACE1
Rotor_SIDEFACE2:
7  patch            Rotor_SIDEFACE2

Added patches in = 0.006 s

Selecting decompositionMethod none
Layer thickness specified as final layer and expansion ratio.

Refinement phase
-----
Found point (0.1 0.008 -0.02) in cell 50768 on processor 0
```

```

Removing 22776 straight edge points ...

Edge intersection testing:
  Number of edges      : 1953390
  Number of edges to retest : 126253
  Number of intersected edges : 83354

Undo iteration 0
-----
Checking faces in error :
  non-orthogonality > 65 degrees           : 0
  faces with face pyramid volume < 1e-013  : 0
  faces with face-decomposition tet quality < -1 : 0
  faces with concavity > 80 degrees        : 0
  faces with skewness > 4 (internal) or 20 (boundary) : 0
  faces with interpolation weights (0..1) < 0.05 : 0
  faces with volume ratio of neighbour cells < 0.01 : 0
  faces with face twist < 0.01             : 0
  faces on cells with determinant < 0.001  : 0

Removing zero-sized patches:
  defaultFaces type patch at position 0

Snapped mesh : cells:641232 faces:1953390 points:684566
Cells per refinement level:
  0 0
  1 0
  2 564950
  3 15619
  4 60663
Writing mesh to time 0.002
Wrote mesh in = 24.622 s.
Mesh snapped in = 307.565 s.
Checking final mesh ...
Checking faces in error :
  non-orthogonality > 65 degrees           : 0
  faces with face pyramid volume < 1e-013  : 0
  faces with face-decomposition tet quality < -1 : 0
  faces with concavity > 80 degrees        : 0
  faces with skewness > 4 (internal) or 20 (boundary) : 0
  faces with interpolation weights (0..1) < 0.05 : 0
  faces with volume ratio of neighbour cells < 0.01 : 0
  faces with face twist < 0.01             : 0
  faces on cells with determinant < 0.001  : 0
Finished meshing without any errors
Finished meshing in = 442.7 s.
End

[2]- Exit 1                paraFoam -builtin -minpath -builtin -minpath
AVANT-02@HP-LAPTOP-02 MINGW64 OpenFOAM-5.x ~/blueCFD/ofuser-of5/run/sonicDyMFoam/Rotor67Project/TheCaseNasaRotor

```

Shown above is the successful run of the unstructured meshing set up of the computational domain. It showed *Finished meshing without any errors* which is very self explanatory. Please note that this is only a portion of the entire report, emphasizing the successful result.


```

13 23
14 24
15 715
Checking topology...
  boundary definition OK.
  cell to face addressing OK.
  Point usage OK.
  Upper triangular ordering OK.
  Face vertices OK.
  Number of regions: 1 (OK).

Checking patch topology for multiply connected surfaces...
  Patch      Faces    Points    Surface topology
  defaultFaces  0        0        ok (empty)
  Rotor_INLET  5389     5616    ok (non-closed singly connected)
  Rotor_OUTLET 4167     4353    ok (non-closed singly connected)
  Rotor_HUB    9793     10875   ok (non-closed singly connected)
  Rotor_BLADE 41944    43120   ok (non-closed singly connected)
  Rotor_SHROUD 16810    17530   ok (non-closed singly connected)
  Rotor_SIDEFACE1 26422   26808   ok (non-closed singly connected)
  Rotor_SIDEFACE2 26953   27352   ok (non-closed singly connected)

Checking geometry...
  Overall domain bounding box (0.0880785 -0.0936638 -0.0297272) (0.255053 0.105019 0.125227)
  Mesh has 3 geometric (non-empty/wedge) directions (1 1 1)
  Mesh has 3 solution (non-empty) directions (1 1 1)
  Boundary openness (3.0751e-016 -1.46679e-015 -1.86985e-016) OK.
  Max cell openness = 2.07825e-016 OK.
  Max aspect ratio = 1.02095 OK.
  Minimum face area = 9.53464e-008. Maximum face area = 1.55875e-006. Face area magnitudes OK.
  Min volume = 2.97862e-011. Max volume = 1.91197e-009. Total volume = 0.00108444. Cell volumes OK.
  Mesh non-orthogonality Max: 25.6738 average: 3.24844
  Non-orthogonality check OK.
  Face pyramids OK.
  Max skewness = 1.00322 OK.
  Coupled point location match (average 0) OK.

Mesh OK.

--> FOAM warning :
  From function virtual Foam::polyMesh::readUpdateState Foam::polyMesh::readUpdate()
  in file meshes/polyMesh/polyMeshIO.C at line 209
  unexpected consequences. Proceed with care.
Time = 0.002

Mesh stats
  points:          684566
  faces:           1953390
  internal faces:  1870025
  cells:           641232
  faces per cell:  5.96261
  boundary patches: 7
  point zones:    0
  face zones:     0
  cell zones:     0

Overall number of cells of each type:
  hexahedra:      598525
  prisms:         13209
  wedges:         0
  pyramids:       0
  tet wedges:     162
  tetrahedra:     2
  polyhedra:      29334
Breakdown of polyhedra by number of faces:

```

```

      faces  number of cells
      4     12260
      5     8862
      6     3134
      7     185
      8     97
      9     2747
     10     50
     11     37
     12    1232
     13     7
     14    11
     15    712

Checking topology...
  Boundary definition OK.
  Cell to face addressing OK.
  Point usage OK.
  Upper triangular ordering OK.
  Face vertices OK.
  Number of regions: 1 (OK).

Checking patch topology for multiply connected surfaces...
      Patch      Faces    Points    Surface topology
  Rotor_INLET   5379     5486    ok (non-closed singly connected)
  Rotor_OUTLET  4165     4251    ok (non-closed singly connected)
  Rotor_HUB     7137     8618    ok (non-closed singly connected)
  Rotor_BLADE   24520    30147   ok (non-closed singly connected)
  Rotor_SHROUD  12881    14272   ok (non-closed singly connected)
  Rotor_SIDEFACE1 14712    17805   ok (non-closed singly connected)
  Rotor_SIDEFACE2 14571    18513   ok (non-closed singly connected)

Checking geometry...
  Overall domain bounding box (0.0877807 -0.0946282 -0.0295) (0.255392 0.106009 0.125)
  Mesh has 3 geometric (non-empty/wedge) directions (1 1 1)
  Mesh has 3 solution (non-empty) directions (1 1 1)
  Boundary openness (-1.69945e-016 2.17399e-015 -7.1783e-017) OK.
  Max cell openness = 2.8233e-016 OK.
  Max aspect ratio = 7.50665 OK.
  Minimum face area = 2.95511e-009. Maximum face area = 4.17563e-006. Face area magnitudes OK.
  Min volume = 3.46562e-012. Max volume = 3.76073e-009. Total volume = 0.00108172. Cell volumes OK.
  Mesh non-orthogonality Max: 64.8489 average: 5.61866
  Non-orthogonality check OK.
  Face pyramids OK.
  Max skewness = 3.08125 OK.
  Coupled point location match (average 0) OK.

Mesh OK.

End

AVANT-02@HP-LAPTOP-02 MINGW64 OpenFOAM-5.x ~/blueCFD/ofuser-of5/run/sonicDyMFoam/Rotor67Project/TheCaseNasaRotor
$ parafoam &

```

Shown above is the quality reports of the result of check Mesh. It gives the output *Mesh OK* which means every mesh quality test is passed. *Checking patch topology* informs the name of the boundaries and *Checking geometry* informs about skewness, non-orthogonality, aspect ratio, etc, which are all intended to mesh quality. *Mesh stats* on the other hand, informs about the number of points, cells and boundaries while *Mesh topology* signifies if mesh are well connected.

APPENDIX 4 - PORTION OF RHOPIMPLE DYMFoam SOLVER OUTPUT

```

Courant Number mean: 0.0030068 max: 0.0574753
deltaT = 0.00141156
Time = 0.00260204
DILUPBiCG: Solving for Ux, Initial residual = 0.476498, Final residual = 0.0154958, No Iterations 3
DILUPBiCG: Solving for Uy, Initial residual = 0.544396, Final residual = 0.038276, No Iterations 2
DILUPBiCG: Solving for Uz, Initial residual = 0.72792, Final residual = 0.0189018, No Iterations 2
GAMG: Solving for p, Initial residual = 0.0426494, Final residual = 0.000233154, No Iterations 4
time step continuity errors : sum local = 2.41503e-06, global = -9.62014e-07, cumulative = 9.37232e-05
GAMG: Solving for p, Initial residual = 0.00865582, Final residual = 3.47567e-05, No Iterations 4
time step continuity errors : sum local = 3.52446e-07, global = 5.90545e-09, cumulative = 9.37291e-05
DILUPBiCG: Solving for epsilon, Initial residual = 0.260977, Final residual = 9.32683e-06, No Iterations 7
DILUPBiCG: Solving for k, Initial residual = 0.434994, Final residual = 7.99034e-06, No Iterations 10
DILUPBiCG: Solving for Ux, Initial residual = 0.103979, Final residual = 2.48923e-06, No Iterations 2
DILUPBiCG: Solving for Uy, Initial residual = 0.133591, Final residual = 1.85105e-06, No Iterations 2
DILUPBiCG: Solving for Uz, Initial residual = 0.889515, Final residual = 7.17669e-06, No Iterations 2
GAMG: Solving for p, Initial residual = 0.0686063, Final residual = 0.000531431, No Iterations 3
time step continuity errors : sum local = 1.44688e-05, global = -5.89197e-06, cumulative = 8.78372e-05
GAMG: Solving for p, Initial residual = 0.00661918, Final residual = 5.97428e-07, No Iterations 12
time step continuity errors : sum local = 1.57524e-08, global = 1.53929e-09, cumulative = 8.78387e-05
DILUPBiCG: Solving for epsilon, Initial residual = 0.398591, Final residual = 1.63817e-06, No Iterations 2
DILUPBiCG: Solving for k, Initial residual = 0.516357, Final residual = 5.80906e-06, No Iterations 2
ExecutionTime = 0.33 s ClockTime = 0 s

```

The *rhoPimpleDyMFoam* solver is run and the resulting max and mean Courant number is overly small, the maximum value should be typically less than 1. Courant number represents the fraction of the cell that the flow advances during a time step, by formula $Co = \frac{\Delta t * U_f}{\Delta x}$, where Δt is time step, U_f fluid velocity, and Δx is adjacent cells distance. Continuity error of the last loop stays small as shown above. Final residual is in the order of ten power to the minus seven, which approaches to zero. These are indications that the *rhoPimpleDyMFoam* solution converges successfully.

The Navier Stokes equation solved by the solver end up in the form of a matrix when the domain is discretised into cells and the equation is solved by integral calculation and then discretised for each cell. The resulting system of equations in a matrix form is solved by matrix inversion. OpenFOAM implements solvers to invert the matrix, these are: the Preconditioned BiConjugate Gradient(PBiCG), the algebraic multi-grid which is GAMG(Geometric-agglomerated Algebraic Multigrid) and the smooth solver for the residuals which is Diagonal-based Incomplete Lower Upper(DILU) smoother for asymmetric matrices, this simulation has asymmetric matrices therefore DILUPBiCG can be seen above(Greenshields, 2017).


```

1 /*-----* C++ *-----*/
2 |=====|
3 | \ \ \ \ / F i e l d | OpenFOAM: The open Source CFD Toolbox |
4 | \ \ \ \ / O p e r a t i o n | Version: 5 |
5 | \ \ \ \ / A n d | Web: www.OpenFOAM.org |
6 | \ \ \ \ / M a n i p u l a t i o n | |
7 /*-----*/
8 FoamFile
9 {
10     version      2.0;
11     format        ascii;
12     class         dictionary;
13     location      "constant";
14     object        thermophysicalProperties;
15 }
16 // ***** //
17
18 thermoType
19 {
20     type          hePsiThermo;
21     mixture       pureMixture;
22     transport     sutherland;
23     thermo        hConst;
24     equationOfState perfectGas;
25     specie        specie;
26     energy        sensibleEnthalpy;
27 }
28
29 mixture
30 {
31     Air
32     {
33         molweight  28.9;
34     }
35     thermodynamics
36     {
37         Cp         1007;
38         Hf         0;
39     }
40     transport
41     {
42         As         1.8e-05;
43         Ts         288.15;
44     }
45 }
46
47
48 // ***** //

```